



Technical Report 1999
January 2013

**Defining Munition Constituent (MC)
Source Terms in Aquatic Environments
on DoD Ranges (ER-1453)**

Final Report

P. F. Wang
R. D. George
W. J. Wild
SSC Pacific

Q. Liao
University of Wisconsin-Milwaukee

Approved for public release.

SSC Pacific
San Diego, CA 92152-5001

Technical Report 1999
January 2013

Defining Munition Constituent (MC) Source Terms in Aquatic Environments on DoD Ranges (ER-1453)

Final Report

P. F. Wang
R. D. George
W. J. Wild
SSC Pacific

Q. Liao
University of Wisconsin-Milwaukee

Approved for public release.



SSC Pacific
San Diego, CA 92152-5001

SSC Pacific
San Diego, California 92152-5001

J.J. Beel, CAPT, USN
Commanding Officer

C. A. Keeney
Executive Director

ADMINISTRATIVE INFORMATION

This report was prepared for the Strategic Environmental Research and Development Program (SERDP) by the Advanced Systems & Applied Sciences Division (Code 717), SPAWAR Systems Center Pacific, and the University of Wisconsin-Milwaukee.

Released by
Charles Katz, Head
Environmental Sciences
Branch

Under authority of
M. J. Machniak, Head
Advanced Systems &
Applied Sciences Division

This is a work of the United States Government and therefore is not copyrighted. This work may be copied and disseminated without restriction.

ACKNOWLEDGMENT

The authors would like to thank the Environmental Restoration Program Manager for the Strategic Environmental Research and Development Program (SERDP) for the support of this study. The SERDP project number is ER-1453.

EXECUTIVE SUMMARY

OBJECTIVE

The objectives of this study were to develop a basic understanding of the release rate and subsequent fate and transport of munition constituents (MCs) in water and in sediment. The ability to characterize, assess, and predict potential MC source loading and distribution has significant implications for Department of Defense (DoD) and Department of Navy (DoN) range sustainability initiatives. DoD will gain critical information for making scientifically defensible risk management decisions about underwater ordnance leave-in-place (LIP) mitigation and blow-in-place (BIP) vs. removal options. In addition to explosive blast (safety) considerations, future regulatory emphasis will likely require an assessment of potential underwater ordnance contamination and mitigation efforts that could include water and sediment quality issues.

TECHNICAL APPROACH

As a baseline scenario, this study directly addresses the amount of MC introduced into the environment from the case of a single breached munition. The information determined for MC release from a single breached shell was incorporated into the calibrated hydrodynamic/transport model to predict fate and transport of the MC and/or degradation products. To address the specific release function and its predictive ability, we conducted analytical, empirical, and numerical modeling studies of MC source release from breached shells under various hydrodynamic and shell integrity conditions. Release rates were developed and validated for a single breached shell in three nominal release scenarios: a shell on the surface of bottom sediment, a shell from a low-order detonation above the bottom in the water column, and a shell buried in sediment. The semi-analytical release rate function was validated by results from both the empirical study and the numerical modeling study, using the FLUENT model. The calibrated model, TRIM2D, and Environmental Protection Agency's (EPA) WASP7 model were both used for simulating fate and transport of trinitrotoluene explosive; 2-methyl-1,3,5-trinitrobenzene (TNT) released by design from a breach shell in San Diego Bay, California, and Elizabeth River, Virginia.

RESULTS

The release function developed semi-analytically assumes that the release through a breach in a munition casing can be determined by the following five key parameters: 1) the growth of the breach hole (as the radius of the hole, b); 2) the radius of the cavity formed due to loss of mass released from inside the shell, (R); 3) the dissolution rate (μ) from solid to aqueous phases of the MC inside the shell casing; 4) the outside ambient current (U) to which the casing hole is exposed; and 5) the hydrodynamic dispersion coefficient, (D). This function dictates the release rate be characteristically governed by two Reynolds Numbers: the current-based Reynolds Number (Ub/D), and the dissolution-based Reynolds Number ($\mu R/D$). Release rate is governed by current (U) and dissolution rate (μ) for the scenarios ($\mu R/D \gg Ub/D$) and ($\mu R/D \ll Ub/D$), respectively. Empirical studies were conducted for release scenarios both in the water column and in sediment. For a current-controlled scenario, release rates are proportional to the ambient current speed, and therefore, release rates in the water column are much greater than in sediment. However, total time for a complete MC release from a test shell ($L = 24''$, $r = 8''$, 8-kg MC weight) also depends on the breach hole size (e.g., crack area), and the dissolution rate, which can result in the total release time varying from a few days to several hundred years.

The fate and transport modeling study shows that predicted TNT concentrations are on the order of nanograms per liter (ng/L) in the vicinity of the release locations for a single test shell. This provides the basis for an order of magnitude estimate for worst-case scenarios. For example, to generate TNT concentrations to the micrograms per liter ($\mu\text{g/L}$) level in the water column, it would take one thousand shells of the same shell integrity to be co-located at a single site.

BENEFITS

A basic understanding of processes and governing factors for the release rate and fate/transport of MC in marine environment was developed. Predictive modeling capabilities were also developed for these processes, which will help DoD scientifically address the MC issues mentioned above. With the data developed from this study, DoD will be better equipped to make technically defensible managerial decisions for sites with underwater ordnance.

CONTENTS

EXECUTIVE SUMMARY	iii
SYMBOLS	xi
ACRONYMS	xiii
1. INTRODUCTION	1
2. BACKGROUND	5
2.1 SOURCE CHARACTERIZATION	5
2.1.1 Dissolution Rates and Solubility	6
2.1.2 Modeling Fate and Transport	7
2.2 MODELING FATE AND TRANSPORT OF TNT, RDX, AND HMX	7
2.3 MC RELEASE AND TRANSPORT BURIED IN SAND	9
2.3.1 Groundwater Seepage	10
2.3.2 Pore-water Advection Induced by Wave Effect	10
2.3.3 Wave Actions	11
2.3.4 MC Release from the Deep Sea Environment	12
3. MATERIALS AND METHODS	17
3.1 RELEASE FUNCTION OF MC FROM BREACHED SHELLS	17
3.2 DISPERSION OF MC FROM BREACHED SHELLS	17
3.2.1 Current-Controlled Release Function ($\mu R^2 \gg \alpha U b^2$)	19
3.2.2 Dissolution-Rate-Controlled Release Function ($\mu R^2 \ll \alpha U b^2$)	20
3.2.3 Low-Order Detonation Scenario Release	20
3.3 EMPIRICAL STUDY – UNBURIED SHELL	20
3.3.1 Experiment Test Platform	20
3.3.2 Measurement Techniques	22
3.3.3 Procedures	23
3.3.4 Estimation of the Mass Release Rate, F	26
3.3.5 Shear velocity u_*	28
3.3.6 Mass Release Velocity u_f vs. Shear Velocity u_*	29
3.3.7 Effect of Crack Hole Radius b on the Release Speed u_f	30
3.3.8 Effect of Cavity Radius R on the Release Speed u_f	31
3.3.9 Observed Universal Function for Mass Release Speed	31
3.4 EMPIRICAL STUDY – BURIED SHELL	31
3.4.1 Pore-water Flow Experiment	31
3.4.2 Dye Release Experiments	35
3.4.3 Mass Depletion Analyses	36
3.5 MODEL VALIDATION	37
3.5.1 Simulation Parameters	37

3.6 MODELING FATE AND TRANSPORT OF TNT, RDX, AND HMX	39
3.6.1 TRIM2D Model	39
3.6.2 TRIM2D Model Setup	41
3.6.3 WASP7 Model	41
3.6.4 WASP Model Setup	42
3.7 MODELING PORE-WATER ADVECTION IN SEDIMENT FLUME BOX	49
4. RESULTS AND DISCUSSION	55
4.1 MODEL VALIDATION	55
4.1.2 Validation Case I: Dependence on Current Speed, (U), and Radial Direction, (r)	55
4.1.3 Validation Case II: Dependence on Hole Size, (b)	57
4.2 EFFECTS OF SHELL THICKNESS	60
4.3 RELEASE TIME	60
4.4 MODELING FATE AND TRANSPORT OF TNT, RDX, AND HMX	67
4.4.1 TRIM2D Model Results	67
4.4.2 WASP7 Model Results	73
4.5 RESULTS OF TASKS 4.3.1A, 4.3.1B, 4.3.2, AND 4.3.6	76
4.5.1 Effect of Shapes of Opening	76
4.5.2 Effect of Orientation of Opening (rectangle of 4:1 aspect ratio)	78
4.5.3 Internal Circulation	81
4.5.4 Probabilistic Modeling	83
4.5.5 Monte Carlo Simulation Results	83
4.6 EMPIRICAL STUDY RESULTS – BURIED SHELL	85
4.6.1 Flux with Zero Seepage Velocity	92
4.7 MODELING STUDY RESULTS – BURIED SHELL	93
4.7.1 Transport of TNT in Sediment	94
4.7.2 Advection-Diffusivity Transport of MC in Sediment	95
5. CONCLUSIONS AND IMPLICATIONS FOR FUTURE RESEARCH/ IMPLEMENTATION	101
5.1 RELEASE RATE	101
5.2 MC TRANSPORT	102
5.3 SETTLING AND RESUSPENSION	103
5.4 SCALING AND INTERPRETATION	104
5.5 SIMULATING BREACHED SHELL SCENARIOS	105
5.6 FUTURE RESEARCH/IMPLEMENTATION	106
6. REFERENCES	107

Figures

1. Conceptual model for MC release from a breached shell with a hole.....	6
2. Simplified MC release rate conceptual model configuration	6
3. Study plan and tasks.....	9
4. Interactions between groundwater and surface ocean water	10
5. Schematic of pore-water flow field driven by oscillating flow interacting with a sediment ripple. Top and center show the pore-water flow field that would develop under steady unidirectional flow in opposing directions; the bottom drawing shows the averaged pore-water flow field under oscillating flow as induced by surface gravity waves (from Precht and Huettel, 2003).....	13
6. Global surface current system under average conditions for winter months in the Northern Hemisphere. Warm currents are shown as solid red arrows, and cold currents are shown as dashed blue arrows	11
7. Dissolution rates of TNT, RDX, and HMX from TNT, military formulations of Composition B, and Octol (Brannon et al., 2005).....	15
8. Dissolution rates for freshwater as a function of temperature (symbols with solid lines are empirical freshwater data from Lynch, Brannon, and Delfino (2002a). Dashed line represents best fits of the data for extrapolation to low temperature	16
9. Re-circulating flume tank and the conceptual release from the half dome	21
10. Test section of open channel flume at UWM hydraulic lab	21
11. Model flow platform and shell cavity	22
12. PIV measurement (with laser sheet).....	24
13. Measured internal flow circulation from the PIV images	25
14. Measured fluorescein concentration processes from the LIF images on a cross section downstream across the plume.....	26
15. Time series of measure mass release rate with small, median and large depletion time scale, t_D	27
16. Vertical profiles of the mean velocity and the Reynolds shear stress	29
17. The relation between mass release speed u_f , and shear velocity u	30
18. Normalized release speed vs. cavity radius based Reynolds number.....	32
19. (a) Schematic of the pore-water tank; (b) Drain holes on the sidewalls of the high-head and low-head reservoir.....	32
20. Dye tracing in the pore-water flow tank.....	33
21. Numerical model simulation result of the flow in the pore-water tank.....	34
22. Averaged head gradient function plot	34
23. Dye release and flux experiments.....	35
24. The container with a breach hole ($d_b = 0.56$ cm) used as an experimental breached munition surrogate	36
25. FLUENT model geometry and meshes generated by GAMIT	37
26. Contours of concentration on the central vertical plane and a cross-section. In this case, the breach hole is $b = 5$ mm in radius and the current speed is $U = 6$ cm/s.	38
27. Location (X) of MC release from a single breached shell, inner San Diego Bay and San Diego Naval Station, respectively (no loading scenario)	41
28. Model grid with eight boxes for WASP7 (box numbering starts from the inner bay and at the bay mouth)	43
29. Box model for Elizabeth River.....	46
30. Conceptual box model for fate and transport of TNT in Elizabeth River.....	47
31. Riverine freshwater inflows from five major river branches of the Elizabeth River watershed.....	48
32. Dispersion coefficients for Elizabeth River.....	49

33. 2-D model for pressure induced pore-water seepage flow in sand flume box.....	50
34. Interior, boundary, and corner nodes of the numerical mesh for solution of Eq. (36).....	51
35. Simulated pressure gradients over the three scenarios ($\Delta h = 1, 2,$ and 3 inches, for the top, middle, and bottom figures, respectively).....	52
36. Current-induced inner circulation in the casing. $b = 5$ mm and $U = 6$ cm/s.....	55
37. Distribution of uAr/Ub as a function of r for different current speed.....	56
38. Modeled relationship between the effective diffusivity D_A , and the current speed U	57
39. Variation of MC flux rate with respect to current speed.....	58
40. Radial distribution of concentration in the casing. Simulation results compared with analytical solution (Eq. (9)).....	59
41. Variation of MC flux rate F , as a function of hole radius b	59
42. Release rate vs. current speed for selected shell thickness, (h), and breach hole radii, (b).....	61
43. Effects of shell thickness on the normalized release rate.....	62
44. Measured dissolution rate constants for TNT, RDX, and HMX in freshwater and saline water (Brannon et al., 2005).....	63
45. Days to complete release of TNT inside the shell with dimension of $L = 24$ inches, $D = 8$ inches, and MC mass = 8 kg. Release time are plotted as functions of ambient velocity U , and hole radius (b).....	64
46. Release time for TNT, RDX, and HMX under the same conditions ($U = 15$ cm/s).....	64
47. Days for complete release (based on Eq. (10a)) for TNT, RDX, and HMX for a release case: $U = 10$ cm/s, $R = 10$ cm. The three up-pointing arrows represent the dissolution speeds for the three compounds.....	65
48. Release rates and current speeds over two tidal cycles (~24 hours) for TNT, RDX, and HMX ($b = 0.1$ cm, $R = 10$ cm).....	65
49. Release rates and current speeds over two tidal cycles (~24 hours) for TNT, RDX, and HMX ($b = 2.5$ cm, $R = 10$ cm).....	66
50. Current speed and estimated release rate at the inner San Diego Bay location.....	67
51. Simulated TNT concentration at the source location (inner San Diego Bay) and total TNT load during 1-year period.....	67
52. Steady-state TNT concentration during ebb tide (simulated release from inner San Diego Bay) (x-y coordinates are distances with I, J indices multiplied by 100 meters, the same convention hereafter).....	68
53. Steady-state TNT concentration during flooding tide (simulated release from inner San Diego Bay).....	69
54. Steady-state TNT concentrations with first-order mineralization during ebb tide (simulated release from inner San Diego Bay).....	69
55. Current speed and estimated release rate at Naval Station San Diego.....	70
56. Simulated TNT concentration at the source location (Naval Station San Diego) and total TNT load during 1-year period.....	71
57. Steady-state TNT concentrations during ebb tide (simulated release from Naval Station San Diego).....	71
58. Steady-state TNT concentrations during flooding tide (simulated release from Naval Station San Diego).....	72
59. Steady-state TNT concentrations with mineralization of TNT during flooding tide (simulated release from Naval Station San Diego).....	72
60. Wasp7-simulated TNT concentrations in water column for Cases 1a and 1b.....	73
61. WASP7-simulated TNT concentrations in sediment for Case 2a (water column transport and exchange with sediment) and 2b (with mineralization) for different partitioning coefficients for San Diego Bay.....	74

62. Simulated TNT concentrations in water column for Case 3a, with TNT release occurring in Box #2, #6, and #12, respectively	75
63. Simulated TNT concentrations in water column for Case 3b, with TNT release occurring in Box #2, #6, and #12, respectively	76
64. Simulated TNT concentrations in sediment for Case 4a (with partitioning coefficients without mineralization) and Case 4b (with mineralization), with TNT release occurring in Box #2	76
65. Simulated TNT concentrations in sediment for Case 4a (with partitioning coefficients and without mineralization) and Case 4b (with mineralization), with TNT release occurring in Box #6	77
66. Four different shapes of opening (above) and normalized mass release rates at different current speed (lower)	78
67. Normalized release rates vs. ambient current speed in the range of $0 < U < 0.15$ m/s (above), and the slopes for the four different shapes of openings	79
68. Normalized release rates vs. ambient current speed in the range of 0.15 m/s , U (above), and the slopes for the four different shapes of openings.....	80
69. Normalized release rates vs. ambient current speed for rectangle (4:1 aspect ratio) at different orientation angles.....	81
70. Model-simulated (above) and measured (below) internal circulation.....	82
71. Monte Carlo simulation for release rate and time for complete depletion of MC; b has a normal distribution	84
72. Monte Carlo simulations for release rate and time for complete depletion of MC: b has a log-normal distribution.....	84
73. Simulated release rate for a group of shells [a], prescribed probability distribution for shell number with a mean of 100 and standard deviation of 30 [b], and simulated total release rate [c], and probability of release time [d]	85
74. Fine sand, low seepage flow ($\Delta h = 1''$), crack hole diameter ($d_b = 0.21$ cm).....	86
75. Fine sand, medium seepage flow ($\Delta h = 2''$), crack hole diameter ($d_b = 0.21$ cm)	86
76. Fine sand, high seepage flow ($\Delta h = 3''$), crack hole diameter ($d_b = 0.21$ cm)	86
77. Fine sand, low seepage flow ($\Delta h = 1''$), crack hole diameter ($d_b = 0.40$ cm).....	87
78. Fine sand, medium seepage flow ($\Delta h = 2''$), crack hole diameter ($d_b = 0.40$ cm)	87
79. Fine sand, high seepage flow ($\Delta h = 3''$), crack hole diameter ($d_b = 0.40$ cm)	87
80. Fine sand, low seepage flow ($\Delta h = 1''$), crack hole diameter ($d_b = 0.56$ cm).....	88
81. Fine sand, medium seepage flow ($\Delta h = 2''$), crack hole diameter ($d_b = 0.56$ cm)	88
82. Fine sand, high seepage flow ($\Delta h = 3''$), crack hole diameter ($d_b = 0.56$ cm)	88
83. Coarse sand, low seepage flow ($\Delta h = 1''$), crack hole (diameter $d_b = 0.21$ cm).....	89
84. Coarse sand, medium seepage flow ($\Delta h = 2''$), crack hole diameter $d_b = 0.21$ cm	89
85. Coarse sand, high seepage flow ($\Delta h = 3''$), crack hole diameter $d_b = 0.21$ cm	89
86. Coarse sand, low seepage flow ($\Delta h = 1''$), crack hole diameter $d_b = 0.40$ cm	90
87. Coarse sand, medium seepage flow ($\Delta h = 2''$), crack hole diameter $d_b = 0.40$ cm	90
88. Coarse sand, high seepage flow ($\Delta h = 3''$), crack hole diameter $d_b = 0.40$ cm	90
89. Coarse sand, low seepage flow ($\Delta h = 1''$), crack hole diameter $d_b = 0.56$ cm	91
90. Coarse sand, medium seepage flow ($\Delta h = 2''$), crack hole diameter $d_b = 0.56$ cm	91
91. Coarse sand, high seepage flow ($\Delta h = 3''$), crack hole diameter $d_b = 0.56$ cm	91
92. Relationship between the estimated mass release velocity (u_r) and the seepage flow velocity (u_s).....	92
93. Change of concentration in water above the sand.....	93
94. Comparison of simulated and measured Darcy velocities at three head pressure differences for fine and coarse sands	93
95. Range of advection and diffusivity (e.g., molecular) in water and sediment (pore water).....	95

96. Dispersion of TNT in sediment by molecular diffusivity ($D_x = D_y = 1.18 \times 10^{-6} \text{ cm}^2/\text{sec}$, $D_z = 0.5 D_{x(y)}$) at time = 23 hours from initial condition (continuous source for $t > 0$, with concentration of 500 units at (0,0)).....	96
97. Dispersion of TNT in sediment by molecular diffusivity ($D_x = D_y = 1.18 \times 10^{-6} \text{ cm}^2/\text{sec}$, $D_z = 0.5 D_{x(y)}$) at time = 7th day from initial condition (continuous source for $t > 0$, with concentration of 500 units at (0,0)).....	97
98. Dispersion of TNT in sediment by molecular diffusivity ($D_x = D_y = 1.18 \times 10^{-6} \text{ cm}^2/\text{sec}$, $D_z = 0.5 D_{x(y)}$) at time = 30th day from initial condition (continuous source for $t > 0$, with concentration of 500 units at (0,0))	98
99. Transport of TNT in sediment by molecular diffusivity ($D = 1.18 \times 10^{-6} \text{ cm}^2/\text{s}$) and advection ($U = 0.001, 0.0001$ and 0.00001 cm/s , for top, middle, and bottom figures, respectively) from initial condition (continuous source for $t > 0$, with concentration of 100,000 units at (0,0)).....	99
100. A sketch of an energy balance model to scale the in-cavity circulation to external shear velocity	104

Tables

1. Characteristic depletion time (seconds) under the combination of cavity radius and hole radius under the median current condition.....	24
2. Shear velocities and ambient current speed (cm/s).....	29
3. Scaling between the mass release speed and the shear velocity, u_f/u	29
4. ANOVA results for u_f/u dependence on hole radius.....	30
5. ANOVA results for u_f/u dependence on cavity radius	31
6. Physical properties of sand in the dye release experiments.....	33
7. Pore-water flow conditions.....	35
8. Sizes and dimensions of the test breached shell.....	39
9. Model parameters for WASP7 (San Diego Bay and Elizabeth River).....	42
10. Grid sizes for the eight-box model grid for San Diego Bay	44
11. Simulation matrix for San Diego Bay using WASP7	44
12. Ranges and mean values of soil partitioning coefficients for TNT and RDX (Brannon and Pennington, 2002).....	45
13. Grid sizes for the 13-box model grid for Elizabeth River.....	47
14. Discharge data for Elizabeth River	48
15. Simulation matrix for Elizabeth River using WASP 7.....	49
16. Saturation concentrations (C_s), dissolution rates, and dissolution speed (μ) for TNT, RDX, and HMX in freshwater	62
17. Mineralization rates for TNT (data provided by Dr. Mike Montgomery, NRL).....	70
18. Comparison of TSS, settling velocity, and resuspension velocity for San Diego Bay and Elizabeth River.....	104

SYMBOLS

Symbol	Definition
α	Empirical coefficient
β	Empirical coefficient
ε	Porosity
μ	Dissolution rate
ρ	Water density
κ	Constant
ν	Kinematic viscosity
τ_b	Shear stress at the bottom
(u, v, w)	Velocity field
A	Constant
A_S	Area of interface between solid and aqueous phase of munition constituents
b	Breach Hole Size
B	Constant
C	Concentration
C_i	Initial dye concentration
C_o	Average concentration within the cavity
C_S	MC saturation concentration
D	Dispersion/diffusivity (hydrodynamic) coefficient
D_A	Diffusivity coefficient, circulation enhanced
D_M	Diffusivity coefficient, molecular
d_b	Breach hole diameter
F	Mass release rate
G	Gravitational constant
Δh	Head differential
H	Water depth
I	Indices for model grid in the x-direction (every 100 meters)
J	Indices for model grid in the y-direction (every 100 meters)
Q	Total discharge
r	Radial coordinate
R	Radius of cavity
Re_r	Cavity radius based Reynolds number
t_D	Time to depletion
U	Ambient current speed
u^*	Shear velocity
u_A	Averaged velocity field
Ub/D	Reynolds number
u_f	Mass release velocity
u_s	Seepage velocity
V	Current velocity
V	Volume of the container

ACRONYMS

1-D	One dimensional
2-D	Two dimensional
3-D	Three dimensional
ANOVA	Analysis of variance
atm	Atmosphere
BIP	Blow in place
CCD	Charge coupled device
CEC	Cation exchange capacity
CFD	Computational fluid dynamics
cm	centimeter
cm/sec	centimeter per second
DoD	Department of Defense
DPSS CW	Diode-pumped solid state continuous wave (laser)
EPA	Environmental Protection Agency
Eq	Equation
ERDC	Engineering Research and Development Center (US Army Corps of Engineers)
FLUENT	CFD software
HMX	High melting explosive; octagen; Octahydro-1,3,5,7-tetranitro-1,3,5,7-tetrazocine
hr	hour
Hz	Hertz (sec ⁻¹)
IEEE	Institute of Electrical and Electronics Engineers
kg	kilogram
km	kilometers
KOW	Octanol-water partition coefficient
L	liter
LIF	Laser induced fluorescence
LIP	Leave in place
m	meter
MC	Munitions constituent
µg	microgram
mJ	milliJoule
mm	millimeter
µm	micrometer
MODFLOW	modular 3D finite-difference ground-water flow model
mol	mole
mW	milliWatt
nm	nanometer
NOAA	National Oceanic and Atmospheric Administration
PC	Personal computer
PIV	Particle image velocimetry
PTU	Programable Timing Unit

RDX	Royal demolition explosive; Cyclotrimethylenetrinitramine; 1,3,5-Trinitroperhydro-1,3,5-triazine
Re	Reynolds number
Sc	Schmidt number
SSC Pacific	Space and Naval Warfare Systems Center Pacific
SUTRA	Saturated-unsaturated, variable-density ground-water flow with solute or energy transport model
TNT	Trinitrotoluene explosive; 2-methyl-1,3,5-trinitrobenzene
TOC	Total organic carbon
TOXI4	Model similar to WASP
TRIM2D	Depth-averaged tidal and residual circulation model software
TSS	Total suspended solids
USEPA	United States EPA
USGS	United States Geological Survey
UWM	University of Wisconsin at Milwaukee
WASP7	Water quality analysis simulation program

1. INTRODUCTION

This effort focused on providing the information necessary for assessing fate and transport processes associated with munition constituents (MCs) release from a single breached shell into a seawater environment. The objective is to provide a predictive modeling capability of MC fate and transport associated with an unexploded breached projectile. The results are being promulgated to assist Department of Defense (DoD) and regulatory agencies with a science-based predictive tool to estimate the amount of MC released to the environment from underwater munitions over time.

Our initial approach (Shell Model Phases I & II) focused on a non-empirical analytical and modeling scenario, wherein a single breached round is hypothetically introduced into the marine environment and subsequent MC release, fate, and transport are predicted. To understand the release behavior, we have developed a set of specific semi-analytical formulae that describe the release rate of munitions constituents under various conditions of shell integrity and hydrodynamic situations. Specifically, the MC release rate can be explicitly expressed as a function of the following five parameters: ambient current speed, hydrodynamic diffusivity coefficient, size of the breach hole, cavity volume inside the shell, and dissolution rate of MC from the solid to aqueous phase inside the shell. Predictions based on this semi-analytical release rate function have been partially verified by results from a generic fluid dynamic model, FLUENT. Generally, this release rate function is considered applicable for release of any type of chemical from breached shells, with breach openings ranging from tiny holes to fully exposed (low-order detonation), under various aquatic environments. However, to fully verify the semi-analytical solution, further modeling and empirical studies would help increase confidence in the underlying assumptions. Subsequent to model verification, a more complete model can be developed to include integration of empirical MC release rates, shell corrosion rates, and MC rates of decomposition. Use of these empirical process descriptors along with analytically/empirically verified release rate formulae will adequately describe and predict source release and fate and transport of MC from a breached shell in water and sediment environments, and can ultimately be used for evaluating risk to the environment in which the breached shell resides. Extrapolation to release by multiple shells is possible given additional information relating to the amount of MC associated with the number, type, and integrity of munitions in a prescribed area.

As an initial approach to coupling the release model described above to fate and transport, we have evaluated two additional fate and transport models, TRIM2D and WASP7. Details of the release rate formulae development, analysis and evaluation, and partial verification using FLUENT, empirical process descriptors, and preliminary fate and transport modeling results using TRIM2D and WASP7 are described. The WASP7 model simulates trinitrotoluene explosive. The 2-methyl-1,3,5-trinitrobenzene (TNT) concentrations in both water column and sediment with box-like resolution, whereas TRIM2D provides simulated TNT concentrations in water column at much finer resolutions. Both models provide meaningful complementary results that are mutually consistent, demonstrating their utility for developing an understanding of MC transport in aquatic environments.

Two estuarine scenarios are evaluated: San Diego Bay, California, and the Elizabeth River, Virginia. Due to unique characteristics of these two estuarine systems, the simulated transport and flushing patterns of TNT in these two Navy harbors exhibit significance differences. Generally, flushing in San Diego Bay is driven by tides, whereas flushing in Elizabeth River is driven by both tidal forcing and riverine flows. It was observed in the model that differences in TSS settling velocities and in the associated sediment bed is much more pronounced for Elizabeth River than for San Diego Bay, resulting in higher predicted TNT concentrations in the Elizabeth River sediments.

The Shell Model Phase III study focused on verification of the release rate function developed in the initial effort associated with MCs' release from a single breached shell into a shallow seawater environment. The objective was to provide a validated predictive modeling capability of MC release rate associated with a single unexploded breached projectile. Validated results are required to assist DoD and regulatory agencies with a science-based predictive tool that is technically defensible when using the models to estimate the amount of MC released to the environment from underwater munitions over time.

Phase III addressed the results of two primary tasks, the numerical modeling study and the corresponding empirical study and four subtasks. The general fluid dynamic model, FLUENT, was used to simulate the release rate of MC leached from a single breached shell under various hydrodynamic (*e.g.*, currents) and shell integrity (*e.g.*, sizes of breach hole and cavity) conditions. The simulated scenarios were designed and focused on the following four sub-tasks: 1) the effect of shapes of the opening, 2) effect of orientation of the crack opening, 3) internal circulation, and 4) probabilistic modeling. The first three scenarios were simulated for a single shell, and the last scenario addresses both a single shell and a group of shells associated with probabilistic functions for currents and hole sizes. Results from these studies are consistent with the analytical solutions previously developed in the Phase I Study.

The empirical study was conducted using the flume tank at the University of Wisconsin-Milwaukee. A surrogate dye in solution, used to mimic MC solution, with mixing in the cavity of a breached shell by the ambient currents, were measured by both PIV (Particle Imagery Velocimetry) and LIF (Laser Induced Fluorescence) instruments. From this empirical study, it was found, among other things, that release rate is governed by the Reynolds number (Ub/D), the release velocity (u_r), and the shear velocity (u_*). Generally, the release velocity can be correlated with the shear velocity. Correlation of the release velocity to the shell internal cavity size is stronger than that to the breach hole size, particularly for a large cavity. All of the empirical results compare well with the numerical modeling results, further verifying the release rate function.

For the initial three phases of study described generally above, we evaluated MC release from a breached shell sitting on the sediment bed, subject to hydrodynamic mixing and transport by ambient current. This resulted in the development and validation of the following MC release rate function, for which the derivation will be described later, incorporating five variables, breached hole size, internal cavity radius, ambient current, mixing coefficient, and dissolution rate:

$$F = \frac{2\pi DC_s}{\frac{2D}{\alpha Ub^2} + \frac{D}{\mu R^2} + \frac{1}{b} - \frac{1}{R}}$$

In Phase IV, we analyzed the order of magnitude of the pore-water advective transport and the relative magnitude between low pore-water advection and the diffusivity (mixing) coefficient. MC release for breached shells buried in sediment is dictated by the same release rate function, except that ambient current is replaced by pore-water flow, which generally is much slower than the current in the water column. The relative magnitude of these two quantities determines how the MC is released from a buried breached shell and how MC in the plume is transported in this situation.

The analysis of pore water and its effects on MC release and transport from breached shells buried in sediment was validated by both an empirical study and two modeling studies. The empirical study was conducted to measure release of dye (surrogate for MC) from a breached shell buried under the sediment in the "sediment flume box." Pore-water advection in sediment within the sediment flume

box was generated by maintaining a constant hydraulic head difference at the two ends of the box. Pore-water advection speed was measured and compared with a pore-water advection model based on Darcy's Law. The rate of dye release from the breached shell surrogate buried in sediment was recorded and then compared to the theoretical solution, which follows a first order decay rate. The pore-water model was further used to characterize the relative length scales of horizontal and vertical domains, within which pressure-induced pore-water advection occurs.

As demonstrated previously, the relative magnitude of pore-water advection versus mixing coefficient (or diffusion coefficient in sediment) can significantly influence MC release and transport behaviors in sediment. A model has been constructed to examine the effects of these two parameters on MC plume transport in sediment.

2. BACKGROUND

The ability to characterize, assess, and predict potential munition constituent (MC) source loading and distribution has significant implications for Department of Defense (DoD) and Department of Navy (DoN) range sustainability initiatives. DoD would gain critical information for making scientifically defensible risk management decisions about underwater ordnance leave-in-place (LIP) mitigation and blow-in-place (BIP) vs. removal options. The Navy and other DoD components have responsibility for human safety and environmental stewardship for inactive or active ranges that have been or are currently being utilized for military training/readiness and for ordnance left underwater as a result of historic military activities. In addition to explosive blast (safety) considerations, future regulatory emphasis may require an assessment of the ecological impact of MC on the marine environment. Such regulations would likely require an assessment of potential underwater ordnance contamination and mitigation efforts that could include water and sediment quality issues.

This effort directly addresses the amount of MC introduced into the environment from the case of a single breached round as a baseline scenario. This information can be then used to address the more complex issues implicit for a buried round, and also MC dispersed by a low-order detonation. Ultimately, the information determined for MC release from multiple breached shells can be further incorporated into appropriate models predicting fate and transport of the MC and/or MC degradation products. This study does not, however, address the density, quantity, or distribution of munitions at any particular site. Such data are critical to assessing overall risk and must be determined by other methods or technologies.

2.1 SOURCE CHARACTERIZATION

Source characterization is the term used to describe the type and amount of a contaminant introduced into the environment, generally as part of an exposure pathway that requires the assessment of risk to human health and/or the environment. Within the context of this proposal it is defined as the estimation of the mass of MC (TNT, royal demolition explosive; Cyclotrimethylene-trinitramine; 1,3,5-Trinitroperhydro-1,3,5-triazine (RDX), high melting explosive; octagen; octahydro-1,3,5,7-tetranitro-1,3,5,7-tetrazocine (HMX), and/or their breakdown products derived from their military compositions) in both quantity and form (chemical species) that are released from the breached shell into the water column and sediment.

To understand the release of MC from ordnance items, it is important to understand and quantify the fundamental processes that govern the release in the context of the three scenarios/conceptual models schematically shown in Figure 1 and Figure 2.

These fundamental processes are described by physical and chemical properties that ultimately define the total magnitude and rate of MC release into the surrounding environment for each of the scenarios of interest: 1) lying on top of the sediment, 2) entirely buried in sediment, or 3) as exposed solid energetic material released directly to the underwater environment, *e.g.*, in a low-order detonation. For scenarios 1 and 2, we assume that the release through a breach in a munition casing can be determined by the following five key parameters: 1) the start and growth of the breach or the hole (with a size of b , the radius of the hole); 2) the radius of the cavity formed due to loss of mass released from inside the shell, (R); 3) the chemical property (dissolution rate (μ) from solid to aqueous phases of the MC inside the shell casing); 4) the outside ambient current (U) to which the casing hole is exposed; and 5) mass of MC remaining inside (M_c). For scenario 3, low-order detonation contamination, only parameters μ (dissolution), U (ambient current), and M_c (mass remaining) need to be considered as an extreme case where a breach is infinite in size. It is the goal of this effort to define and quantify the MC release rate function, $F(b,R, \mu,U,M_c)$, as a function of the

five listed variables, which presumably govern the release rate of MC from the munition casing.

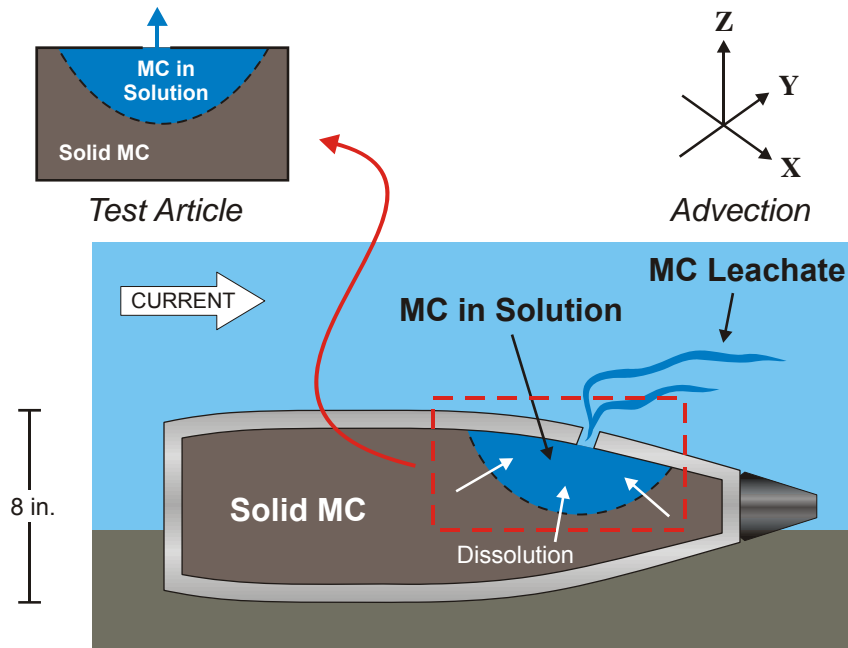


Figure 1. Conceptual model for MC release from a breached shell with a hole.

We have conducted both analytical and numerical modeling studies on MC release rates under various conditions. To validate these release rate results, an empirical study plan was developed as part of the follow-on (Phase II effort of this work). Results from previous studies on the chemical characteristics of MCs in marine water and sediment environments relevant to this study were evaluated and used for both the release rate solution and subsequent fate and transport modeling study. For example, results on chemical properties, such as solubility and dissolution kinetics for each of the munition constituents of interest, have been used to assist in defining the dependence of the MC release rate function (F) on the issues described in Sections 2.1.1 and 2.1.2..

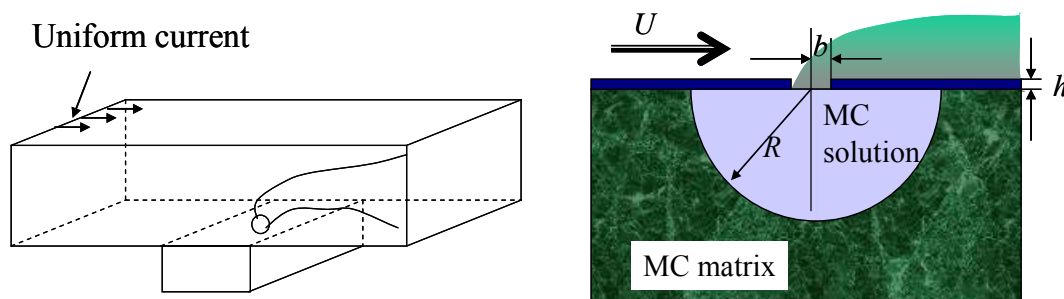


Figure 2. Simplified MC release rate conceptual model configuration.

2.1.1 Dissolution Rates and Solubility

Few measurements of aqueous dissolution of MC from military formulations have been conducted. The U.S. Army Corps of Engineers (ERDC-EL) has shown (Lynch, Myers, Brannon, and Delfino, 2001) that solubility and dissolution rates of TNT, RDX, and HMX in freshwater were not

significantly affected by pH over the range 4.2 to 6.2, but were significantly affected by temperature over the range of 3.1°C to 33.3°C. More recently, Lynch *et al.* (2001) and Lynch, Brannon, and Delfino (2002a; 2002b) conducted studies measuring dissolution rate with effects of surface area, mixing rate, and temperature correlated for the separate dissolution rates of TNT, RDX, HMX, and three military-grade compositions, including Octol (70/30% HMX/TNT), LX-14 (95.5/4.5% HMX/Estane), and Composition B (59.5/39.5/1% RDX/TNT/wax) (Lynch *et al.*, 2001; Lynch, Brannon, and Delfino, 2002a; 2002b; and Lynch, Brannon, Hatfield, and Delfino, 2003). In those studies, Lynch *et al.* (2002b) determined that dissolution of military compositions of explosive compositions occurs an order of magnitude slower than dissolution of the pure explosive compound. This is probably due to hindered diffusion and/or release of explosive compound from the binding matrix. Increased salinity has been reported to hinder crystalline TNT dissolution, while having little effect on crystalline RDX or HMX dissolution, or on dissolution from mixtures within a TNT, RDX, or HMX military composition (Brannon *et al.*, 2005). Environmental factors such as temperature and pH can affect solubility and, therefore, the chemical fate and toxicity (Huang *et al.*, 2000).

Both dissolution rates and solubilities of MCs in marine water are used in the release rate formulae (Brannon *et al.*, 2005). Solid phase MC dissolves into the aqueous phase at a rate (dissolution rate) that competes with the hydrodynamic diffusivity created by ambient current and the size of the breached hole, which act to disperse the MC solution out of the shell.

2.1.2 Modeling Fate and Transport

This study defines and quantifies the environmental process descriptors necessary to evaluate the fate and transport of dissolved MC in aquatic environments. When undissolved MCs (still contained within a shell) are introduced into the aquatic environment, there is no release until the shell is eventually breached by corrosion or other destructive processes. Compounds inside are then exposed to the ambient environment until totally depleted. Breach size (*i.e.*, shell casing hole size) is assumed to be a function of time in the case of corrosion. The results of a generalized/non-specific corrosion study initiated by Naval Facilities Engineering Service Center (Polly, 2012 [in prep.]) could be integrated into the release rate formulae, in which the hole size, b , will be a time-varying (growing) function determined from the corrosion study result. Total MC mass remaining inside the shell is another time-varying parameter that can be calculated by the difference between the initial mass and the total MC mass released from the shell from the beginning of the formation of the breached hole.

Once released into the environment, the MC sources undergo processes that govern fate, including degradation and partitioning, and transport processes, including diffusivity, advection, and exchanges between the water column and the sediment bed through partitioning, settling, and resuspension. Two existing numerical models, the general water quality model, WASP (EPA), and the fine-scaled fate and transport model, TRIM2D (U.S. Geological Survey and SSC Pacific), are used to simulate fate and transport from the MC source release from two different locations in San Diego Bay. These models have been rigorously scrutinized and their accuracies demonstrated by many users nationally and internationally for more than a decade. The results of these models should minimize uncertainties associated with model performance.

2.2 MODELING FATE AND TRANSPORT OF TNT, RDX, AND HMX

In Phase I, a conceptual model was first developed in which a shell with a circular breach hole rests on the bottom with ambient current flowing tangentially over the hole. Due to the hydrodynamic mixing through the breach hole, MC inside the shell is dissolved, an internal cavity is created in the solid MC matrix, and the MC solution is dispersed out of the shell through the hole and carried away by the ambient current. Based on this conceptual model, the release rate for a single breached shell in the marine environment was developed. Analytically, the release rate function can be

expressed explicitly with six dependent variables, which include the ambient current speed (U), breach hole size (b), hydrodynamic mixing coefficient (D), MC cavity radius inside the shell (R), the MC dissolution rate (μ), and the MC saturation concentration (D_s). Of these six variables, ambient current and breach hole size can be prescribed either from field data or estimated by a model. MC saturation concentration and dissolution rate, both as properties of the MC, can be obtained from literature values and/or laboratory data, such as that conducted at ERDC (Brannon *et al.*, 2005). The hydrodynamic mixing coefficient results from interactions of the ambient flow, the internal circulation, and the hole size and shape, and therefore, can be obtained by empirical data or by a numerical model. The semi-analytical release rate function was applied, under various hydrodynamic and shell integrity conditions, to three common MCs: TNT, RDX, and HMX. For these MCs, the time for complete depletion from a breached shell under various ambient current speeds was calculated to range from less than 1 year to over 1000 years, depending on the range of realistic values selected for the six variables.

In Phase II, the transport of MC release from breached shells was studied. Two fate and transport models, TRIM2D and WASP7, were evaluated and coupled with the MC release model described above. The WASP7 model simulates TNT concentrations in both the water column and sediment with box-like resolutions, whereas TRIM2D provides simulated TNT concentrations in the water column at much finer resolutions. Both of these models provide meaningful results that are mutually consistent and complementary, demonstrating their utility for developing an understanding of munitions constituent transport in the marine environment. Two estuarine scenarios were evaluated: San Diego Bay, California, and the Elizabeth River, Virginia. Due to the unique and distinctive characteristics of these two estuarine systems, the simulated transport and flushing patterns of TNT in these two Navy harbors exhibit significance differences. Generally, flushing in San Diego Bay is driven by tides, whereas flushing in Elizabeth River is driven primarily by the combined riverine flows and tidal forcing. It was observed in the model that differences in Total Suspended Solids (TSS) settling velocities and associated TNT between the water column and sediment bed is much more pronounced for the Elizabeth River than for San Diego Bay, resulting in higher predicted TNT concentrations in the Elizabeth River sediments. Details of the release rate formulae development, analysis and evaluation and partial verification using FLUENT, empirical process descriptors, and preliminary fate and transport modeling results using TRIM2D and WASP7 are in Section 4.2 and Section 5, respectively..

The Phase III effort conducted both a numerical modeling study and an empirical laboratory-based study to verify the semi-analytical release rate function. Results from both the numerical and empirical studies were compared with those from the semi-analytical release rate function. Specifically, the semi-analytical release rate function was compared and verified with results from the numerical computational fluid dynamics (CFD) model, FLUENT, and also from flume-tank experiments conducted at the University of Wisconsin-Milwaukee. This report documents study results for 1) effect of opening shapes, 2) internal circulation, 3) probabilistic modeling of the release rate, and 4) an empirical study for unburied shells (Figure 3).

Numerical simulations were conducted to 1) verify the release rate function, and 2) investigate the effect on the release rate from different shapes of the hole opening. Mass release rates were calculated for breach holes with different shapes, with the same opening areas, including a circle, a triangle, and two rectangles with aspect ratios of 4:1 and 10:1, respectively. The high aspect ratio rectangular shape was investigated for simulating cracks in a shell.

The variables for the mass release rate function can be treated in both a deterministic and probabilistic fashion. The probabilistic modeling has two components. The first addresses real-world scenarios and focuses on the variability associated with selected input parameters, and the second is

focused on (defined or undefined) uncertainties associated with those input parameters. For the first scenario, ambient current amplitudes and hole sizes were assigned probabilistic distribution functions, then Monte-Carlo simulations were conducted. Predicted mass release rates for these scenarios were associated with probabilistic distributions. Subsequently, the Monte-Carlo-based probabilistic model allowed for uncertainty and sensitivity analyses of the predicted mass release rates.

The empirical study was conducted at the flume tank of the University of Wisconsin-Milwaukee. The tank was designed to run flows with a current speed range of ~ 7 to 45 cm/s. Semi-circular hollow domes (purchased) with different radii were sequentially glued to an acrylic sheet. Holes of different radii were drilled at the center of an acrylic sheet forming the impermeable closure to the top of the half dome. Fluorescein was used as the surrogate dye for MC and was placed inside the half dome, which was placed under the acrylic sheet over which tank water flowed at the designed speed. Particle image velocimetry (PIV) was used to measure flow speed inside and outside the half dome. Released dye from the hole was measured ~20 cm downstream by the laser-induced fluorometry (LIF) device. Both data were measured as images, and image processing algorithm software was used to calculate flow speed from PIV data and dye concentrations from the LIF data.

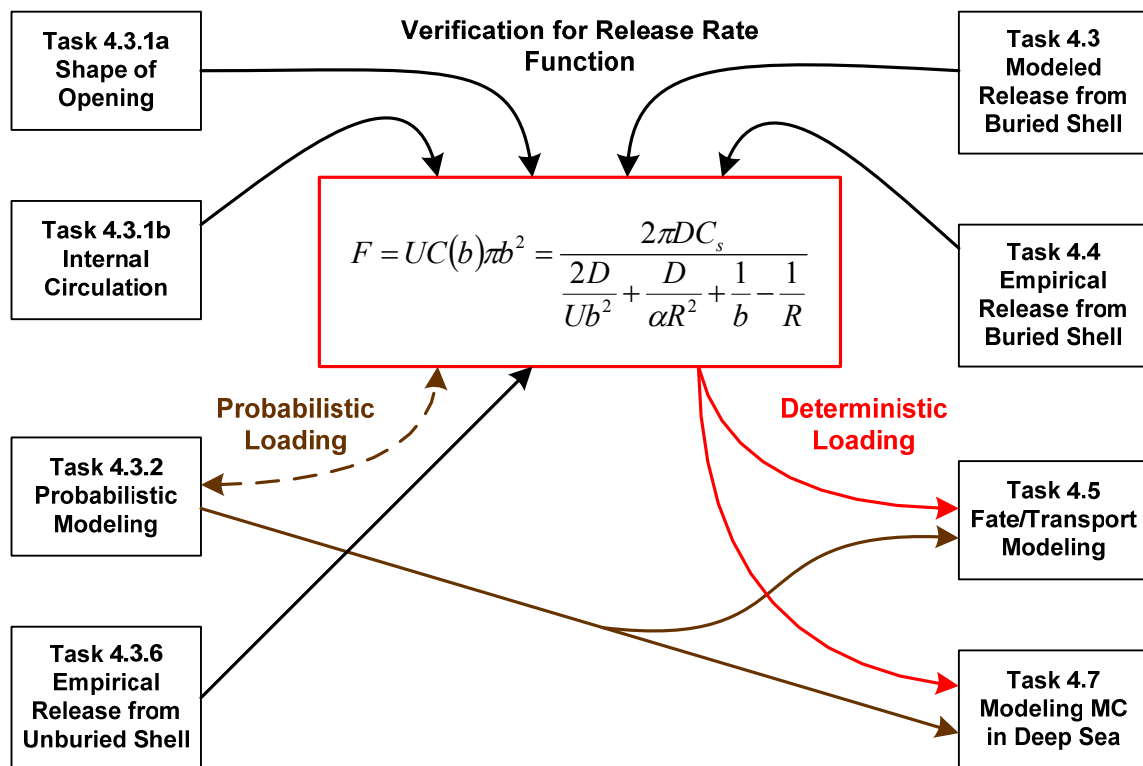


Figure 3. Study plan and tasks.

2.3 MC RELEASE AND TRANSPORT BURIED IN SAND

Pore water flows in coastal water are affected by multiple factors, including advection induced by surface waves, ground water seepage, and mixing by both flow-induced mixing and molecular diffusivity. In near-shore, coastal regions, surface waves exert pressure on the sediment bed, and hence, pore water in the sediment bed is subject to wave actions. Such actions and their impacts on

pore-water advection, although minute, are continuous, and thus the accumulated effects on the release rate are likely not negligible.

Similar to wave actions, groundwater flows in coastal and near-shore regions have effects on the advection and mixing of MC release. Groundwater seepage in these regions results from multiple sources. For all of these forcing functions, the seepage flows follow Darcy's law, which correlates flow with pressure (hydraulic head) gradients.

2.3.1 Groundwater Seepage

Groundwater in coastal region sediments originates from the interactions of ocean water and inland surface waters (rivers, streams, lakes) and groundwater. Generally, ocean water and inland water meet and interact near the shoreline and beach areas. These interfaces are composed of porous media through which interactions and exchanges of inland freshwater with the saline ocean water take place. For a cross-section view cutting across the shoreline (Figure 4), the direction of pore-water flow is seaward under low tide and high river flow or high water table conditions. Conversely, pore-water flow is landward under high tide, low river flow, or low water table conditions. Pore-water advection in these coastal and shoreline regions has been studied extensively in both field efforts and modeling studies. In general, a groundwater model, such as MODFLOW or SUTRA, can be applied to quantify and predict dynamics of groundwater and pore-water flows. Based on the fundamental underlying principles of these models, a simple two-dimensional (2-D) model has been developed for predicting the pore-water advection in the sediment flume laboratory study.

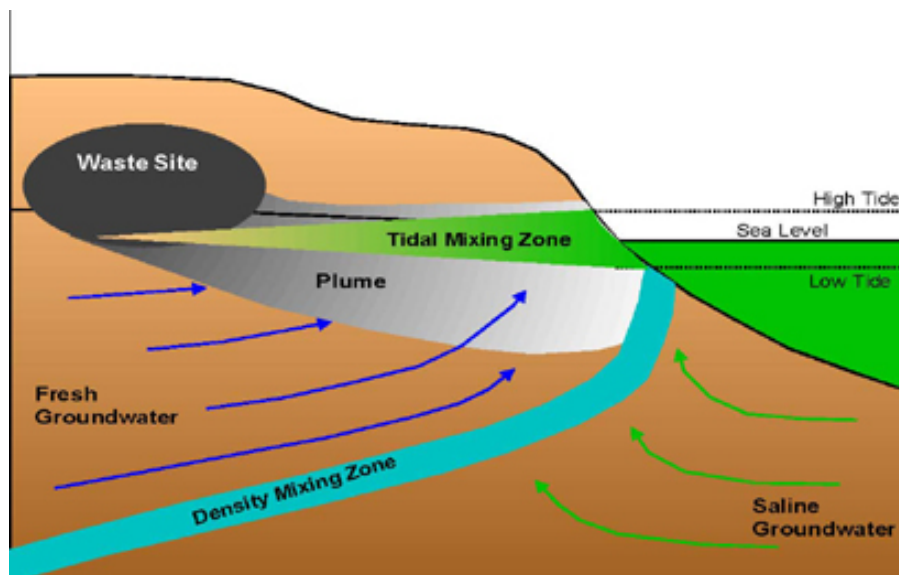


Figure 4. Interactions between groundwater and surface ocean water.

2.3.2 Pore-water Advection Induced by Wave Effect

Pore-water velocities associated with current-induced pressure gradients (Figure 5) are typically in the range of several centimeters (0.1 to 9.2 cm) per hour (Huettel and Gust, 1992; Huettel, Forster, Kloser, and Fossing, 1996). Advective pore-water flow in the natural environment has also been reported. Tracing of dye plumes injected into the sand at shallow, rippled Mediterranean sites revealed the presence of pore-water advection in the presence of wave-induced oscillating bottom flow (Precht and Huettel, 2004). In Mid-Atlantic Bight sediments that were exposed to combined tidal and wave-driven currents, the presence of fast vertical pore-water transport became apparent from the short time it took iodide, released above the sediment surface, to arrive at the tip of a

voltammetric sensor 20 mm below the sediment surface (Reimers *et al.*, 2004). Even relatively slow advective pore-water circulation at velocities of a few centimeters per hour resulted in intense interfacial exchange of solutes. In flume experiments with stained pore waters, Huettel and Gust (1992) observed interfacial pore-water exchange in the presence of small mounds (height ≤ 25 mm) and quantified the rates in terms of dye release to the overlying water.

In a low-pressure, bottom-sea mound (sand ripple, as per Figure 5), pore water was transported upwards from > 100 mm sediment depth and released at the sediment surface. Near the mounds, dye release exceeded diffusion by three orders of magnitude. Based on these measurements, Huettel and Gust (1992) estimated that advection induced by mounds at natural densities in the North Sea intertidal would affect the entire surface area and result in a fold increase of fluxes when compared to diffusion. Using a similar experimental approach, other researchers (Precht and Huettel, 2003) quantified solute exchange across rippled beds in a wave tank under oscillating currents and found release rates that were 50 times greater than diffusive exchange.

2.3.3 Wave Actions

Coastal waves impose pressure on the sediment bed in coastal shallow regions. Due to their dispersive nature, ocean waves propagate at various speeds according to their wavelengths and frequencies. When waves propagate from deep ocean water toward the shallow coastal water, they gradually impose increasing pressure onto the sediment bed. As these waves are restricted by the shallow near-shore regions, the wave heights grow and eventually break in the surf zone, which further impose impacts to the bottom sediments. These wave-induced impacts on sediment and pore water are briefly discussed here.

Generally, ocean waves can be approximated by the sum of multiple trains of single linear waves, each of which has an amplitude expressed as

$$\eta(x,t) = H \sin(kx - \omega t), \quad (1)$$

where H is a constant representing the maximum amplitude of the wave train. The wave number, $k = 2\pi/\lambda$, and the frequency, ω , are related by the dispersion equation:

$$\begin{aligned} \omega^2 &= gk \tanh(kh) \\ &= gk \text{ for deep water; } h/\lambda > 1/4 \\ &= gk^2 h \text{ for shallow water; } h/\lambda < 1/11, \end{aligned} \quad (2)$$

where g is the gravity constant (9.8 m/s^2), λ is the wave length, h is the local depth, and tanh is the hyperbolic tangent function,

The speed of the traveling wave (traveling velocity) can be expressed as the ratio of the wavelength over the period:

$$\begin{aligned}
C &= \frac{\lambda}{T} \\
&= \frac{\omega}{k} \\
&= \frac{g}{\omega} \text{ for deep water} \\
&= \sqrt{gh} \text{ for shallow water,}
\end{aligned} \tag{3}$$

where T is the wave period (in seconds).

As can be shown in Eqs. (2) and (3), deep-water waves are dispersive long waves, with low frequencies traveling faster than short waves with high frequencies. Note that in the equations both deep- and shallow-water waves are defined by the parameter, kh , which is a ratio of water depth versus wave length. Therefore, a wave with the same wavelength is defined as a shallow water or deep water wave according to the parameter, kh . In addition, for a group of waves originated offshore, long waves travel faster and reach the surf zone first. As these long deep-water waves travel to the shallower regions, they gradually become shallow-water waves, with traveling velocity restricted by the local depth, again as shown in Eq. (3).

Pressure exerted by a wave train to the bottom sediment can be expressed as

$$p(x,t) = \frac{\rho g H}{2 \cosh(kh)} \sin 2\pi \left(\frac{x}{\lambda} - \frac{t}{T} \right). \tag{4}$$

The pressure exerted by the wave train on the bottom propagates along the x-direction and is oscillatory in time. Pressure, and its gradient exerted by the wave at the sediment water interface, also decays exponentially with depth. Therefore, surface waves lose their effects rapidly as water depth increases. Eq. (4) provides the boundary condition that generates pore-water flows, which is also oscillatory. In reality, advection in pore water, resulting from the pressure differences of the waves, dissipates fast inside the sediment bed, because ocean waves are random with multiple wave directions, which counteract wave actions from multiple directions and wave components.

2.3.4 MC Release from the Deep Sea Environment

As discussed above, groundwater seepage and wave actions can produce pore-water advection in shallow, coastal regions, where the interactions of fresh surface water and saline ocean water take place and surface wave actions can reach the bottom. These effects are reduced significantly (exponentially) in deep-sea environments. However, MC release rate is affected by deep-sea currents, which are affected by global circulation, and altered dissolution rate due to low water temperature.

In addition to very low water temperature, the deep sea is also characterized by high dissolved oxygen, darkness with no sunlight, and currents with variable magnitudes. All of these features have potential impacts on the release rates of MC in deep-ocean regions. To study MC release from breached shells in deep-sea environment, the semi-analytical release function developed and validated in this study is further analyzed by evaluating the relative magnitudes for three of the five governing variables, including 1) ambient current (U), 2) hydrodynamic mixing coefficient (D), and 3) dissolution rate constant (μ). The other two variables, hole size and internal cavity volume, would have no significant differences between deep and shallow seawater scenarios.

Deep-Sea Currents

Deep-sea currents are primarily driven by four major forcing components, including energy from the sun, the rotation of the earth, the shape of land masses, and shape of the ocean floor. Solar energy is more intense at the equator than at the poles, causing the air and water near the equator to be hotter than at higher latitudes. The heated warm water near the equator moves the water along the density gradient northward (Figure 6). For example, the Gulf Stream is driven by the warm water from the equator traveling north along the east coast of America (Gaskell, 1973). As the current travels further north, one section moves south down the west coast of Africa, before completing a full circle to return to the Gulf of Mexico. The second, often referred to as the North Atlantic Drift, moves further north up the west coast of Ireland and Scandinavia and cools at high altitudes and then sinks as a deep-water cold current back along the east coast of America. Due to the rotation of the earth, the Coriolis Effect and trade winds force the currents to flow in a clockwise direction (Gross, 1982). In addition to the above, land masses and their distributions also dictate the currents and circulations in waters bounded by the land.

Magnitudes of deep-sea currents have been reported to vary with geographical location, ranging from 2 to 10 cm/sec on the low end (Adams, 1999a and 1999b), to 4 to 14 cm/sec (Gross, 1990), and to the high end of ~150 cm/sec (Coble, Murray, and Rice, 1987), within the Gulf Stream. These current speed ranges are equivalent to those for tidal currents in estuaries, coastal regions, and harbors for which the MC release study was designed. Therefore, impacts to the MC release rates from deep-sea currents depend, to a great extent, on the magnitude of the currents, in a pattern similar to those in the shallow estuaries, harbors, and coastal regions.

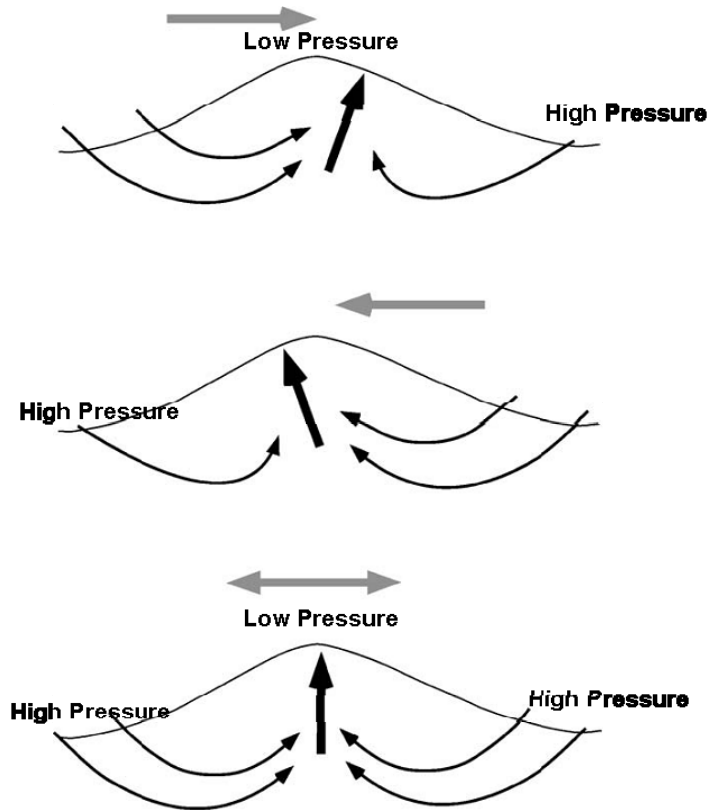


Figure 5. Schematic of pore-water flow field driven by oscillating flow interacting with a sediment ripple. Top and center show the pore-water flow field that would develop under steady unidirectional flow in opposing directions; the bottom drawing shows the averaged pore-water flow field under oscillating flow as induced by surface gravity waves (from Precht and Huettel, 2003).

Hydrodynamic Mixing

Hydrodynamic mixing also plays a role in mixing and exchanging solute with ambient water through the hole. It is also demonstrated that the hydrodynamic mixing is strongly correlated with the magnitude of the ambient current and size of the internal cavity, and to a lesser degree, with the breach hole size. Since the internal cavity size and its growth are directly related to the overall release rate, *i.e.*, the reduction in munition fill through MC dissolution and release, the internal cavity factor can be neglected since it is a result of the overall release rate. In the deep sea, wave effects and groundwater are negligible, which leaves deep-sea current as the single factor that determines the hydrodynamic mixing parameter, which follows the release rates validated in this study.

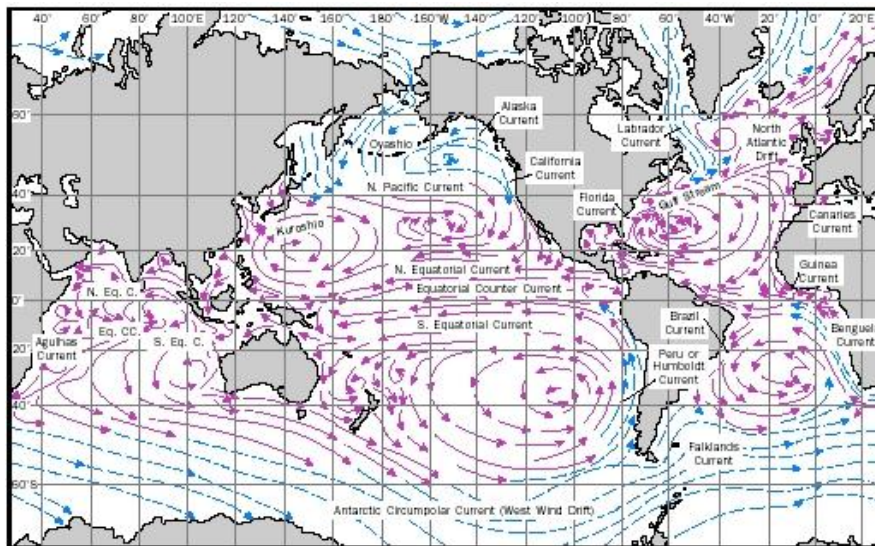


Figure 6. Global surface current system under average conditions for winter months in the Northern Hemisphere. Warm currents are shown as solid red arrows, and cold currents as dashed blue arrows.

Hydrodynamic Mixing

Hydrodynamic mixing also plays a role in mixing and exchanging solute with ambient water through the hole. It is also demonstrated that the hydrodynamic mixing is strongly correlated with the magnitude of the ambient current and size of the internal cavity, and to a lesser degree, with the breach hole size. Since the internal cavity size and its growth are directly related to the overall release rate, *i.e.*, the reduction in munition fill through MC dissolution and release, the internal cavity factor can be neglected since it is a result of the overall release rate. In the deep sea, wave effects and groundwater are negligible, which leaves deep-sea current as the single factor that determines the hydrodynamic mixing parameter, which follows the release rates validated in this study.

Dissolution Rate Constants (μ)

Dissolution rate constants are temperature dependent, which may be most influenced by the low water temperatures found in deep-sea environments. Before we investigate the temperature effect on the release rates, temperature in the deep-sea environment is briefly discussed.

Temperature of ocean water is influenced by multiple factors, including heat from the sun, salinity, and water mass transport (circulation and the mixing). Much of the ocean water (over 90%) is found below the thermocline, which is located 50 to 100 m in the deep ocean. Temperature should have an effect on the dissolution rate, which is a parameter of the release rate function. Dissolution rate constants for TNT, RDX, and HMX in freshwater have been published for freshwater (Lynch,

Brannon, and Delfino, 2002a) and for seawater (Brannon, et al., 2005). Dissolution rates for the three munition constituents, including TNT, HMX, and RDX, do not vary by much when compared to freshwater and seawater (Figure 7, Brannon, et al., 2005) The rate constants for freshwater (Lynch, Brannon, and Delfino, 2002a) were measured at three different temperatures, 10°C, 20°C and 30°C, respectively. Generally, temperatures for typical coastal surface water are within these ranges and measured rate constants can be directly used for these regions. However, in the deep ocean, temperature can drop rapidly below the thermocline to the range of 0 to 4°C. Dissolution rate constants measured for the normal shallow water temperatures, namely 10°C, 20°C, and 30°C, can be linearly extrapolated for low temperature conditions.

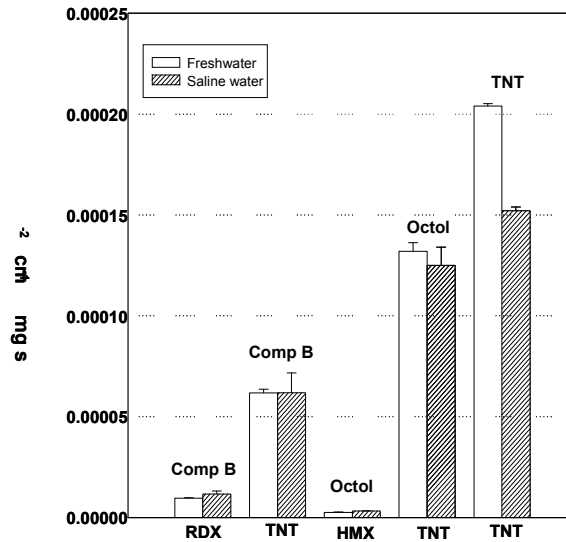


Figure 7. Dissolution rates of TNT, RDX, and HMX from TNT, military formulations of Composition B, and Octol (Brannon et al., 2005).

Figure 8 shows the dissolution rates of TNT, RDX, and HMX, extrapolated for 4°C water from those measured by Lynch, Brannon, and Delfino (2002a). Compared to the 20°C coastal surface water, the dissolution rates are reduced by a factor of 2.7 for TNT, a factor of 10 for RDX, and a factor of 7 for HMX. The temperature effect is much greater than the salinity effect. This is significant because the rate constants directly govern the dissolution rate in a linear fashion and the reduced dissolution in a cold, deep-water environment dictates that it should take a longer time for MC depletion from breached shells in these environments.

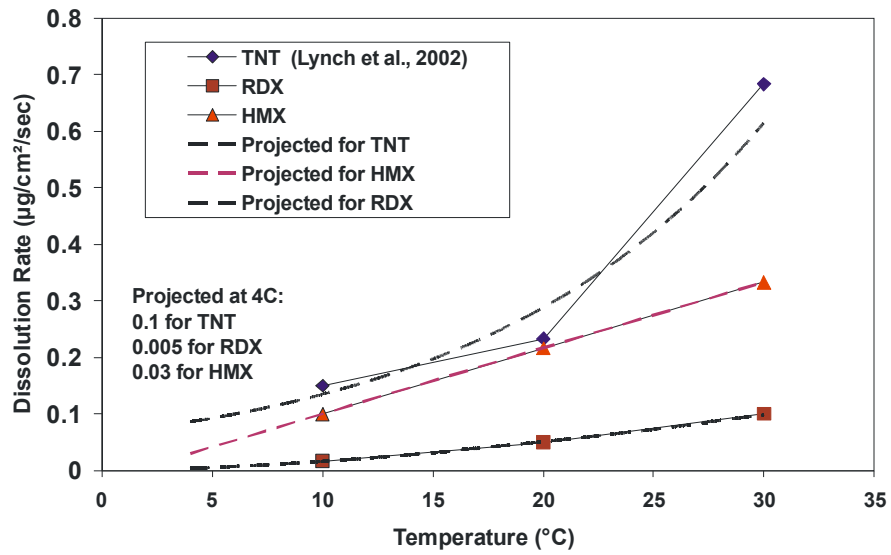


Figure 8. Dissolution rates for freshwater as a function of temperature (symbols with solid lines are empirical freshwater data from Lynch, Brannon, and Delfino (2002a). Dashed line represents best fits of the data for extrapolation to low temperature.

3. MATERIALS AND METHODS

3.1 RELEASE FUNCTION OF MC FROM BREACHED SHELLS

The approach to estimate the release rate of unexploded munition constituents (MCs) from breached shells into estuarine and coastal waters has included the development of an analytical release function and partial verification using a numerical model, FLUENT. The analytical release function is derived with the assumption that MC is released through the breached hole and exposed to ambient hydrodynamic conditions. Specifically, the MC release through a breach in a munition casing is determined by the following five key parameters: 1) the start and growth of the breach or the hole in the shell casing (with a size of b , the radius of the hole), 2) the radius of the cavity formed due to loss of mass released from inside the shell (R), 3) the chemical property (dissolution rate (μ) from solid to aqueous phases of the MC inside the shell casing), 4) the ambient current (U) to which the casing hole is exposed, and 5) mass of MC remaining inside (M_c). This effort's goal is to define and quantify the release function, $F(b, R, \mu, U, M_c)$, as a function of the five variables, which presumably govern the release rate of MC from the munition casing

This analytical release function was validated by the numerical model, FLUENT, which is a commercial computational fluid dynamic (CFD) software program. The munition source is considered a passive scalar concentration governed by a fluid transport equation, which is solved concurrently with flow equations. The MC release rate is calculated from simulation results. The dependency of the release rate on the breach size, ambient current, and shell thickness were examined with FLUENT modeling. Based on simulation results, this analytical equation for the release rate is proposed, which can be easily implemented as a source term into any fate and transport model.

3.2 DISPERSION OF MC FROM BREACHED SHELLS

In the MC release problem, it is assumed that MC is released from the shells through a breach or hole in the shell casing, which is exposed to ambient currents. The size of the hole is assumed to be small compared to the overall size of most shells, with curvatures that are small enough not to affect the ambient currents at the outer surface of the shell as in the conceptual model (Figure 1). Under these assumptions, the MC release process can be approximated by a flat plate as in the simplified conceptual model, Figure 2, in which MC is released from a hole on the plate over which ambient current flows.

It is assumed that most of the total release occurs during a stage when a relatively large cavity (compared to the breach hole or crack) has formed due to dissolving of the MC matrix. Thus, the overall release rate is governed by the advection and diffusion of MC concentration within the inner cavity, which is in turn determined by the dissolution of MC at the solid-solution interface and the exchange flow at the breach (boundary conditions). The driving force for MC leaching from the inner cavity is the hydrodynamic diffusion caused by ambient current inside the cavity, which generates inner circulation. We also assume that the local shear stress near the breach hole largely determines the inner circulation of the MC solution, *e.g.*, different external flow conditions with similar near-breach/hole hydrodynamic conditions result in a similar inner circulation pattern, resulting in approximately the same mass depletion rate.

Based on the above assumptions, the MC flux can be examined with a simplified conceptual model consisting of a uniform ambient fluid flowing over a flat plate that represents the surface of a shell as in Figure 1 and Figure 2. The shell breach is modeled as a circular hole with radius b . Water flows over the hole with speed U . The typical flow inside the cavity is characterized with three-dimensional (3-D) structures. However, we assume a cavity with a spherical shape with radius R , *i.e.*, diffusion/mixing process (by molecular diffusion and flow-induced stirring) is considered homogeneous. The

3-D diffusion/mixing problem inside the casing is thus simplified to a one-dimensional (1-D) process. The controlling equation can be written as

$$\frac{\partial C}{\partial t} = D \frac{1}{r^2} \frac{\partial}{\partial r} \left(r^2 \frac{\partial C}{\partial r} \right), \quad (5)$$

where C is concentration as a function of radial direction, r , and time, D , is a dispersion/diffusivity coefficient, which may include the combined effects of molecular diffusion, D_M , and circulation induced mixing, D_A , (*i.e.*, $D = D_M + D_A$), where D_M is known as a physical property of seawater and MC and D_A is an hydrodynamic function induced by ambient current speed, U , which will be obtained empirically from the results of the numerical model, FLUENT.

At an equilibrium state, the general solution to Eq. (5) is

$$C(r) = B - \frac{A}{r}, \quad (6)$$

where r is hole radius, and A and B are constants.

The boundary condition at the solid-liquid interface is prescribed as

$$-D \frac{dC}{dr} = \mu(C_s - C) \quad @r = R, \quad (7)$$

where μ is the dissolution speed [cm/s], which is obtained by dividing the dissolution rate [mg/cm²/s] over the saturation concentration C_s (solubility), [mg/L]. This boundary condition reflects the fact that flux by diffusion at the solid/liquid interface is in equilibrium with the dissolution process.

At the breach hole, the flux of C caused by mean current is considered to be linearly proportional to U , the local C and the 2-D area of the hole, *i.e.*, MC flux is prescribed as $\alpha UC\pi b^2$, which is in equilibrium with diffusive flux from just inside the hole. The coefficient α (approximately equal to 1) is a model parameter that is a function of the local geometry of the breach hole/crack and the thickness of the shell. Thus, we can write the boundary condition at the breach hole as

$$2\pi b^2 D \frac{dC}{dr} = \alpha UC\pi b^2 \quad @r = b$$

or

$$\frac{dC}{dr} = \frac{\alpha U}{2D} C \quad @r = b.$$

Substituting boundary conditions, Eqs. (7) and (8), into the general solution, Eq. (6), we have obtained the following concentration field inside the cavity:

$$C(r) = \frac{C_s}{\frac{2D}{\alpha U b^2} + \frac{D}{\mu R^2} + \frac{1}{b} - \frac{1}{R}} \left(\frac{2D}{\alpha U b^2} + \frac{1}{b} - \frac{1}{r} \right). \quad (9)$$

The MC release rate can be obtained, by definition, as follows:

$$F = \alpha UC(b)\pi b^2 = \frac{2\pi DC_s}{\frac{2D}{\alpha Ub^2} + \frac{D}{\mu R^2} + \frac{1}{b} - \frac{1}{R}}. \quad (10a)$$

F is the release rate function, which, as depicted in Eq. (10a), is a closed-form solution with the five variables, including hydrodynamic diffusivity coefficient (D), current (U), hole size (b), cavity radius (R) and dissolution speed of MC from solid to aqueous phase (μ). The model parameter α is defined as a geometry factor (Eq. (8)).

Eq. (10a) can also be expressed in a non-dimensional form as follows:

$$\begin{aligned} \bar{F} &= \frac{F}{\pi b^2 UC_s} \\ &= \frac{\frac{2D}{Ub}}{\frac{2}{\alpha} \left(\frac{D}{Ub} \right) + \frac{b}{R} \left(\frac{D}{\mu R} \right) + 1 - \frac{b}{R}}. \\ &\sim \frac{\kappa}{\frac{2}{\alpha} \left(\frac{D}{Ub} \right) + \frac{b}{R} \left(\frac{D}{\mu R} \right) + 1 - \frac{b}{R}}. \end{aligned} \quad (10b)$$

The denominator of Eq (10b) includes three non-dimensional parameters, including the current-based Reynolds Number (Ub/D); the model parameter α and the number 2, which are both constants; the dissolution-based Reynolds Number ($\mu R/D$); and the hole-to-cavity size ratio (b/R). The hydrodynamic properties, D and U, can be described by field data or a numerical fluid dynamic model. The coefficient κ in the numerator can be obtained empirically either by laboratory experiment or from the FLUENT model. In our numerical modeling experiments using FLUENT, to be discussed later, the value of κ is between 0.015 and 0.035, and $\kappa = 0.023$ if shell thickness is neglected.

Generally, the breached hole is much smaller than the cavity during scenarios where mass flux is most significant. As a result, the $1/R$ term in the denominator of Eq. (10a) can be neglected, which will help to highlight the behavior of the release rate function for the two extreme conditions described in Sections 3.2.1 and 3.2.2.

3.2.1 Current-Controlled Release Function ($\mu R^2 \gg \alpha Ub^2$)

When the dissolution speed (μ) is much larger than the ambient current (U) or the cavity (R) is much larger than the hole (b), MC solutions inside the cavity are near saturation and the release rate of MC is controlled by the ambient current speed U and the hole size. The release rate function can be simplified explicitly as

$$F = \frac{2\pi DC_s}{\frac{2D}{\alpha Ub^2} + \frac{1}{b}}. \quad (11)$$

The MC release rate increases with ambient current speed, the area of the hole, and the saturation concentration of the MC.

3.2.2 Dissolution-Rate-Controlled Release Function ($\mu R^2 \ll \alpha U b^2$)

For this case, release of MC is controlled by the dissolution speed (rate), since ambient current and/or the hole is so large that MC solution dissolved from the solid phase is dispersed out of the breached shell immediately:

$$F = \frac{2\pi D C_s}{\frac{D}{\mu R^2} + \frac{1}{b}} \quad (12)$$

$$\approx 2\pi R^2 \mu C_s ; \quad \text{if } \frac{\mu R}{D} \ll \frac{b}{R}$$

When the hole size is relatively small (compared to the parameter, $\mu R^2/D$), the hole has a damping effect, restricting the release rate of MC out of the shell. When the hole size becomes relatively large (compared to $\mu R^2/D$), the damping effect of the hole diminishes and the release of MC is directly proportional to the surface area of the cavity ($2\pi R^2$) and the mass dissolution rate (μC_s), as indicated in Eq. (12).

3.2.3 Low-Order Detonation Scenario Release

In the case where shells are broken apart and MC is fully exposed to the ambient current, MC dissolution from the solid phase to the aqueous phase is controlled by the dissolution rate. Once dissolved, the MC plume is advected away by the ambient current. Therefore, under this low-order detonation scenario, MC release follows the dissolution-controlled release process. The release function, Eq. (12), derived for release through a hole, can be modified for this scenario:

$$F = A_S \mu C_s, \quad (13)$$

where the term $1/b$ in Eq. (12) is infinitely small (hole is so large that $1/b \sim 0$) and the solid-water interfacial area of the semi-sphere, $2\pi R^2$, is replaced by surface area of the MC solid-water interface (A_S). For this scenario, A_S may be obtained from field observation/data. Therefore, release of MC under a low-order detonation scenario depends on the integrity of the exposed MC, represented by the total contact surface area between the remaining active MC matrix and the aqueous phase.

3.3 EMPIRICAL STUDY – UNBURIED SHELL

3.3.1 Experiment Test Platform

All mass release experiments were conducted in a tiltable re-circulating open-channel flume in the hydraulic lab at University of Wisconsin-Milwaukee. The flume consists of a head tank, a tail tank, and a test section (Figure 9 and Figure 10). The channel is 60-feet long, and 2.5-feet wide, with a water depth up to 2 feet. The two side walls of the test section are made of glass, allowing excellent optical viewing. The slope of the channel is adjustable, with the water flow driven by a centrifugal pump. The flow rate of the channel can be adjusted by varying the pump speed, the channel slope, and using a valve simultaneously. Water is sucked from the tail tank by the pump, carried through a pipe underneath the flume, and upwells into the head tank. It then flows through a series of grids that

regulate the flow condition to generate a uniform mean current with a homogeneous turbulence distribution in the test section. All measurements were conducted at a location about 35 feet downstream of the inlet, where a mass release test platform was placed.

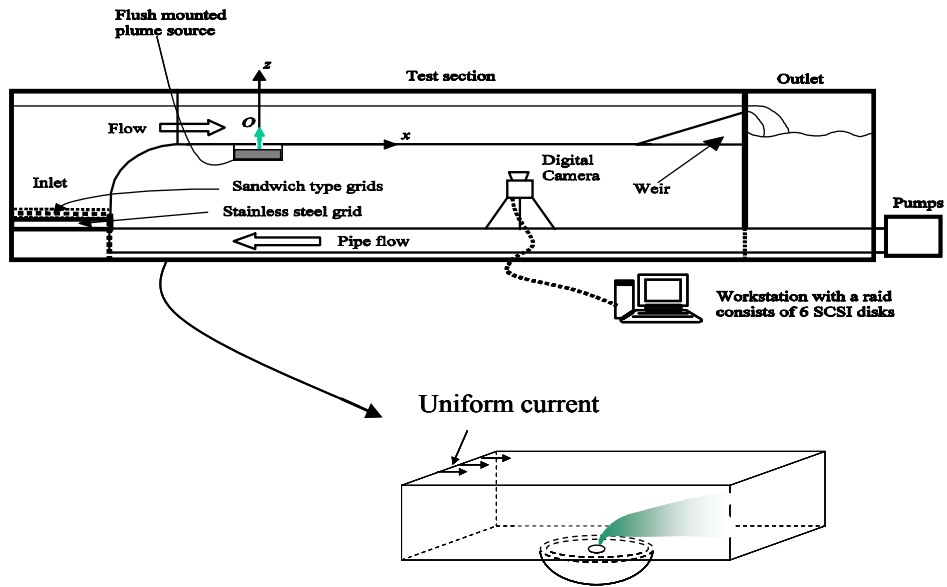


Figure 9. Re-circulating flume tank and the conceptual release from the half dome.

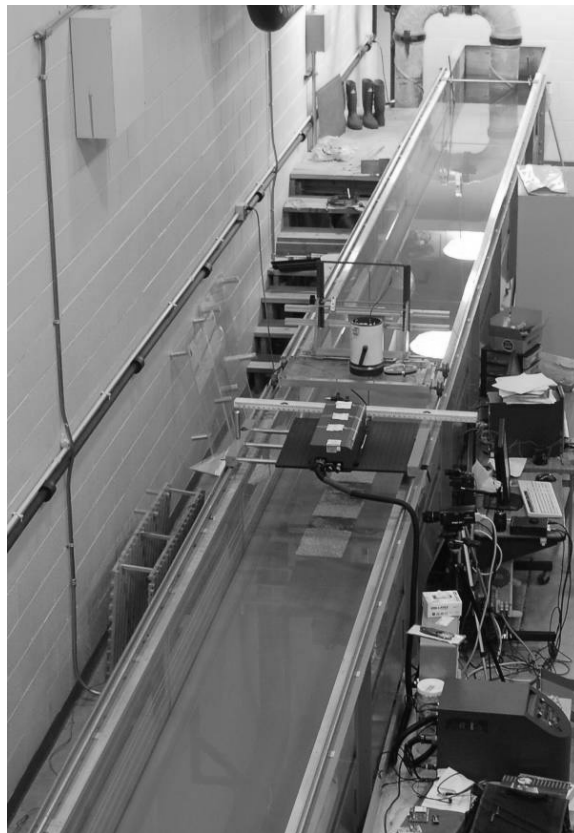


Figure 10. Test section of open channel flume at UWM hydraulic lab.

A mass release platform was constructed to create an ideal uniform flow over a smooth surface. The platform was made of polycarbonate plates with thickness = 1 inch, a total length of 4 m, and width of 0.75 m (about equal to the width of the flume). The platform was placed in the open channel, supported by aluminum rods and was elevated to 10 cm above the flume bed. Breached cavities were modeled from semispherical acrylic domes. Breached surfaces were made of 1/8-inch thick circular acrylic sheets, which were glued to the cavity dome using silicone sealer. Circular holes or line cracks of various sized were machined by drilling through the covering sheets over the glued cavity domes. Modeled cavities with breached holes/cracks were then flush-mounted onto the flow platform with the center of holes/cracks located 3 meters downstream of the leading edge of the platform. Figure 11 shows the designed interchangeable mass release test platform. The experimental system was designed in such a way that cavities with different breach sizes, shapes, and inner radii could be easily mounted on the same platform. For each designed flow condition, experiments commenced once the flow reached a uniform condition along the mean stream direction at the location of the breach.

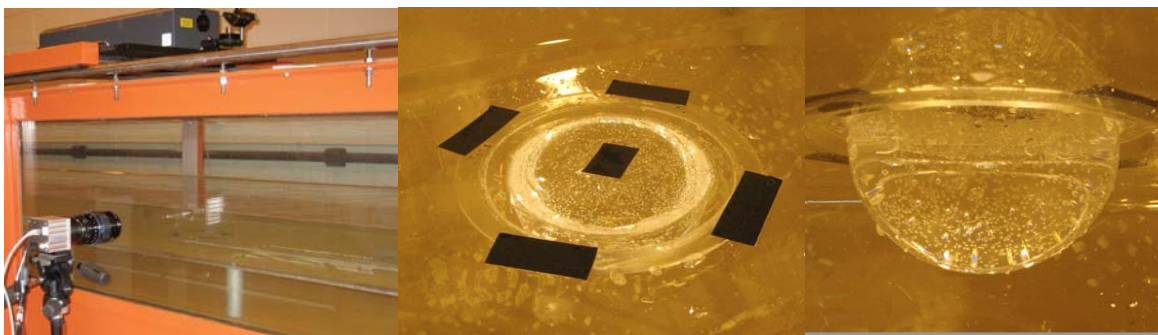


Figure 11. Model flow platform and shell cavity.

3.3.2 Measurement Techniques

To characterize the external shearing flow above the breach, as well as the induced in-cavity circulation, PIV was applied to measure the 2-D instantaneous velocity field. The PIV system consisted of a high-resolution, cross-correlation CCD camera, a dual-head Q-switched laser, a set of optics, and a PC-based image acquisition system. The CCD camera was an ImagerPro X manufactured by LaVision Co (<http://www.lavision.de>). It has a maximum resolution of 1600 x 1200 pixels and a 14-bit pixel dynamic range. The maximum frame rate at full resolution is 15 Hz. Image data streams into a dedicated computer system through a CameraLink interface, and is directly saved to a computer hard drive. In this study, a frame rate of 10 Hz was selected, along with an image resolution of 1200 x 1200 pixels. The Q-switched laser was a Solo XT PIV made by New Wave Research (<http://www.new-wave.com>). It is a laser diode-pumped Nd:Yag green laser (light wavelength = 532 nm) with a maximum repetition rate of 15 Hz (15 pairs of pulses per second). The duration of each laser pulse is 20 ns and the light energy is 200 mJ per pulse. A programmable timing unit (PTU) was used to send controlling signals to trigger and synchronize the laser and camera. Image acquisition and timing controls are integrated into the LaVision software, DaVis 7.2.

Fluorescein was selected as a surrogate for MC because fluorescein: 1) exists in both solid and aqueous phases under room temperature, and 2) is measurable by a fluorometer with high accuracy. Subsequently, the study shows that the molecular diffusivity (kinematic) of fluorescein in water at 20° C is 5.05×10^{-10} (m²/s) is on the same order of magnitude as that for TNT (10^{-10} m²/s), both being much smaller when compared with the hydrodynamic diffusion ($\sim 10^{-6}$ m²/s) for the smallest breach size and current investigated of 0.05 m/s, which governs the release rate. Therefore, for the cases we

studied, the molecular diffusivities of MC are not directly relevant to the study results but are still considered appropriate for modeling the release rates of MC.

The 2-D instantaneous concentration distribution of fluorescein solution was measured using planar laser induced fluorescence (LIF). The molecular diffusivity (kinematic) of fluorescein in water at 20°C is 5.05×10^{-10} (m²/s). The peak absorption of fluorescein occurs at 494 nm and the emission peak at 521 nm. A DPSS CW laser (www.laserglow.com) with wavelength of 473 nm and 300 mW of light power was applied to excite the dye solution. The laser beam was steered by an optical scanner (Cambridge Technology 6210H galvanometer) to cut across the dispersing fluorescein plume emitted from the breach. The resulted laser “sheet” was perpendicular to the direction of the mean current in the open channel, and placed at a location downstream of the breach hole (20~30 cm) where the plume was picked up by turbulent eddies, grown to a larger size and sufficiently diluted. This was considered an important step to increase the accuracy of concentration measurement, as the linear relation between the fluorescein concentration and the emitted light intensity is optimal at lower concentrations. In addition, laser light attenuation becomes less of an issue at lower concentrations. A mirror was placed downstream of the laser sheet, forming a 45-degree angle from the mean flow direction. A CCD (Point Grey Research, FI) IEEE 1394 camera with 1032 x 776 pixel resolution was introduced from the channel sidewall to collect images of the fluorescent light emitted from the dispersing dye. An USB-based analog output module (Data Translation DT9810) was used to generate signal waveforms to synchronize the shutter of the CCD camera and the scanning angle of the galvanometer.

3.3.3 Procedures

The first set of experimental studies was developed to examine the dominant factors that determine the mass release rate from a breached hole. According to our hypothetical analysis, the three controlling parameters were the radius of the semispherical cavity (R), the radius of the crack hole (b), and the shear velocity above the breached surface (u_*), where the shear velocity over a smooth wall has a well-known relation with the ambient flow speed (U). We selected three cavity radii, $R = 2.0, 3.5,$ and 5.8 (cm) and five hole radii, $b = 0.5, 2.5, 5.0, 10.0,$ and 25.0 (mm), respectively. Repeatable flow conditions were established with three nominal free stream speed, i.e., $U = 7, 15,$ and 31 cm/s, and the corresponding shear velocities were about ($u_* = 3.4, 6.7,$ and 11.2 mm/s). These were referred to as “Low Current,” “Median Current,” and “High Current” conditions hereafter. As a first-order approximation, we hypothesized that the time scale of mass depletion was related to the volume of the cavity ($V = 2/3\pi R^3$), the area of the hole ($A = \pi b^2$), and the shear velocity (u_*). For dissolved MC (no solid MC replenishment), a characteristic time to depletion can be defined as

$$t_D = \frac{V}{Au_*} = \frac{2R^3}{3u_*b^2}. \quad (14)$$

In this study, the combination of the selected R and b forms a wide range of characteristic depletion times (from 8 to 77,657 seconds). Table 1 shows the series of R and b and the corresponding t_D under the shear velocity $u_* = 6.7$ mm/s (the median current condition).

Table 1. Characteristic depletion time (seconds) under the combination of cavity radius and hole radius under the median current condition.

t_D	$b = 0.5$ (mm)	$b = 2.5$ (mm)	$b = 5$ (mm)	$b = 10$ (mm)	$b = 25$ (mm)
$R = 2.0$ cm	3,184	127	32	8	N/A
$R = 3.5$ cm	17,065	683	171	43	7
$R = 5.8$ cm	77,657	3,106	777	194	31

The order of measurements with different combination of b and R were randomized. First, the channel flow was set up at a desired current speed that was kept unchanged. PIV was then applied to characterize both the near-breach external flow and the induced in-cavity circulation (Figure 12 and Figure 13). A pulsed laser sheet was then delivered from the top of the channel. The light sheet was parallel to the mean flow direction, perpendicular to the breached surface, and cut through the semispherical cavity in the middle. Since the physical model is made of optically clear acrylic, it allowed excellent optical viewing (for both the laser light and the imaging device) to the inner space of the cavity. Profiles of the external mean current speed $U(z)$ and the Reynolds shear stress $-\overline{u'w'}(z)$ were determined from ensemble averaging instantaneous velocity fields measured more than 10 minutes. Thus, the shear velocity u^* could be estimated by either fitting the profile of U with the log-law (hydraulically smooth boundary), or taking the square root of the maximum value of the $-\overline{u'w'}$ profile. Measurements on internal circulations were followed to determine the temporal and spatial variation of circulation patterns and magnitudes.

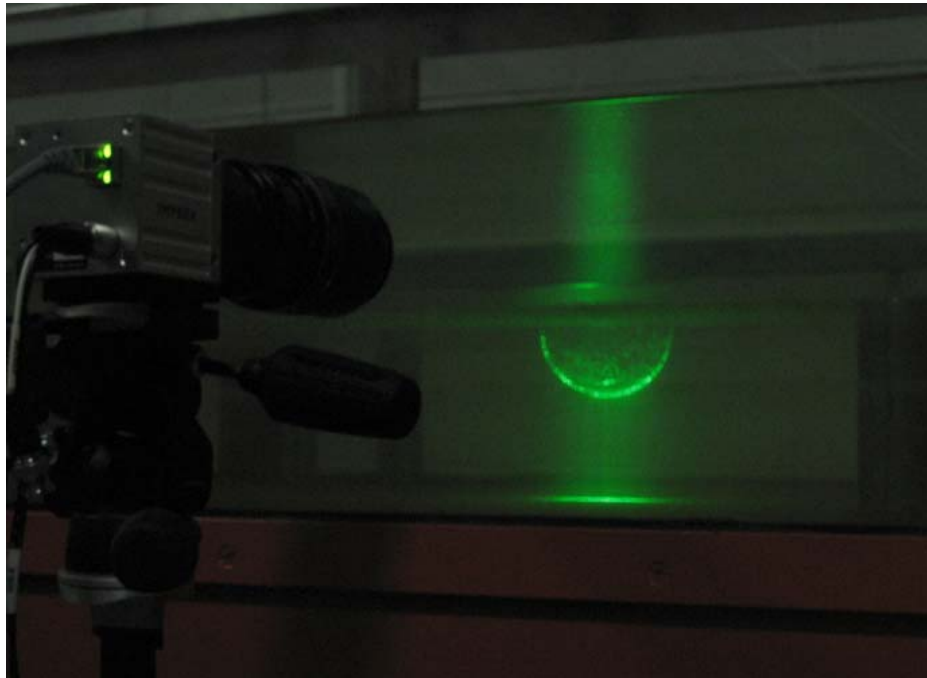


Figure 12. PIV measurement (with laser sheet).

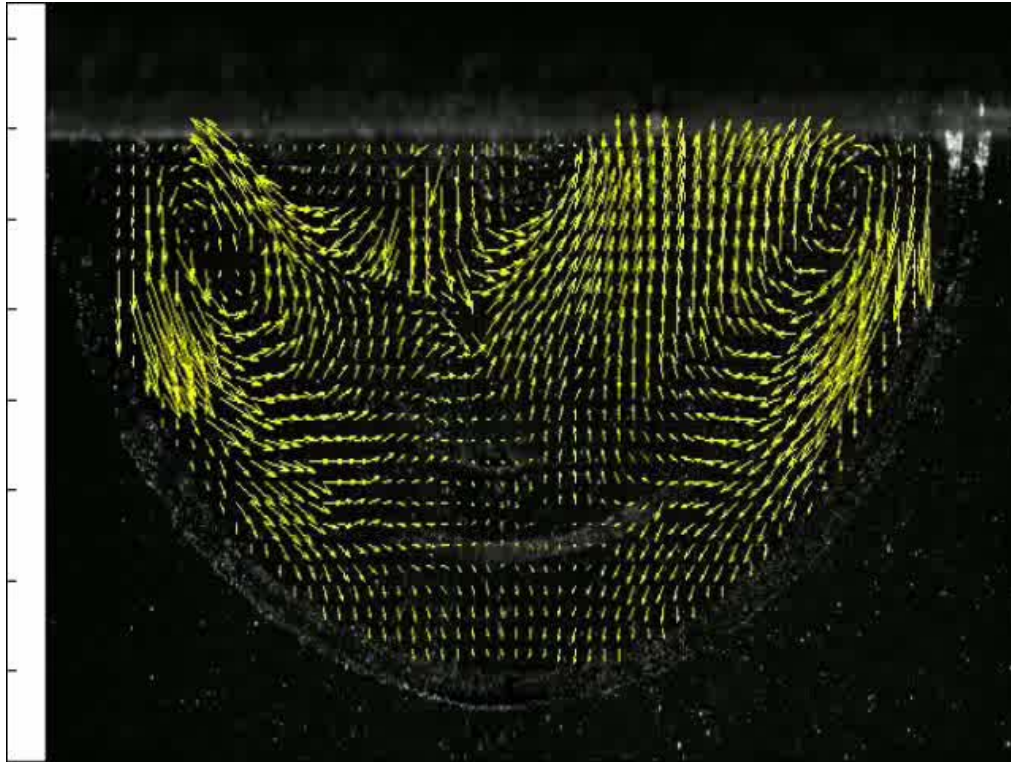


Figure 13. Measured internal flow circulation from the PIV images.

After the PIV measurements, the cavity model was taken out and refilled with a well-mixed fluorescein solution. Then the crack hole was sealed with waterproof tape and the cavity was mounted back on to the platform. LIF image sequence acquisition was then initiated quickly after the seal was removed and a fluorescein plume started to emit from the breach opening. The instantaneous concentration distribution on a 2-D cross-flow downstream section was measured using LIF at a rate of 1 Hz over 400 seconds (400 images) (Figure 14). In essence, the time scale of mass depletion is tabulated in Table 1. Depending on whether the depletion time was much smaller than, greater than, or the same order as the duration of LIF measurements, the mass depletion rates are estimated with different methods, which will be explained in Section 3.4.4.

Calibration measurements were also performed to relate the measured concentration to that of the source, under the assumption that the source was initially well mixed before it was injected in the modeled cavity. Using a pipette (5 ml), samples of dye solution were withdrawn from the cavity before and after each LIF measurement. The samples were then injected into a small aquarium and diluted 1700 times by adding clean water into the aquarium. The concentration of the diluted source was then measured by LIF using the same optical configuration as in flume experiments. This concentration, modified by the dilution factor (1700x) is the concentration of the source, which was used to normalize the plume concentration measurement and to estimate the total mass depleted through the hole during the flume LIF measurement.

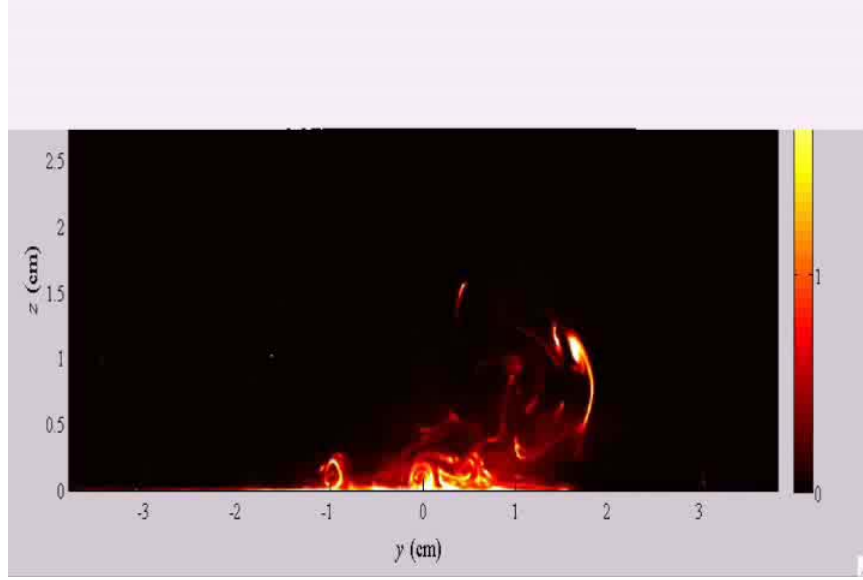


Figure 14. Measured fluorescein concentration processes from the LIF images on a cross-section downstream across the plume.

3.3.4 Estimation of the Mass Release Rate, F

The instantaneous chemical mass release rate can be experimentally determined by measuring the streamwise release of dye concentration at a downstream cross-section. In theory, the mass release rate is

$$F = \iint_A u(y,z)c(y,z)dydz, \quad (15)$$

where A is the downstream cross section, y and z are the spanwise and vertical coordinates, and u and c are fluctuating streamwise velocity and dye concentrations. According to Reynolds decomposition, they can be written as

$$\begin{aligned} u(y,z) &= U(z) + u'(y,z) \\ c(y,z) &= C(y,z) + c'(y,z), \end{aligned} \quad (16)$$

where the U is the ensemble mean velocity, which is assumed to be homogenous along the spanwise direction, thus only a function of z , and u' is the turbulent fluctuation. Similarly, C is the ensemble mean concentration and c' is the fluctuation. Thus, it can be shown that for a statistically steady state, the temporally averaged total flux rate is

$$\bar{F} = \int \left[U(z) \left(\int C(y,z)dy \right) \right] dz + \iint_A \overline{u'(y,z)c'(y,z)} dydz, \quad (17)$$

where the two integrals on the right-hand side are the mean current flux and the turbulent flux, respectively. Previous studies in the flume laboratory indicate that the turbulent flux in the streamwise direction is generally an order of magnitude smaller than the mean flux. Therefore,

we assume the turbulent flux in our measurement to be \gg mean current flux, and use the mean flux to estimate the mass release rate. Note that it is technically impractical to measure the streamwise turbulent flux over a cross-stream section, although it can be done over a plane that is parallel to the mean flow.

For the MC release rate measurements reported here, the mass release rate is not statistically steady, especially for the characteristically small depletion time t_D . The temporal variation of releaserate cannot be avoided in these cases, as there is no dissolution interface in the currently designed system. Based on the argument above, the instantaneous release rate was approximated by ignoring the correlation between the fluctuating part of the velocity and the instantaneous concentration, so we have

$$F(t) = \int_0^H \int_{-W/2}^{W/2} U(z)c(y,z)dydz, \quad (18)$$

where H is the height of the image above the flume bed and W is the width of the image.

The mass release rate was determined as statistically steady over the period of image acquisition (i.e., without obvious longterm trend) if the t_D is large (e.g., > 400 s). Otherwise, the observed mass release decreases in a log-linear fashion with time. Figure 15 shows a time series of $F(t)$ for typical small, medium, and large values of t_D . Note: for small and medium t_D , the figure is presented in a semi-log fashion. Dashed lines are fitted to exponential functions with respect to time.

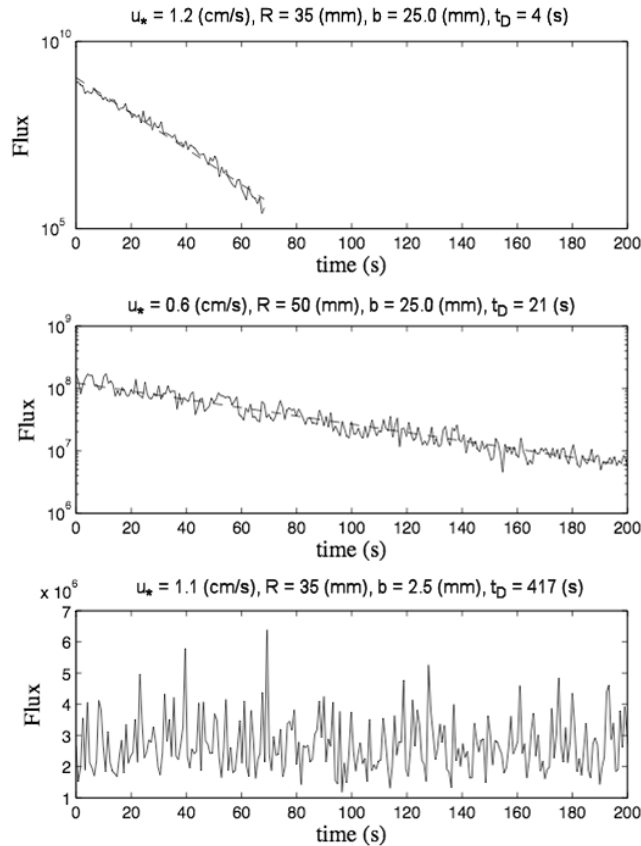


Figure 15. Time series of measure mass release rate with small, median and large depletion time scale, t_D .

For scenarios with large values of t_D , like the third scenario in Figure 15, we can assume the mass release rate is quasi-steady state. Thus, the ensemble average of the recorded series of $F(t)$ is considered as the MC release rate, and we can assume a model of the mass release rate as

$$F = u_f A C_0, \quad (19)$$

where $A = \pi b^2$, the hole area, C_0 is the average concentration within the cavity, and u_f is the “release velocity.” The release velocity has previously been determined empirically as $0.023U$ according to FLUENT simulations (with $Sc = 1$), and $0.025U/Sc$ according to lab experiments with small hole radius. Our new data show that u_f could be a function of the hole radius and the cavity radius as well.

For smaller values of t_D , the observed log-linear trend is characteristic of a simple first order mass depletion model, which can be applied to describe the MC release:

$$V \frac{dC_0}{dt} = -F = -u_f A C_0, \quad (20)$$

where C_0 is the average concentration in the cavity, as it decreases with time. Eq. (20) indicates that the decreasing release rate can be modeled as

$$F = u_f A \tilde{C}_0 \exp\left(-\frac{u_f A}{V} t\right), \quad (21)$$

where \tilde{C}_0 is the initial in-cavity concentration, which can be determined through the calibration experiment. Linear regression can be applied to $\log(F)$ vs. t to determine the release speed u_f .

3.3.5 Shear velocity u_*

We have argued that mass release rate from a small breach should be scaled with the surrounding flow structure that has a comparable scale as the breach hole itself. Therefore, the shear velocity above the breached surface is selected as one of scaling parameters. A relationship between the ambient current speed and the shear velocity can be established based on the roughness and orientation of the surface. Therefore, it will be convenient to separate the Reynolds number of the overall flow and other factors, so that we can focus on the fundamental mechanisms that control mass release through a small opening.

In our previous studies, mass release rate has been associated with the depth-averaged velocity (or the ambient current speed). Here we present the relationship between shear velocity and ambient speed under the scenario of simple uniform flows over a smooth surface. Most of our experiments were conducted in three groups. For each group, three nominal flow speeds were established: low, median, and high. Vertical profiles of mean velocity and Reynolds shear stresses of the nine flows are shown in Figure 16.

Shear velocity u_* was estimated as the square root of the peak value of $-\overline{u'w'}$. The ambient current speed U was estimated as the depth-average of the vertical profile of the mean velocity. These values and the ratio u_*/U are listed in Table 2.

Our previous study has indicated that for general cases, the mass release velocity is $u_f = 0.025U$. With the new scaling parameter u_* , we should expect that $u_f = 0.50 \sim 0.63u_*$, since u_*/U is about 0.04 to ~ 0.05 (Table 3).

3.3.6 Mass Release Velocity u_f vs. Shear Velocity u_*

For a large depletion time, measured mass release rate F was normalized by the calibrated source concentration and divided by the crack area to deduce the mass release velocity u_f . For a smaller depletion time, first-order depletion model, log-linear regression analysis based on Eq. (20) was directly applied to deduce the release speed u_f . For the median depletion rate, both methods were applied and the average of the two results were chosen as the mass release velocity.

First, the mass release velocity was plotted against the shear velocity for all combinations of R and b , as shown in Figure 17. Generally, u_f increases almost linearly with u_* for most cases. If we apply linear regression of $u_f \sim u_*$ for each pair of R and b , and force the intercept to be zero, the scaling between u_f and u_* can be determined, and the results are listed in Table 4.

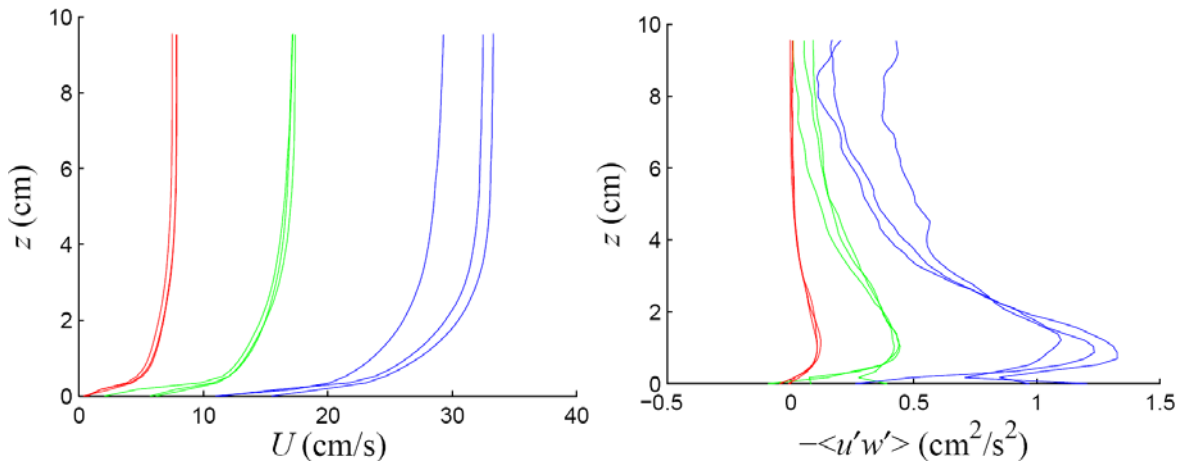


Figure 16. Vertical profiles of the mean velocity and the Reynolds shear stress.

Table 2. Shear velocities and ambient current speed (cm/s).

	Low Speed			Median Speed			High Speed		
	u_*	U	u_*/U	u_*	U	u_*/U	u_*	U	u_*/U
Group 1	0.328	6.756	0.049	0.667	15.692	0.043	1.152	31.306	0.037
Group 2	0.351	7.113	0.049	0.663	15.943	0.042	1.097	27.087	0.041
Group 3	0.330	7.133	0.046	0.649	15.360	0.042	1.111	30.290	0.037

Table 3. Scaling between the mass release speed and the shear velocity, u_f/u_* .

u_f/u_*	$b = 0.5$ (mm)	$b = 2.5$ (mm)	$b = 5$ (mm)	$b = 10$ (mm)	$b = 25$ (mm)
$R = 2.0$ cm	0.44	0.49	0.51	0.50	N/A
$R = 3.5$ cm	0.84	0.90	0.97	1.25	1.17
$R = 5.8$ cm	1.68	1.69	1.62	1.97	1.69

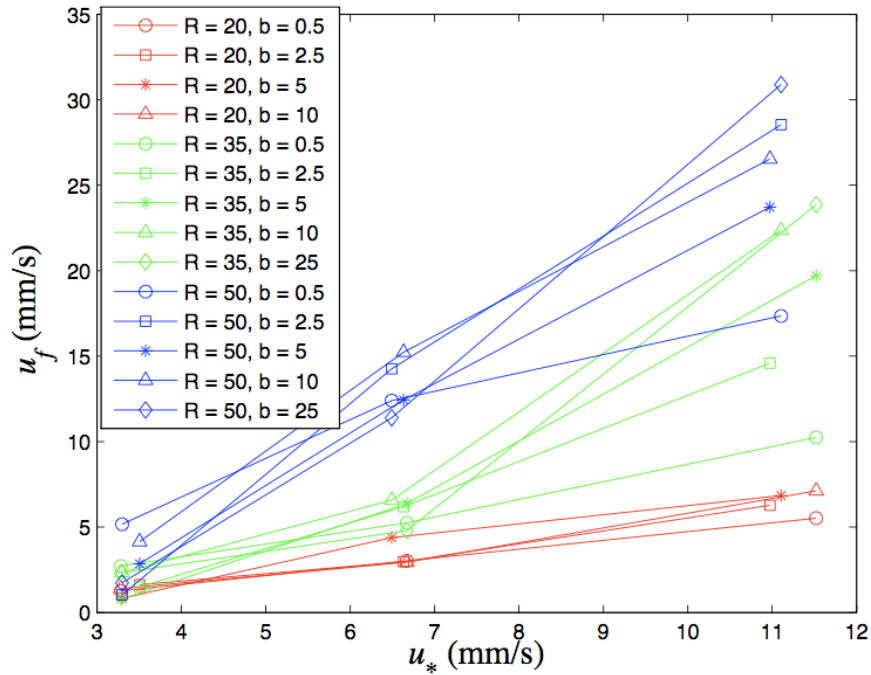


Figure 17. The relation between mass release speed u_f , and shear velocity u_* .

According to our empirical results, $u_f = 0.44 \sim 1.97 u_*$, a much wider variability than our preliminary simulation results.

3.3.7 Effect of Crack Hole Radius b on the Release Speed u_f

According to the values listed in Tables 4 and 5, the scaling factor between u_f and u_* seems to slightly increase with the crack hole radius for all the different cavity radii R . By grouping measured u_f/u_* with the hole radius b , a single factor ANOVA shows that the dependency of u_f/u_* on the hole radius is not significant (P -value = 0.93) (Table 4).

Table 4. ANOVA results for u_f/u_* dependence on hole radius.

SUMMARY				
Groups	Count	Sum	Average	Variance
B = 0.5	3	2.96	0.986666667	0.400533333
b = 2.5	3	3.08	1.026666667	0.372033333
B = 5	3	3.1	1.033333333	0.311033333
B = 10	3	3.71	1.236666667	0.540233333
B = 25	2	2.81	1.405	0.11045

ANOVA						
Source of Variation	SS	df	MS	F	P-value	F crit
Between Groups	0.305254762	4	0.07631369	0.204526311	0.929521104	3.633088512
Within Groups	3.358116667	9	0.373124074			
Total	3.663371429	13				

3.3.8 Effect of Cavity Radius R on the Release Speed u_f

According to the values listed in Tables 4 and 5, the cavity radius has a strong effect on the scaling factor between u_f and u_* . By grouping measured u_f/u_* ratio with cavity radius R , a single factor ANOVA verifies that the non-dimensional u_f/u_* increases with R significantly (P-value = 1.28×10^{-7}) (Table 5).

3.3.9 Observed Universal Function for Mass Release Speed

If we exclude the hole radius b , a simple dimensional analysis shows that the normalized mass release speed u_f/u_* should be a function of the cavity radius based Reynolds number:

$$\text{Re}_R = \frac{u_* R}{\nu}, \quad (22)$$

where ν is the kinematic viscosity. Figure 18 shows the scaling factor u_f/u_* versus Re_R for all the measurements. A linear regression analysis indicates that

$$\frac{u_f}{u_*} = 0.0042 \text{Re}_R + 0.0492, \quad (23)$$

with the correlation coefficient $R^2 = 0.7227$.

Table 5. ANOVA results for u_f / u_* dependence on cavity radius.

SUMMARY						
Groups	Count	Sum	Average	Variance		
R = 10	4	1.94	0.485	0.000966667		
R = 35	5	5.12	1.024	0.03003		
R = 50	5	8.6	1.72	0.02035		
ANOVA						
Source of Variation	SS	df	MS	F	P-value	F crit
Between						
Groups	3.458951429	2	1.729475714	93.06444016	1.27801E-07	3.982297957
Within Groups	0.20442	11	0.018583636			
Total	3.663371429	13				

3.4 EMPIRICAL STUDY – BURIED SHELL

3.4.1 Pore-water Flow Experiment

A pore-water tank was designed and fabricated to study the release rate of tracer dye from a buried breached dye container to simulate MC from buried shells. The tank includes two constant depth water reservoirs and a connecting porous media channel. The overall configuration and dimension of the tank is shown in Figure 19.

Hydraulic pressure drove the seepage flow through the porous media channel and was achieved by maintaining constant water levels in the two reservoirs. Water was continuously pumped into the high-head reservoir and drained through one of the three holes to maintain a desired water level. As water seeped through the porous media, it upwelled into the low-head reservoir and eventually drained through the hole (see Figure 19(b)). The system was designed such that head difference on

the two sides of the porous media channel can be 1, 2, or 3 inches, respectively. Throughout this study, the resultant seepage flow conditions are called: “low,” “medium,” and “high” flow conditions, respectively.

Figure 20 shows the operation of the pore-water tank. The head difference used in this case is 3 inches. Two types of clean sand were used to model the coastal water sediment: fine sand (mean diameter $d_s = 150 \mu\text{m}$) and coarse sand (mean diameter $d_s = 500 \mu\text{m}$). The estimated parameters for the two types of sand are given in Table 6 (the estimation of conductivity will be detailed in the following paragraphs).

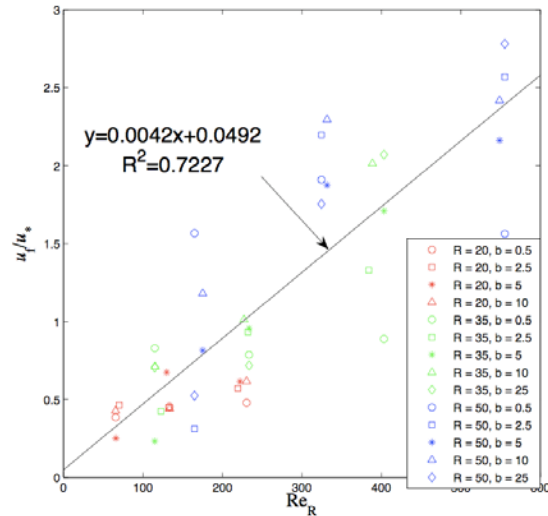


Figure 18. Normalized release speed vs. cavity radius based Reynolds number.

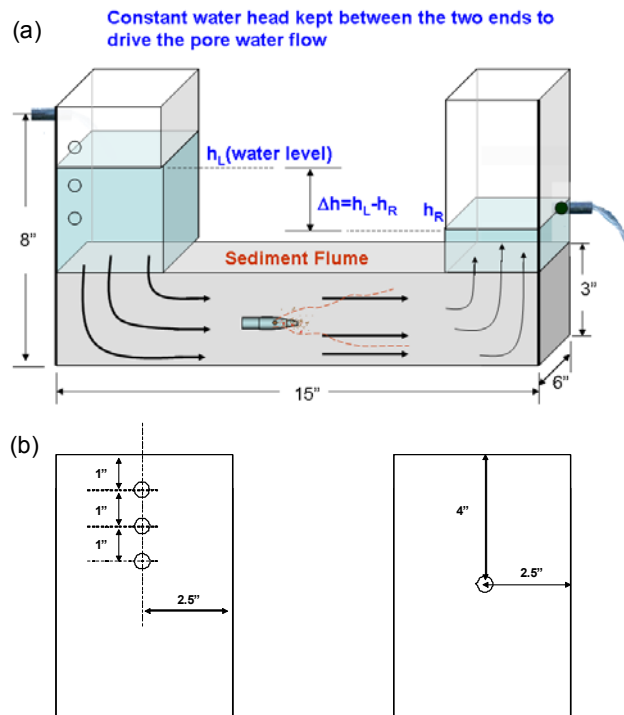


Figure 19. (a) Schematic of the pore-water tank; (b) Drain holes on the sidewalls of the high-head and low-head reservoir.

Table 6. Physical properties of sand in the dye release experiments.

Parameter	Fine sand (150 μm)	Coarse sand (500 μm)
Porosity	31%	28%
Hydraulic conductivity (cm/s)	0.011	0.065



Figure 20. Dye tracing in the pore-water flow tank.

Pore-water seepage velocity was measured through dye visualization (Figure 20), and was found to be slightly non-uniform over the depth of the channel. Under a typical medium flow condition, the seepage velocity was about $u_s = 0.20$ mm/s near the top wall, and decreased with depth until 1.2 inches below the top wall. It then became nearly uniform ($v = 0.16$ mm/s) over a 1.5-inch thickness above the bottom wall. The vertical profile of the seepage velocity was similar under all flow conditions. During the dye release experiments described in the next section, the modeled shell was buried at ~ 1 inch above the bottom wall. The local seepage velocity was then estimated using the measured total discharge and the estimated vertical velocity profile,

$$u_s = 0.88Q/(A\varepsilon), \quad (24)$$

where the Q is the total discharge, ε is the porosity, A the area of the channel cross-section, and 0.88 was the mean correction coefficient that accounts for non-uniformity of all the flow profiles.

A 2-D numerical model was developed to simulate the flow conditions using the Matlab Partial Differential Equation Toolbox (see Section 3.8 for details). The model solves for the distribution of piezometric (hydraulic) head h over the sandy matrix. The Darcy velocity is then evaluated as $\bar{q} = -K\nabla h$. Figure 21 shows the simulated result, the simulation corresponds closely to the experimental observation in terms of the visualized flow streamline. It also shows that the Darcy velocity vectors are nearly horizontal in most regions of the test section.

Figure 22 shows the plot of the averaged head gradient function, $G = -W \int_0^H (\partial h / \partial x) dy$ (where $H = 3$ in, the height of the channel, $W = 5$ inches, the width of the channel), as a function of the distance x (from 0 to 14.5 inches). It reaches a nearly constant value in the central part of the test section, indicating a uniform flow condition. Thus, we can use the measured discharge Q and the simulated result G (at the constant value of the horizontal flow test section) to estimate the hydraulic conductivity, $K (= Q/G)$. Using this approach for both types of sediment, we found $K = 0.011$ (cm/s) for the fine sand and $K = 0.065$ (cm/s) for the coarse sand (see Table 6, above).

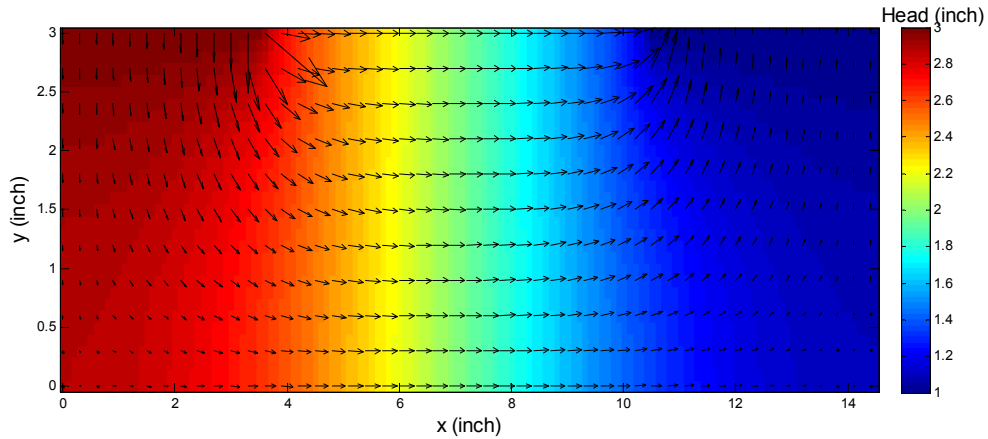


Figure 21. Numerical model simulation result of the flow in the pore-water tank.

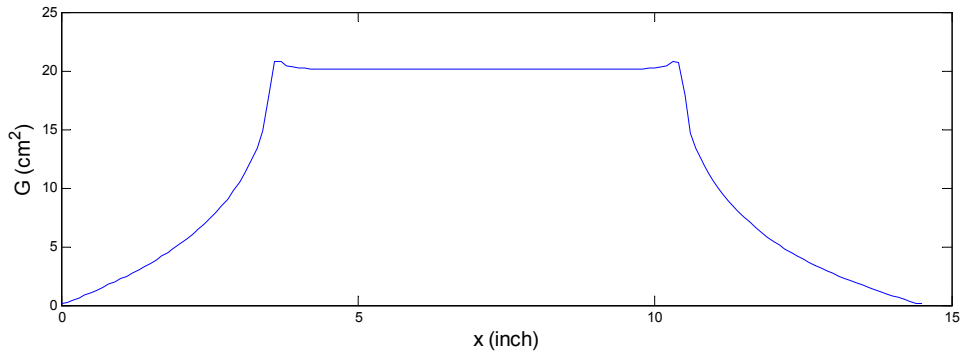


Figure 22. Averaged head gradient function plot.

Table 7 lists the typical discharge values for porous media flow, in addition to the estimated seepage velocity near the buried shell under three typical flow conditions for fine and coarse sand structures.

Table 7. Pore-water flow conditions.

	Flow conditions	Head difference (cm)	Discharge (ml/hour)	Average Darcy velocity (v-mm/s)	Average Seepage Flow velocity (u_s -mm/s)	Seepage Flow velocity around the shell (u_s -mm/s)
Fine sand	Low	2.54	263	0.008	0.026	0.023
	Medium	5.08	514	0.015	0.048	0.042
	High	7.62	815	0.023	0.074	0.065
Coarse sand	Low	2.54	1600	0.046	0.163	0.143
	Medium	5.08	3250	0.093	0.332	0.292
	High	7.62	4380	0.125	0.446	0.393

3.4.2 Dye Release Experiments

Based on the sandbox porous flow (Figure 19 and Figure 20), the dye release experiments were conducted as visualized in Figure 23. A small glass bottle (4-cm high and 2.5-cm in diameter, inner volume = 11 ml) with a small circular hole drilled in the cap that was used as a surrogate for a breached shell (Figure 24). The experimental methodology used is described as follows. The bottle, filled with Rhodamine WT fluorescent dye solution (molecular diffusion coefficient in water $D = 1.5 \times 10^{-4} \text{ cm}^2/\text{s}$) of known concentration (usually $C_0 = 400 \text{ ppm}$), was placed in the lower portion of the porous media channel, with its hole at 5 cm above the bottom and the breached surface parallel to the mean flow direction. As the dye was transported with the pore-water movement, it upwelled into the low-head reservoir where it was mixed by air-induced turbulence at the water surface generated from a small fan. Finally, well-mixed dye was drained from the low-head reservoir where it was collected by a flask and remixed. A fluorometer (Turner Designs Cyclops) probe, submerged in the flask, was used to measure and record the concentration of the exit dye continuously at a frequency of one sample every 10 minutes. Thus, the flux rate (F) of dye (as MC surrogate) can be estimated as

$$F = QC_{\text{out}}, \quad (25)$$

where Q is the discharge of the groundwater flow and C_{out} is the exit dye concentration in the flask.

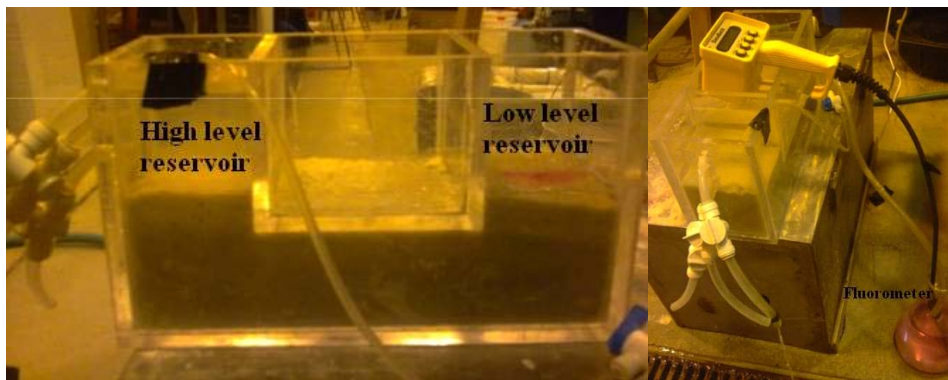


Figure 23. Dye release and flux experiments.



Figure 24. The container with a breach hole ($d_b = 0.56$ cm) used as an experimental breached munition surrogate.

Three breach hole diameters were used in these experiments: $d_b = 0.21$, 0.4 , and 0.56 cm. The dye release experiment consisted of 18 runs, with three different breach diameters, three flow conditions, and two types of sand. Each test run lasted for at least 24 hours, or until 50% of the total dye mass was released from the breach hole.

3.4.3 Mass Depletion Analyses

A dimensional analysis allows us to postulate the following MC release rate model,

$$F = C_0 A u_f, \quad (26)$$

where C_0 is the mass concentration near the breach, A is the area of the breach, and u_f is a mass release velocity, measured experimentally. A similar model was used to estimate the rate of release from a breached hole in flowing water.

Once the dye is released through the crack of the container, subsequent transport is determined by pore-water advection and dispersion in the sediment channel. It is also assumed that the fluorescent dye in the container is well mixed, i.e., $C = C_0$ everywhere in the container. This assumption is reasonable as the mass flux is expected to be low due to the low seepage velocity, thus the time scale for diffusion within the cavity is short compared with the timescale for the overall mass depletion, allowing the release rate to be expressed as the following simplified equation:

$$F = \frac{d(C_0 V)}{dt} = -C_0 A u_f, \quad (27)$$

where V is the volume of the container. Therefore, the concentration decreases exponentially as follows:

$$C_0(t) = C_i \exp\left(-\frac{A}{V} u_f t\right), \quad (28)$$

where C_i is the initial dye concentration. Meanwhile, the concentration of dye exiting the reservoir is measured in addition to the flux (Eqs. (25) and (26)), resulting in $QC_{out} = Au_f C_0$. If a simple first-order release model is correct, we would expect to see the concentration of the exit dye also decrease exponentially.

Therefore, we have,

$$\ln C_{out} = -\frac{A}{V} u_f t + \ln\left(\frac{A u_f}{Q} C_i\right). \quad (29)$$

Eq. (28) represents the analytical solution of the dye concentration in the container, which dilutes exponentially over time, whereas, Eq. (29) represents the analytical solution for the exit dye concentration which behaves similarly (exponentially decaying) to the dye concentration in the container. In addition, Eq. (29) can also be expressed explicitly as a function of flow parameters, u_f , Q , breach area (A), and volume (V) of the container. The analytical solution of the exit dye concentration (Eq. (29)) was compared with that measured from the dye release experiments in Section 4.4.2.

3.5 MODEL VALIDATION

3.5.1 Simulation Parameters

The algebraic analytical function for MC release was validated by the numerical simulation results using the FLUENT model. FLUENT is a general computational fluid dynamic model widely used in automobile and combustion industries. The FLUENT model includes a mesh generating software, GAMIT, which is flexible in generating model configuration and meshes for scenarios designed by the users. For this numerical modeling study, a numerical flume channel was used that was 1 m in length, 0.4 m in width, and 0.2 m in depth. A circular hole (radius = b) was “drilled” into the bottom of the channel. The hole was a representative of the breach hole in the shell, and it connected to a semi-sphere space (radius = R) beneath the flow channel as seen in Figure 25. The flume channel and the semi-sphere were filled with water. The inner surface of the semi-sphere was defined as the MC solid-aqueous interface, through which the MC dissolution occurs. Solution inside the semi-sphere cavity was released through the hole due to the current in the channel. The coordinate system was set such that the center of the hole was the origin, positive x was in the mean flow direction, y was in the cross-channel direction, and z was positive upward (normal to flow).

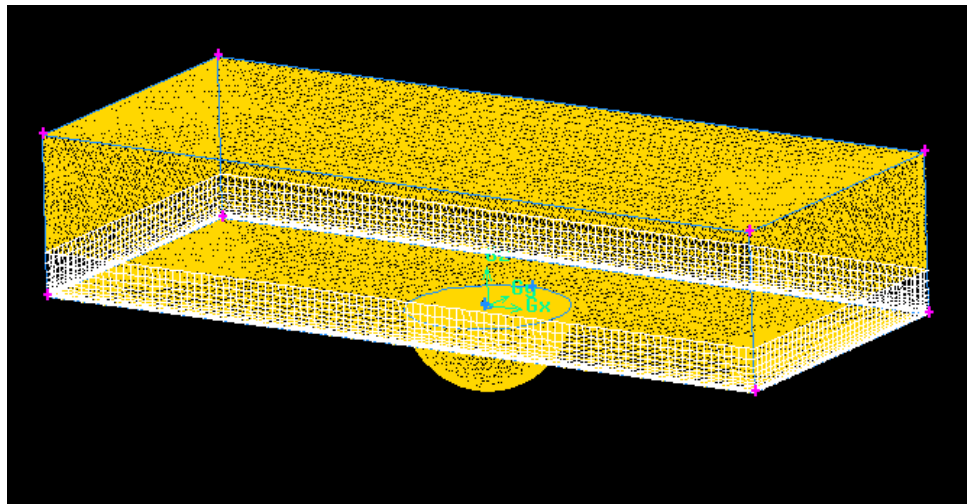


Figure 25. FLUENT model geometry and meshes generated by GAMIT.

Model meshes with variable sizes are generated, with an average grid size of 10 mm. Meshes are refined near the breach hole and the boundaries of the channel bottom. Meshes are then imported into FLUENT for numerical simulations.

A uniform in-flow profile with a velocity U is applied to the upstream cross-section of the channel. Flow is simulated as a laminar type with non-slip wall boundary condition. At the solid-liquid interface inside the semi-sphere ($r = R$, where r is the radial coordinate originating from the center of the hole pointing radially), the MC concentration is assumed to reach saturation ($C = C_S$). The molecular diffusivity of MC solution is assumed to be $D_M = 1.0 \times 10^{-9} \text{ m}^2/\text{s}$, *i.e.*, the Schmidt number of the MC solution, $Sc = \nu/D_M = 1$, where ν is the viscosity of water.

Steady-state solutions for both velocity field and concentration field are obtained by solving the segregated Navier-Stokes equation and scalar transport equations in FLUENT. Concentration flux induced by channel flow is evaluated by integrating the transport term UC over a selected downstream cross-section. Under steady-state conditions, the flux should be independent of location downstream of the breach hole. This is verified by calculating fluxes at four different cross-sections in FLUENT. Figure 26 shows a typical simulated concentration field displayed on the central vertical plane of the channel, a cross-section 25 cm downstream of the breach hole, the plane near the bottom of the channel, and a central vertical plane inside the semi-sphere. A saturation constant of 100 mg/L is assumed in this numerical model run. As is shown in Figure 26, solutions inside the semi-spherical source container retain concentrations $\sim 13 \text{ mg/L}$. Concentrations outside the hole are 0.2 to 0.5 mg/L which is rapidly reduced downstream ($\sim 0.002 \text{ mg/L}$, at a location 25 cm downstream).

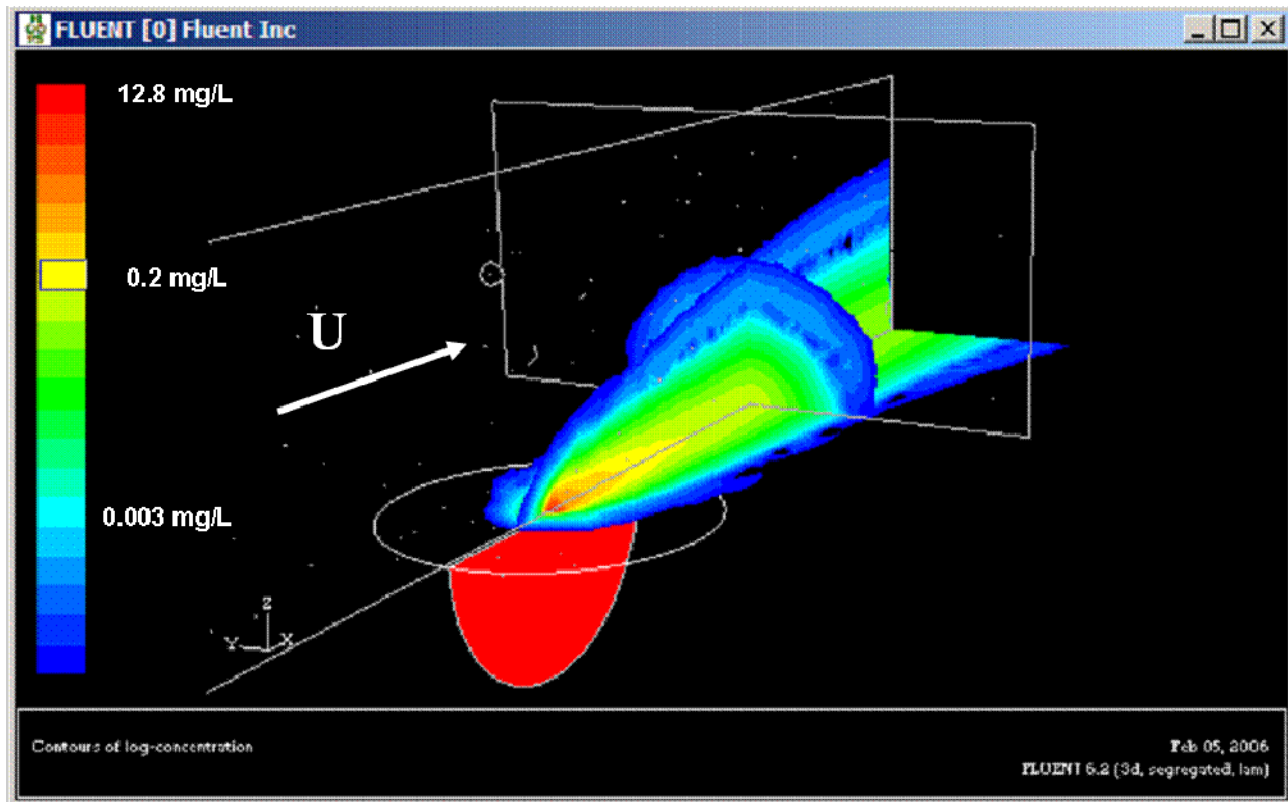


Figure 26. Contours of concentration on the central vertical plane and a cross-section. In this case, the breach hole is $b = 5 \text{ mm}$ in radius and the current speed is $U = 6 \text{ cm/s}$.

3.6 MODELING FATE AND TRANSPORT OF TNT, RDX, AND HMX

The release rate function, developed, and validated by FLUENT previously, provides release rates for a single shell under various hydrodynamic and shell integrity conditions. Since we do not have adequate information about the quantity and magnitude of breached shells in DoD coastal and estuarine waters, the following assumptions are made:

1. The release rate function, developed for this study, can be used to predict release rate for any single breached shell.
2. For multiple breached shells, the total release rates can be obtained by summing the release rates of each individual beached shell. This requires an estimate or assessment of the number and type of shells at a given site.

In the following example, we used two models to simulate the fate and transport of MCs released from breached shells, the hydrodynamic and transport model, TRIM2D (Cheng, Casulli, and Gartner, 1993; Wang *et al.*, 1998a and 1998b), and the USEPA's standard water quality model, WASP7 (Wool *et al.*, 2001; Ambrose *et al.*, 1992). We used San Diego Bay as the test site, since the hydrodynamics are adequately known and relevant data are available for modeling purposes. For both models, we choose a theoretical munition shell with the following dimensions shown in Table 9.

Table 8. Sizes and dimensions of the test breached shell.

Length (inches)	Diameter (inches)	Hole radius (mm)	Average current (cm/s)	MC Mass (kg)
24	8	20	8	8

For TRIM2D, which is a 2-D hydrodynamic and transport model, time-varying current speeds, predicted by the model, are input into the release rate function for the breached shell. The resulting release rates are time varying, fluctuating with ambient current speed. For WASP, a fixed averaged current of 8 cm/s is chosen, which is close to the tidally averaged current speed in San Diego Bay. Release rate for WASP7 is assumed to be a constant.

3.6.1 TRIM2D Model

TRIM2D is a depth-averaged tidal and residual circulation model with a finite-difference numerical grid and scheme. TRIM2D has been previously applied to simulate time-varying water surface elevation, averaged water-column currents, and associated transport of contaminants for several estuarine systems, including San Francisco Bay, California; Boston Harbor, Massachusetts; Charleston Harbor, South Carolina; and Venice Lagoon, Italy (Cheng, Casulli, and Gartner, 1993; personal communication). Over the past two years, SSC Pacific has applied TRIM to several water-resource and water quality studies for San Diego (Chadwick *et al.*, 1999; Wang, Sutton, Richter, and Chadwick, 2000; Wang, Chadwick, Johnson, and Grovhoug, 2006).

The use of a 2-D depth-averaged model such as TRIM is justified because field data show that the flow in San Diego Bay exhibits strong uniformity in the water column (Wang *et al.*, 1998a). Such uniformity of flow in the water column results from the fact that San Diego Bay is shallow and flow in the bay is primarily driven by tides from the Pacific Ocean. Other assumptions in model formulation included incompressibility of water and the Boussinesq approximation, which simplifies effects of density difference by only considering buoyancy (associated with gravity) and neglecting other high-order terms of density differences. As with any depth-averaged model, velocity and density are implicitly assumed as nearly constant over the water column. However, horizontal density gradients are treated explicitly in the momentum equations.

We approximated bottom shear stress using a Manning–Chezy formulation with Manning's n coefficient assigned as a function of water depth:

$$\tau_b = \rho u_*^2, \quad (30)$$

where τ_b is the shear stress at the bottom, ρ and u_* are water density and shear velocity, respectively.

The shear velocity is correlated with the Manning–Chezy relationship as follows:

$$u_* = \frac{g|V|V}{C} \quad (31a)$$

$$C = \frac{H^{1/3}}{n^2} \quad (31b)$$

where g is gravity, V is the current velocity (simulated), C is the Chezy coefficient, and n is Manning's n-value.

The empirically based Manning–Chezy formulation provides a closure to the bottom boundary. The only empirical parameter needed for TRIM2D is Manning's n-value, which is assumed to be a function of water depth.

An additional transport equation is used for each chemical species, to simulate solute transport. Solutes are assumed to be dilute (no more than 1000 parts per million), not affecting water density, and thus the solute transport equations are uncoupled from hydrodynamics. Furthermore, the transport equation is solved one time-step behind the continuity and momentum equations, effectively uncoupling the transport equation (Cheng, Casulli, and Gartner, 1993). This approach is valid because baroclinic forcing (i.e., density flow) changes less rapidly than barotropic forcing (gravity flow). The advective term in the transport equation is processed using an upstream differencing scheme that ensures conservation of mass as solutes are transported by advection. Similar numerical schemes were used in several previous studies, in which details about the formulation and previous applications of TRIM2D can be found (Wang, Mill, Martin, and Wool, 1997).

TRIM2D calculations reported here were compared with the 1983 tide data collected by the National Oceanic and Atmospheric Association (NOAA) at the Ballast Point, Downtown San Diego, and South Bay stations for San Diego Bay. We used tide data collected at the Scripps Piers as boundary conditions for the model. These data, along with the Manning's n-coefficients, were fine-tuned to fit the model-simulated tides against measured values. Once calibrated, we validated the model by independently simulating tides and currents, and then compared simulated results with measured tides and currents. Overall, the observed differences between model and measurements were less than 3% for tidal heights and less than 15% for tidal currents. The differences in tidal currents between the model and measurements may be attributed to multiple sources, including errors associated with tidal measurement and the approximation and simulation of 3-D flows by the 2-D, vertically averaged model (TRIM2D).

From a rest condition, we ran TRIM for 2 days (48 hours) to ensure that a steady-state flow condition was reached before the constant-load effluent entered into the bay. This initial 2-day run was necessary to eliminate transient flows that should not exist under steady-state, quasi-repetitive tidal conditions. We used a 6-minute time-step in the model and simulated tidal height and tidal

currents. Simulation for 1 year (365 days) was executed and results at the end of 365 days were analyzed. The Modeling Results sections of this report discuss the findings from this modeling study.

3.6.2 TRIM2D Model Setup

A 2-D rectangular numerical grid system (of dimensions 100 m x 100 m) was used for TRIM. These numerical grids cover the entire San Diego Bay and portions of open ocean outside the mouth of the bay, consisting of 30,845 grid cells with 21,563 water cells. Hydrodynamics of the bay is driven by ocean tides only and measured tides are prescribed along the west, south, and north boundaries of the model domain, which cover the entire ocean boundary.

Two simulation scenarios for TRIM were evaluated. The first scenario explores the release of MCs from a shell located at the south end of the inner bay, Figure 27, which resembles the loading scenario for the WASP7 model (Box #1). The second simulation scenario assumes that MC release occurs at the San Diego Naval Station near the middle of the bay. For both simulation scenarios, current speeds at both locations simulated by TRIM2D are used for estimating release rate. Therefore, the release rates are temporally dependent (time-varying).

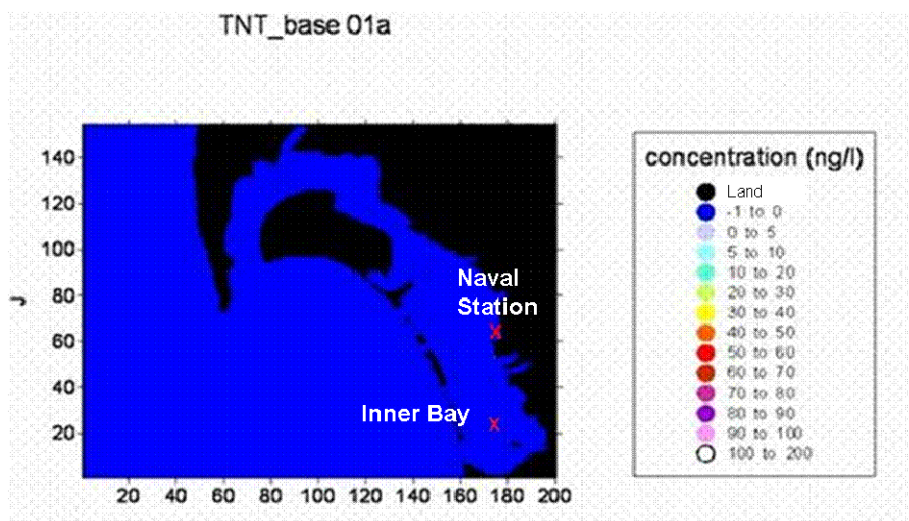


Figure 27. Location (X) of MC release from a single breached shell, inner San Diego Bay and San Diego Naval Station, respectively (no loading scenario).

3.6.3 WASP7 Model

The second model applied for this analysis is the toxic module (TOXI4) of the U.S. EPA Water Analysis Simulation Program Version 7 (WASP7) (Wool *et al.*, 2001; Ambrose *et al.*, 1993). WASP7 is a dynamic compartment (“box”) modeling program for aquatic systems. The time-varying processes of advection, dispersion, point and nonpoint mass loading, and boundary exchange are represented in the basic program. For each box, WASP7 calculates the mass of contaminants exiting the box by physical transport and chemical or biological transformation, or accumulation therein.

The WASP models have been applied previously to address fate and transport in estuaries, including the eutrophication in Tampa Bay (Wang, Martin, Wool, and Morrison, 1999) and a pesticide spill in the Sacramento River (Wang *et al.*, 1997). Model accuracy and stability were demonstrated in these studies and we have selected this model for simulating the fate and transport of MCs leached from a breached shell in San Diego Bay.

The WASP7 model domain includes both the water column and sediment bed. It is assumed that the water column (vertically from water surface to the sediment-water interface) is fully mixed. Below the water column is a vertically stratified sediment column. The sediment is well-mixed within each layer, but segmented vertically into a well-mixed active surface layer and a deep sediment layer. The deep sediment is further segmented into contaminated and clean sediment regions. Transport pathways incorporated into the WASP7 model include volatilization, burial, resuspension, settling, advection, in addition to pore-water diffusion, sorption, and decay. Spatial variations are described and evaluated by the use of multiple boxes in the horizontal plane.

Pollutants in the water column can be transferred to the atmosphere by volatilization and to the sediment layer by settling. Concurrently, pollutants in bottom sediments can be released into the water column by resuspension of particles, mixing by benthic organisms, and diffusion from the sediment pore water.

The parameters described above for use with WASP7 are listed in Table 9.

Table 9. Model parameters for WASP7 (San Diego Bay and Elizabeth River).

Water Column	Values	
	San Diego Bay	Elizabeth River
Porosity	0.8	0.8
Particle specific gravity	2.65	2.65
Suspended Solids Concentration	2 mg/L	15 mg/L
Weight Fraction Carbon in Solids	0.02	0.02
Settling velocity	0.5 m/hr	4.2 m/hr
Resuspension velocity	9.4E-05 m/yr	0.25 m/yr
Molecular diffusivity	1.0.E-09 m ² /s	1.0.E-09 m ² /s
Henry's Constant	0.00013700 atm·m ³ /gmole	0.00013700 atm·m ³ /gmole
Molecular weight (TNT)	227 g/mole	227 g/mole

These parameters are generated based on the best available knowledge that we have for San Diego Bay and the Elizabeth River. With these parameters, the fate and transport of MCs from a single breached shell can be simulated. Steady-state solutions were obtained from the WASP model runs.

3.6.4 WASP Model Setup

Two model scenarios for two Navy harbors were set up for this analysis. The first model scenario was for San Diego Bay, California, and the second model scenario for Elizabeth River, Virginia. San Diego Bay is an estuary in which the flows are governed by tidal forcing from the Pacific Ocean. The bay receives very little freshwater inflow throughout the year except during the storm seasons of the wet years. Transport and flushing of the bay are primarily driven by tides. In comparison, the Elizabeth River watershed is a riverine sub-estuary of the Chesapeake Bay estuarine systems. The watershed is a complex system of branches and small tributaries that also contains a deep-water harbor used by the U.S. Navy and many maritime industries. The watershed is approximately 600 km², with ambient water and sediment quality influences from the highly industrialized commercial and military activities and densely populated urban areas of the metropolitan Hampton Roads Region. The river flow is affected by the tidal motion from the river mouth and the riverine flows entering from upstream of five major watersheds. As a result, transport and flushing of the river behave differently than those for San Diego Bay.

San Diego Bay, California

An eight-box model grid for San Diego Bay was generated, as shown Figure 28. Information on the grid size is included in Table 10 and Table 11. Flows and properties in each of the boxes are assumed to be homogeneous (fully mixed). Transport in the water column includes net advective flow from the inner bay (Box #1) toward the mouth of the bay (Box #8), and hydrodynamic dispersion occurs between boxes. Total suspended solids (TSS) concentration in the water column is obtained based on the field data. The settling velocity of TSS is used to describe sedimentation processes (TSS and particulate MCs). The resuspension velocity is calculated based on the assigned settling velocity so that the sediment bed remains at steady-state condition, *i.e.*, there is no gain or loss of sediment mass in the bed. The hydrodynamic dispersion coefficients between adjacent boxes, obtained by calibration in a previous study (Wang, Chadwick, Johnson, and Grovhoug, 2006), are assigned to the two model grids.

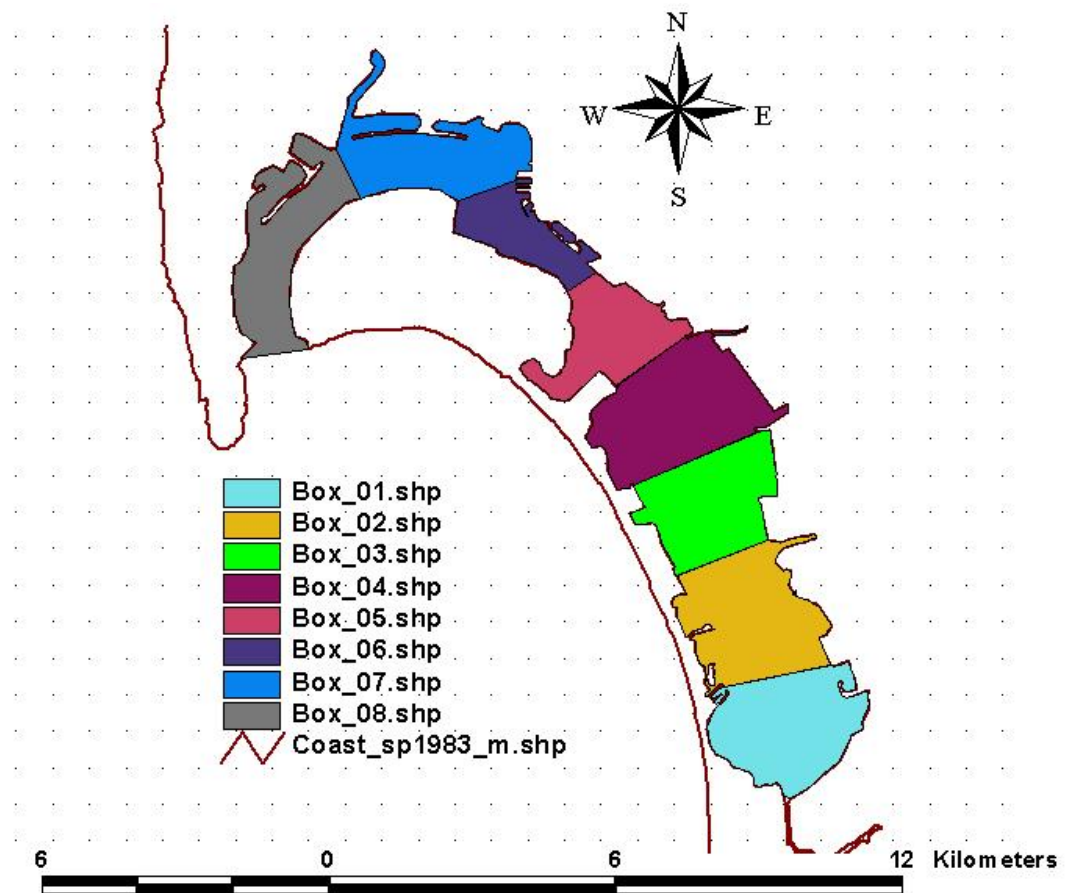


Figure 28. Model grid with eight boxes for WASP7 (box numbering starts from the inner bay and ends at the bay mouth).

Table 10. Grid sizes for the eight-box model grid for San Diego Bay.

No.	Surface Area (m ²)	Perimeter (m)	Characteristic Length (km)	Water Depth (m)	Water Volume (m ³)
1	6,248,273.28	12,733.26	2.340	2.0	12,496,546.56
2	6,708,257.83	15,821.94	2.716	3.3	22,137,250.84
3	5,611,943.57	10,562.35	2.154	4.8	26,937,329.14
4	7,438,031.79	13,831.00	2.213	6.0	44,628,190.74
5	4,298,172.22	11,254.83	2.200	6.6	28,367,936.65
6	3,119,004.66	12,988.63	2.873	9.2	28,694,842.87
7	5,658,497.40	18,893.49	3.067	9.8	55,453,274.52
8	5,778,423.78	18,386.98	4.408	10.2	58,939,922.56

Table 11. Simulation matrix for San Diego Bay using WASP7.

8-box San Diego Bay	Hydrodynamic Dispersion	Settling/Resuspension Velocities	Mineralization
Case 1a	Yes	No	No
Case 1b	Yes	No	Yes
Case 2a	Yes	Yes	No
Case 2b	Yes	Yes	Yes

To understand crucial processes governing the fate and transport of TNT in San Diego Bay, we have selected the following four cases, each with different combinations of model parameters:

Case 1a simulates the transport of TNT in San Diego Bay driven only by the hydrodynamic dispersion. This scenario is similar to the scenario simulated by TRIM2D with no mineralization. The only difference is that San Diego Bay is represented by eight boxes in WASP7 and the TRIM2D model uses much finer grid resolutions. With the different resolutions, WASP7 model results for Case 1a are compared with those from TRIM2D; both can be considered as the conservative estimates of TNT in water column for this analysis.

Case 1b is the same as **Case 1a**, but with mineralization (same as the rate used in TRIM2D). Results are also compared with the results from the corresponding TRIM2D run.

Case 2a simulates both transport in water column and exchange of particulate TNT across the water/sediment interface via settling and resuspension. Settling velocity of 0.5 m/hour is assumed, which, according to the Stoke's Law, corresponds to particles with size ~20 µm. TSS concentration of 2 mg/L is assumed in the model (derived from San Diego Bay field data). Under the assumption that sediment mass is balanced (no net sediment erosion or accumulation), a resuspension velocity necessary to satisfy this condition is calculated and assigned to the model.

Case 2b is the same as **Case 2a**, but with mineralization.

For Cases 2a, 2b (and later in the 4a and 4b cases for the Elizabeth River), a partitioning coefficient between the particulate and aqueous phases of TNT is needed. A literature search reveals little or no direct measurements of partitioning coefficient of TNT in marine water/sediment. Although in theory, partitioning coefficient of TNT can be calculated from K_{OW} and TOC, there are studies in measuring partitioning coefficient values for marine water. During measurements of TNT partitioning coefficients in laboratory settings by Pennington (personal communication), a steady-state distribution between sediment and overlying water could never be reached. "TNT and its

degradation products continued to decline until the end of the test. This can be attributed to continuing removal of the compound from the water by degradation, transformation, or covalent bonding to sediment components such as organic carbon” (Brannon *et al.*, 2005). Mostly likely, these processes, observed by Pennington as mentioned above, are not reversible, contrary to partitioning that is used in the model as a reversible process.

In other efforts, measured partitioning coefficients of TNT in soils with various contents of moisture and total organic carbon were reported (Brannon and Pennington, 2002). Gerald and Dortch (personal communication) summarized and examined the data reported by Brannon and Pennington (2002) and confirmed that the partitioning coefficient for TNT, RDX, and HMX are dependent on a number of soil and chemistry parameters, including percentage of clay, cation exchange capacity (CEC), and TOC. Ranges of values and mean of the partitioning coefficients associated with these parameters are shown in Table 12. Measured mean TNT partitioning coefficients (for soil) were low, in the range of ~0.88 to 5.5 L/Kg. Since these are the only reported values that are conformal to partitioning, we used these values, 0.9 and 5.0 L/Kg, in our modeling study, despite the fact that they are for soil.

Table 12. Ranges and mean values of soil partitioning coefficients for TNT and RDX (Brannon and Pennington, 2002).

% Clay	CEC, milliequivalents (g ¹)	TOC (%)	Range of partitioning coefficient values L/Kg	Mean Partitioning Coefficient Values	Number of Observations
TNT					
0-20	0-10	0-1	1.04-3.64	0.88	11
20-50	11-30	1-3	2.3-6.16	3.39	14
> 50	> 30	> 3	2.23-11	5.54	12
RDX					
0-20	0-10	0-1	0.07-1.57	0.53	11
20-50	11-30	1-3	0.06-1.65	0.85	13
> 50	> 30	> 3	0.31-8.4	2.31	15

Elizabeth River, Virginia

A box model for the Elizabeth River was generated, as shown in Figure 29. The box model is composed of 26 boxes for the water column and the sediment layer, boxes 1–13 and boxes 14–26, respectively. Box #1 is located at the upstream boundary and Box #13 at the downstream boundary for the Elizabeth River. Dimensions of the model boxes are shown in Table 13. Flows and properties in each of the boxes are assumed to be homogeneous (fully mixed). Transport in the water column includes net advective flow from the upstream segment (Box #1) toward the mouth of the river (Box #13), and hydrodynamic dispersion between boxes (Figure 30). Total suspended solids (TSS) concentration in the water column is obtained based on field data (Wang *et al.*, 2007). Settling of particulate MCs are described by the settling velocity of TSS. The resuspension velocity is calculated based on the assigned settling velocity so that the sediment bed deposition rate of 1 cm/year is achieved, which is obtained from sediment coring data (Wang *et al.*, 2007). The hydrodynamic dispersion coefficients between adjacent boxes, obtained by calibration in a previous study (Wang *et al.*, 2006) are assigned to the two model grids.

The salinity gradient results from the balance of advection and dispersion in the river. The freshwater riverine inflows from the watersheds are obtained from measured data as shown in Table 14 and Figure 31. To estimate the dispersion coefficients, we used the finite-difference model of salinity by Thomann and Mueller (1987) to estimate the dispersion coefficients for the Elizabeth River (Figure 32).

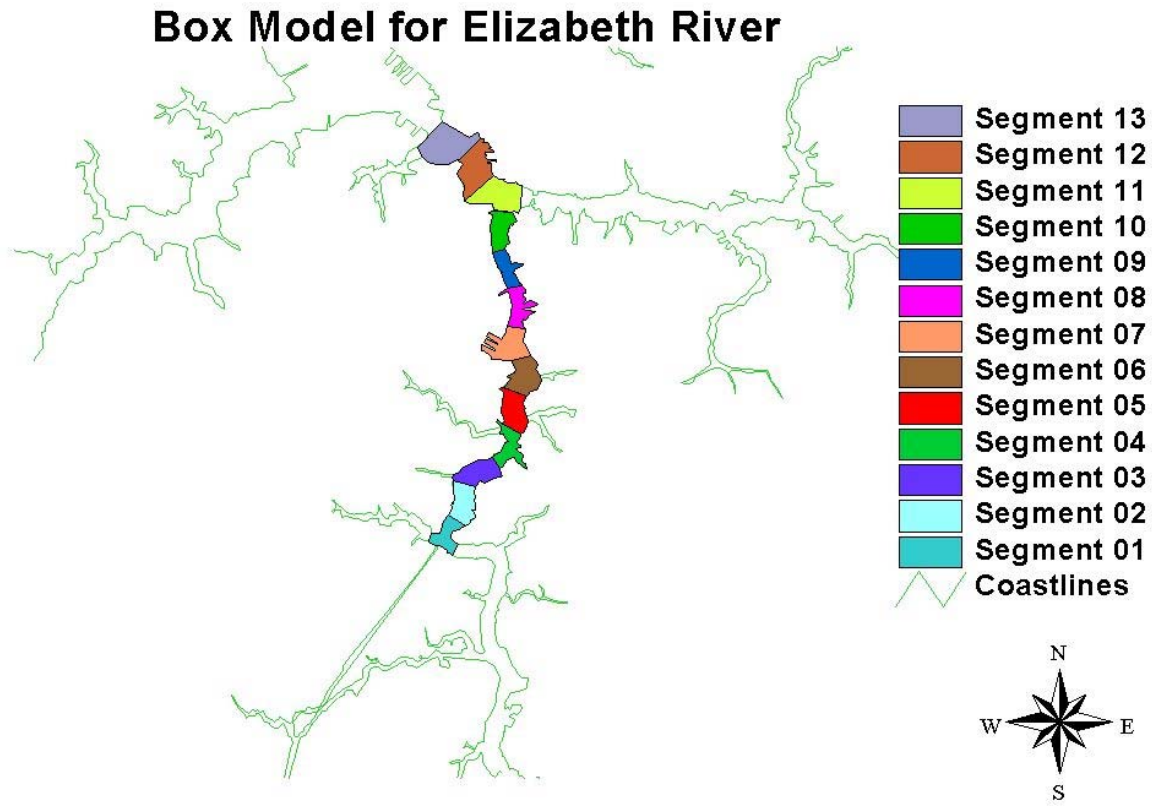


Figure 29. Box model for Elizabeth River.

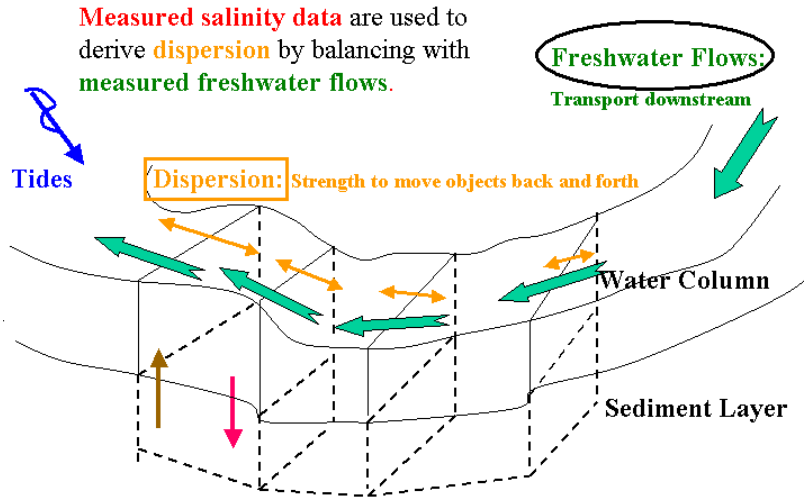


Figure 30. Conceptual box model for fate and transport of TNT in Elizabeth River.

Table 13. Grid sizes for the 13-box model grid for Elizabeth River.

Segment No.	Surface Area (m ²)	Depth (m)	Volume (m ³)	Interaction Area (m ²)
1	261,214	6.7	1,750,410	2,020
2	352,011	5.0	1,759,852	2,768
3	359,596	5.8	2,081,851	2,733
4	297,811	7.3	2,162,238	2,392
5	366,058	8.7	3,198,533	3,359
6	393,763	6.8	2,686,806	4,465
7	444,106	10.5	4,658,982	3,364
8	300,423	8.0	2,416,018	3,801
9	248,628	10.0	2,497,280	3,201
10	309,713	7.5	2,321,518	2,898
11	529,690	5.6	2,992,211	3,892
12	554,277	6.8	3,759,952	3,497
13	654,112	6.4	4,188,029	5,011

Table 14. Discharge data for Elizabeth River.

Watersheds	Discharge (cms)
Lafayette River	0.53
Western Branch	0.94
Eastern Branch	0.88
Deep Creek	2.60
Southern Branch	1.66

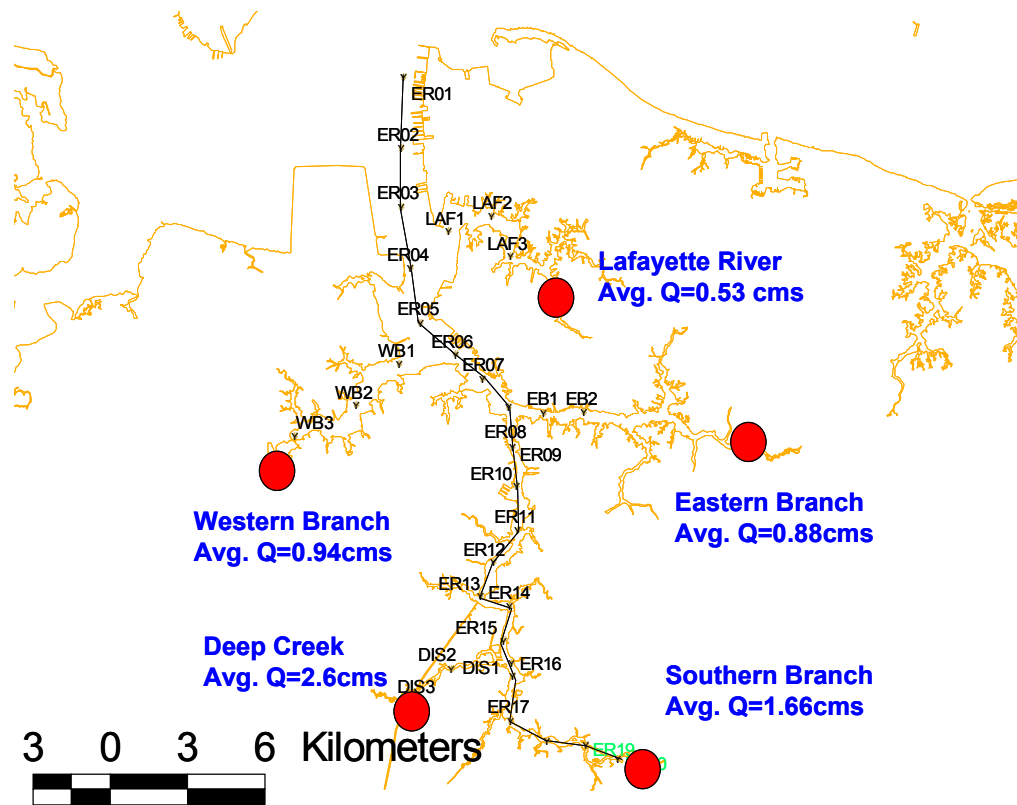


Figure 31. Riverine freshwater inflows from five major river branches of the Elizabeth River watershed.

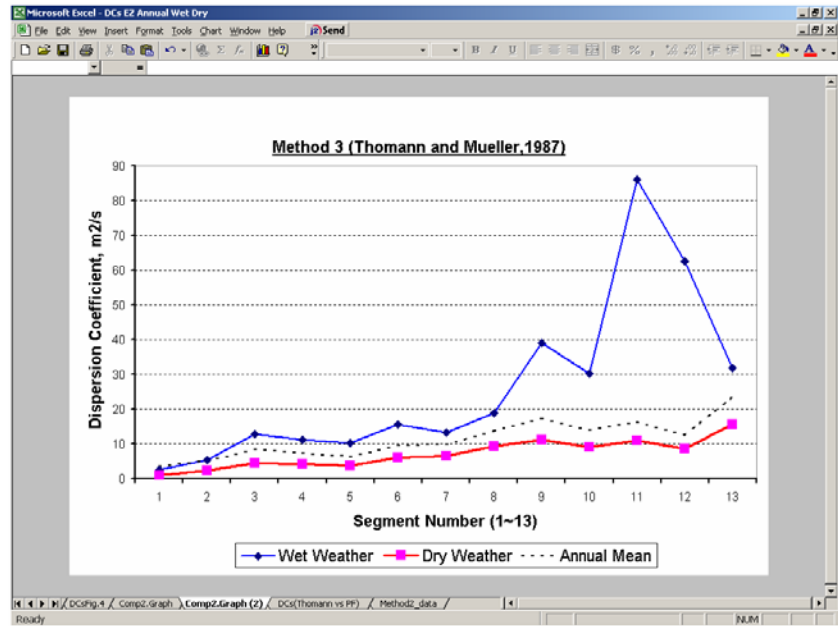


Figure 32. Dispersion coefficients for Elizabeth River.

Table 15 describes the four scenarios for the Elizabeth River study.

Table 15. Simulation matrix for Elizabeth River using WASP 7.

13-box Elizabeth River	Hydrodynamic Dispersion	Settling/Resuspension Velocities	Mineralization
Case 3a	Yes	No	No
Case 3b	Yes	No	Yes
Case 4a	Yes	Yes	No
Case 4b	Yes	Yes	Yes

Case 3a simulates the transport of TNT in Elizabeth River with the 8-kg/year TNT released in Box #2, #6, and #12, respectively. The goal of evaluating the behavior at these three different release locations is to understand the transport/dispersion patterns for TNT in the river.

Case 3b is similar to Case 3a, but with mineralization.

Case 4a is similar to Case 2a and simulates both transport in water column and exchange of particulate TNT across the water/sediment interface for Elizabeth River.

Case 4b is the same as Case 2a, but with mineralization.

3.7 MODELING PORE-WATER ADVECTION IN SEDIMENT FLUME BOX

As part of the empirical study for evaluating MC release in sediment, experiments were conducted to measure pore-water advection flow and release rates of dye (as MC surrogate) at the University of Wisconsin-Milwaukee. Results of this empirical study were then compared with the simulations of pore-water advection. To simulate the pore-water in the sediment flume box, a simple 2-D model based on Darcy's Law was developed. Figure 33 shows the configuration of the model grid and parameterization. Three head differences between the left and right boundaries were used: 1, 2, and 3 inches.

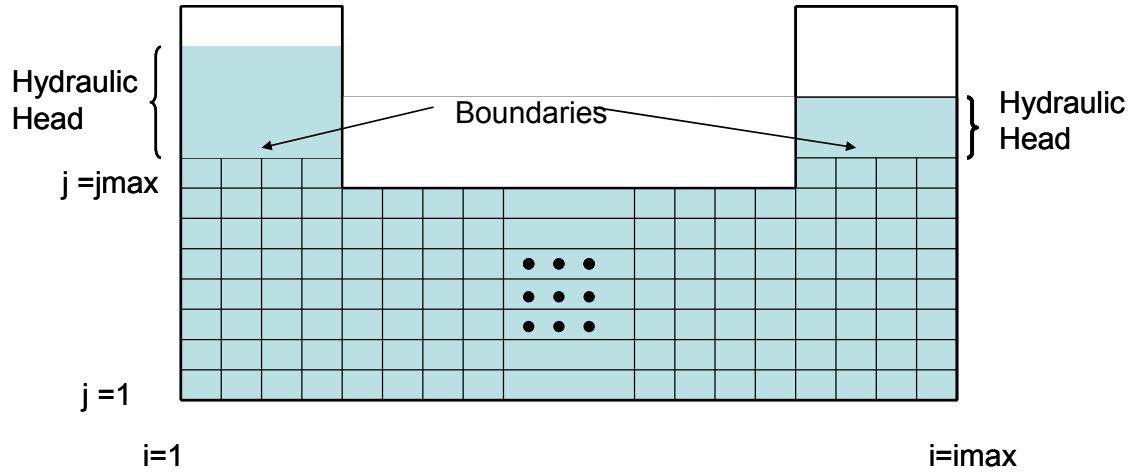


Figure 33. 2-D model for pressure induced pore-water seepage flow in sand flume box.

Following Darcy's Law,

$$Q = -kA \frac{dh}{ds}, \quad (32)$$

where Q is the Darcy velocity (L/sec); k is the conductivity (L/sec), which is a function of the media (*e.g.*, silt, sand, etc); A is the cross section of the flow, which is perpendicular to the flow direction s , and dh/ds is the pressure gradient in the s direction. Eq. (32) is a well-known fundamental governing equation for groundwater flow and transport, which is a basis for nearly all groundwater models (MODFLOW, SUTRA, etc.) (Bear, 1979 and Freeze and Cherry, 1979). While these complex models can accommodate complex systems, the fundamental principal depicted by Eq. (32) is universal.

Similarly, we have developed a simple model, based on Eq. (32), to simulate pore-water advection for the same scenarios that were evaluated by the empirical study. For those experiments, it is assumed that the pore-water flow was homogeneous, isotropic (no directionality for conductivity), and saturated flows, for which the continuity equation is

$$\nabla \cdot (\rho \vec{V}) = 0, \quad (33)$$

where the gradient vector operator (∇) and the flow velocity (V) can be expressed in the (x, y, z) coordinate system as

$$\nabla = \frac{\partial}{\partial x} \vec{i} + \frac{\partial}{\partial y} \vec{j} + \frac{\partial}{\partial z} \vec{k} \quad (34)$$

and

$$\vec{V} = V_x \vec{i} + V_y \vec{j} + V_z \vec{k}. \quad (35)$$

Substituting Eqs. (32) into (33) ($Q = V$), the equation governing the homogeneous, isotropic saturated flow for the empirical sand flume box is

$$\nabla^2 h(x, y) = \frac{\partial^2 h}{\partial x^2} + \frac{\partial^2 h}{\partial y^2} = 0. \quad (36)$$

Assuming a rectangular grid is used with the size $dx = dy = 3$ inches, 60 cells, each with the I-index, correspond to the x-direction, and 12 cells, each with the J-index, correspond to the y-direction. The model calculates the head pressure, $h(I, J)$, induced by the pressure head difference imposed at the two boundaries (Figure 34). The indices, (I, J) , represent the coordinates, (x, y) with equal grid sizes, $dx = dy = 3$, and $x = I \cdot dx$, $y = J \cdot dy$, respectively. In order to solve Eq. (36) at all the nodal points (I, J) , the head at the node (I, J) can be categorized into the following three types: interior nodes, boundary nodes, and corner nodes (Figure 34).

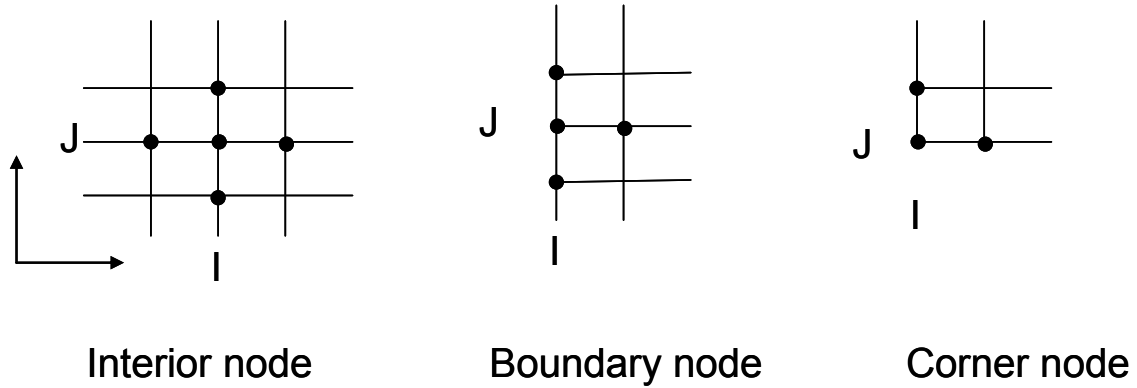


Figure 34. Interior, boundary, and corner nodes of the numerical mesh for solution of Eq. (36).

Boundary and corner nodes in the reversed direction can be developed following the same rules as shown in the following equations.

To set up the model following Eq. (36), the equations are applied for the nodes in the interior, at the boundaries, and at the corners of the domain:

$$\text{Interior nodes: } h(I, J) = \frac{1}{4} (h(I-1, J) + h(I+1, J) + h(I, J-1) + h(I, J+1))$$

$$\text{Boundary nodes: } h(I, J) = \frac{1}{4} (h(I, J-1) + h(I, J+1) + 2h(I+1, J))$$

$$\text{Corner nodes: } h(I, J) = \frac{1}{4} (h(I, J+1) + h(I+1, J))$$

The model calculates the pressure head, $h(I, J)$, at each of the nodes. Figure 35 (top panel) shows the pressure head and the corresponding pressure gradient contours for the 1-inch head difference (Δh) between the boundaries. The other two panels in the figure show the corresponding variables for the other two cases, 2-inch and 3-inch head difference, respectively. Darcy's velocity can be readily obtained as the product of the head gradients and the conductivity of the sand. Generally, pore-water advection is proportional to the net head difference between the two boundaries. Flows (arrows) are

perpendicular to the head contours (solid line with numbers) flowing from high head (left) to low head (right). In the middle section of the box, pore-water flows are relatively uniform in the water column.

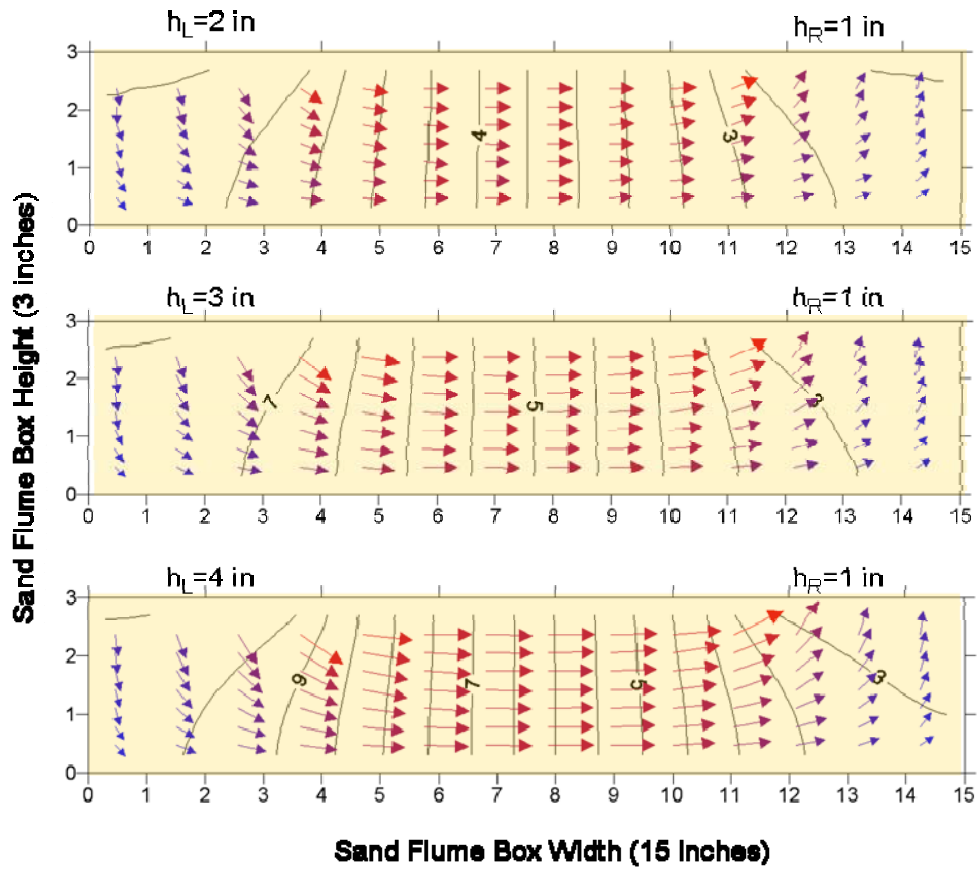


Figure 35. Simulated pressure gradients over the three scenarios ($\Delta h = 1, 2,$ and 3 inches, for the top, middle, and bottom figures, respectively).

4. RESULTS AND DISCUSSION

4.1 MODEL VALIDATION

4.1.2 Validation Case I: Dependence on Current Speed, (U), and Radial Direction, (r)

In the first validation case, the radius of the breach hole is $b = 5$ mm. The inside cavity is a semi-sphere with radius $R = 0.1$ m. Upstream current speed varies from 1 to 0.5 m/s. The Reynolds number based on the hole size and the mean current speed varies from 5 to 2,500.

The flow configuration results in a complicated circulation pattern inside the shell as seen in Figure 36. Circulation of fluid causes advection of MC solution, and the resulting effects can be modeled as a diffusion process with a circulation enhanced diffusivity D_A , and solution of Eqs. (10a) and (10b) can still apply.

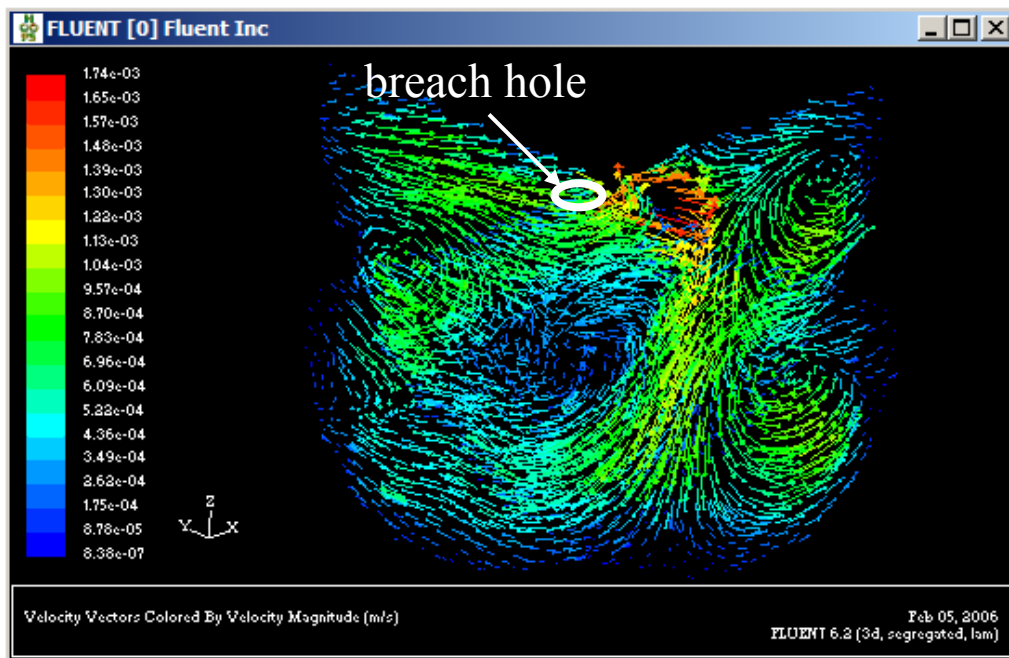


Figure 36. Current-induced inner circulation in the casing. $b = 5$ mm and $U = 6$ cm/s.

The circulation enhanced diffusivity, D_A , has a dimension of [Velocity \times Length], which in general, should be a function of r ; D_A varies with distance r inside the cavity. The velocity scale is modeled as

$$u_A(r) = \frac{\int_{r'=r} \sqrt{[u(r')]^2 + [v(r')]^2 + [w(r')]^2} dA}{2\pi r^2}, \quad (37)$$

where u , v , and w are the disturbed velocity components in the x - y - z coordinates inside the cavity at the radius r , over which the surface integral is performed.

The value u_A is the averaged velocity on a spherical surface with radius r . D_A is modeled as

$$D_A = \beta u_A r, \quad (38)$$

where β is a model parameter.

Based on FLUENT simulation results, D_A/β as a function of r is calculated for different current speed, as shown in Figure 37. Generally, u_A decreases with r , but $u_A r$ is only weakly dependent on r , except near the breach hole and the solid-liquid interface.

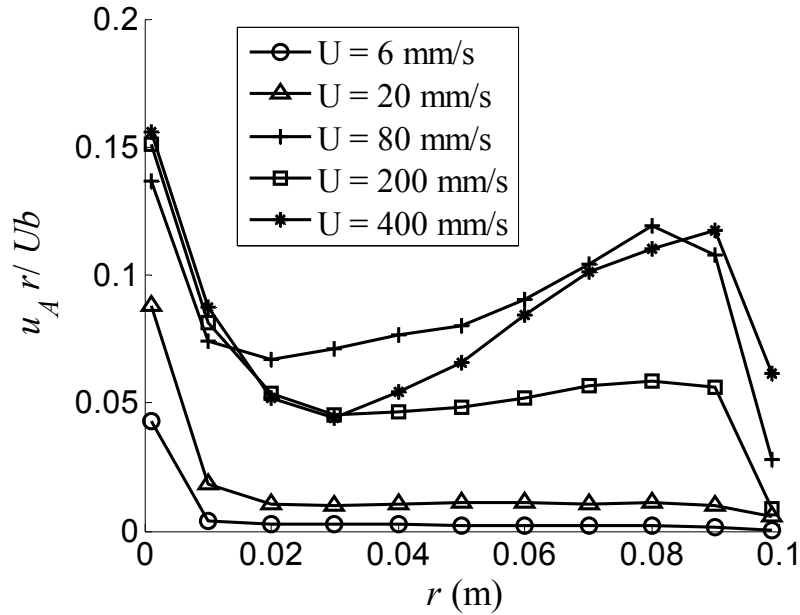


Figure 37. Distribution of $u_A r / Ub$ as a function of r for different current speed.

As a first-order approximation, we assume D_A is homogenous inside the breach hole and we take the average of D_A / β calculated at different r (except for $r = b$ and $r = R$) as the effective advection induced diffusivity, as defined in Eq. (38), and plot it with respect to current speed U times the hole radius b , as shown in Figure 38.

Again, as a first-order approximation, we assume there is a linear relationship between D_A / β and Ub . By linearly fitting with the simulation result (Figure 39), we can propose a model for D_A :

$$\frac{D_A}{\beta} = 0.012 Ub. \quad (39)$$

It can be shown that D_A is much greater than the molecular diffusivity D_M except for very small current speed. According to this argument, Eq. (11) for the MC flux rate is

$$F \approx \frac{2\pi \times 0.012 \beta Ub C_s}{\frac{2 \times 0.012 \beta Ub}{\alpha Ub^2} + \frac{1}{b}} \approx \theta U (\pi b^2) C_s, \quad (40)$$

where $\theta = \frac{0.024\alpha\beta}{0.024\beta + \alpha}$, *i.e.*, the flux is linearly proportional to the current speed, the saturated MC concentration, and the radius of the breach hole.

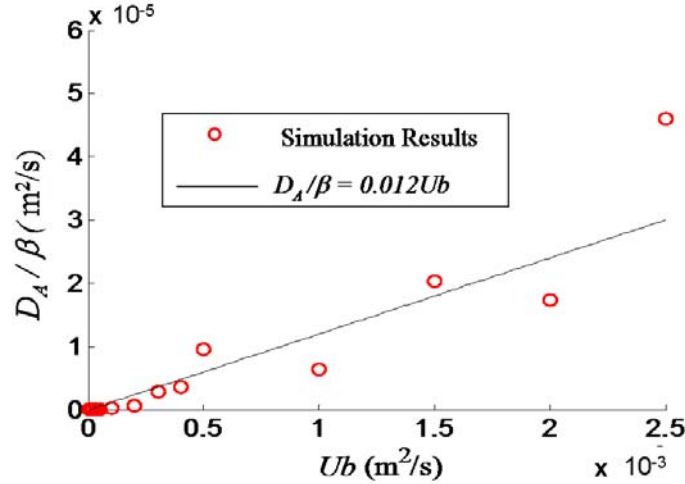


Figure 38. Modeled relationship between the effective diffusivity D_A , and the current speed U .

The above model is validated with the simulation results, as shown in Figure 39. The linear relation observed above fits well with simulation results and the model coefficient θ is ~ 0.023 . Note that the linear growth of F with U is only valid for large Reynolds number values. As shown in the inset plot for small U in Figure 39, the effect of molecular diffusion is on the same order of magnitude as advection, thus the linear dependency is not valid in this regime.

With the fitted parameter θ , we can substitute the modeled D_A into the equation of concentration profile Eq. (12) and compare it with simulation results. Figure 40 shows, as a function of r , both the analytical solution and simulation results for different current speeds. There are generally good agreements, especially for smaller current speed. However, for $U > 100$ mm/s (+ symbols), differences between simulation and analytical solutions become apparent. This is due, in part, to the circulation-induced diffusivity becoming increasingly inhomogeneous, which makes our analytical solution invalid for this current regime.

4.1.3 Validation Case II: Dependence on Hole Size, (b)

As in Validation Case I, the cavity inside the shell casing is still a semi-sphere with radius $R = 0.1$ m and the current speed is a constant with $U = 0.1$ m/s. The radius of breach hole varies from $b = 5$ to 50 mm.

If we first assume our previous analysis is still valid for this case, then we would have

$$\frac{F}{C_s} \approx 0.023U(\pi b^2) = 0.007b^2, \quad (41)$$

where F would be a quadratic function of the hole radius b (or alternatively a linear function of breach area A). Using these two validation cases, the MC release rate is approximated as

$$F \approx 0.023UAC_s, \quad (42)$$

similar to the analysis of Eq. (12) in Figure 39.

The above model is compared with the simulation results in Figure 41. It agrees well with numerical experiment results for $b < 25$ mm. However, it does over-estimate the flux for larger holes. This is not a surprise since when b grows larger, the inner circulation becomes more complex and the assumption of a small hole size starts to be violated for the analytical release rate function.

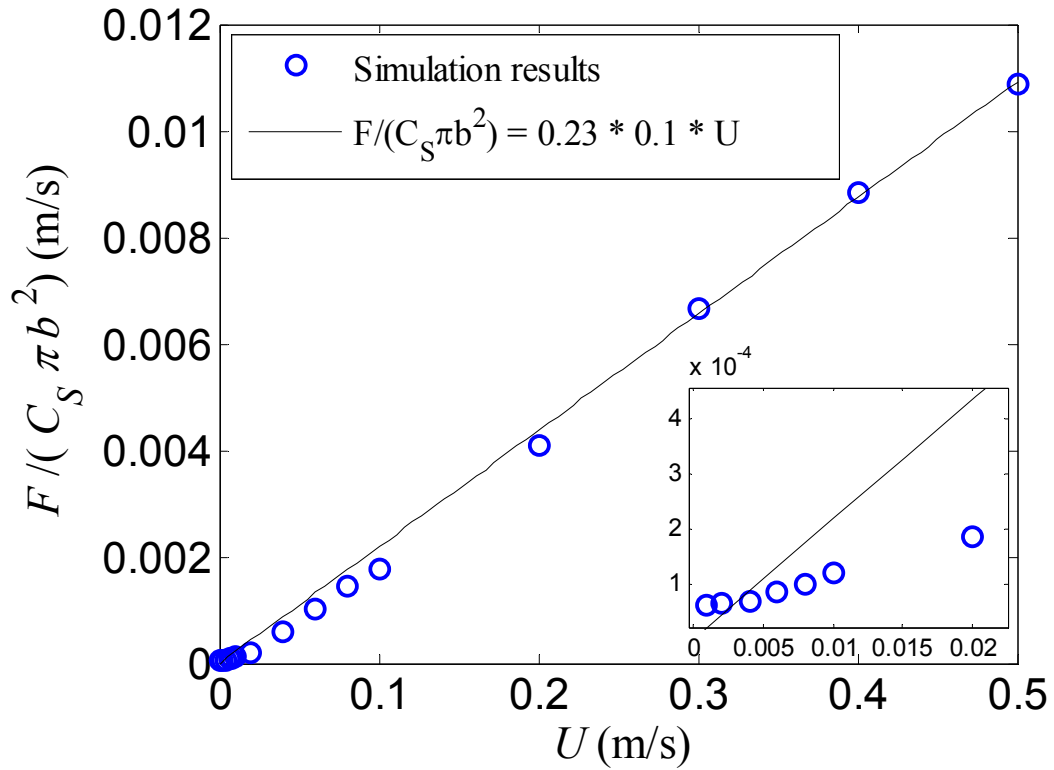


Figure 39. Variation of MC flux rate with respect to current speed.

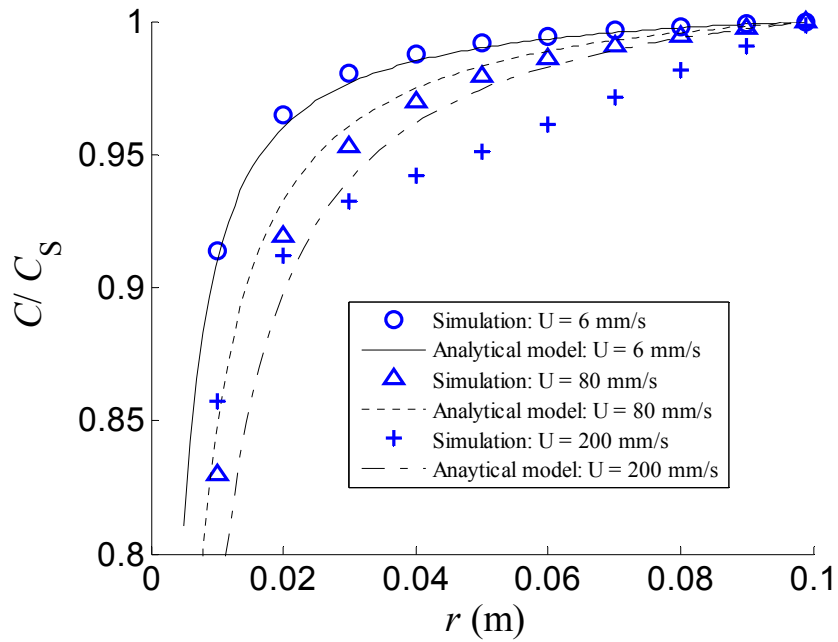


Figure 40. Radial distribution of concentration in the casing. Simulation results compared with analytical solution (Eq. (9)).

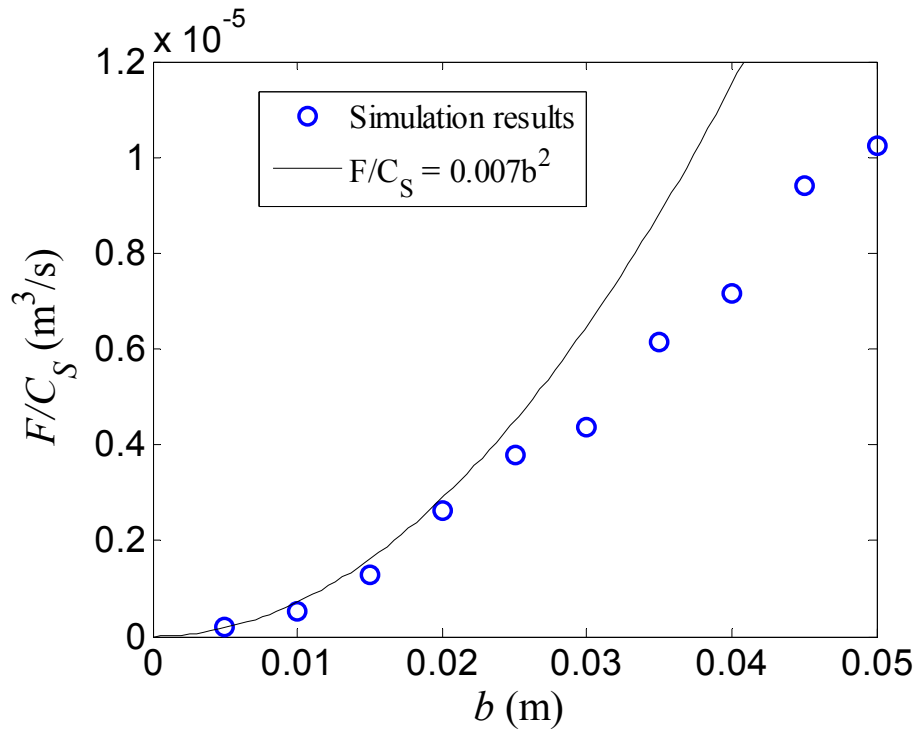


Figure 41. Variation of MC flux rate F , as a function of hole radius b .

4.2 EFFECTS OF SHELL THICKNESS

In our previous analysis, the munition wall or shell thickness (hereafter denoted as h) has been ignored. Shell thickness is generally smaller compared to the inner cavity radius R , thus its effects on the overall flux rate can be considered secondary, *i.e.*, it may result in a slightly different coefficient β in the boundary condition of our analytical model (*i.e.*, Eq. (38)), but the general equation of inner scalar transport should not be affected by nominal shell thickness.

Due to the limitation of grid size, details of circulation patterns smaller than h are not easily resolved by simulation. We will, however, present the empirical relation between the release rate and the shell thickness. Three breach radius are selected for simulation, $b = 2.5, 5,$ and 10 mm, respectively. The shell thickness varies from 4 to 24 mm and the current velocity is allowed to change from 4 to 45 cm/s. Figure 42 shows the release rate function F vs. the ambient current U for various shell thicknesses. In most cases, a linear increase of release rate (flux) with the mean current U can be observed. This agrees with the analytical solution Eq. (10a). However, the proportionality ($\theta\lambda$) differs from case to case. For comparison, the empirical solution for validation case I, Eq. (40), is also shown in this figure.

The release rate function (Eq. (42)) is shown normalized and plotted vs. shell thickness in Figure 43. The normalized release rate fluctuates when h and b are of the same order of magnitude. When $h \gg b$, the normalized F seems to be independent of h and becomes a constant. This constant varies between 0.015 and ~ 0.035 , compared to 0.023 demonstrated in the previous validation case. Therefore, future efforts will select an appropriate value of this constant based on the $h:b$ ratio that lies within the range of 0.015 to ~ 0.035 .

4.3 RELEASE TIME

The general analytical release rate function (Eq. (10a)), which has now been validated by the FLUENT model, can be used to predict the release rates of MC, under various hydrodynamic and shell integrity conditions. For a single shell with known MC mass, the predicted release rates can be further used to estimate time to deplete all MC in the shell under these conditions. Here we use Eq. (10a) for the calculations of release time for TNT, RDX, and HMX under various hydrodynamic and shell integrity conditions.

In the analytical release rate function, the MC-dependent variables include the saturation concentrations (C_S) and the dissolution speed (μ), obtained by dividing the dissolution rate by the saturation concentration. These MC-dependent chemical data are listed in Table 16.

Brannon *et al.* (2005) measured dissolution rate constants of TNT, RDX, and HMX in saline water and compared them with the rate constants in freshwater (Table 16).

“Dissolution rates of RDX and HMX from the military formulations, Composition B and Octol, did not differ significantly under freshwater and saline conditions (see Figure 44). The rate of dissolution of TNT from the solid in saline water was slower than in freshwater. However, freshwater dissolution rate values for pure TNT would conservatively estimate TNT saline water dissolution rates. The rate of dissolution of TNT at salinities of 10 and 30 ppt was the same as the rate at 20 ppt. Dissolution rates for the explosives in both fresh and saline water decreased in the order TNT>RDX>HMX, which is consistent with trends observed previously in fresh water...” Brannon *et al.* (2005)

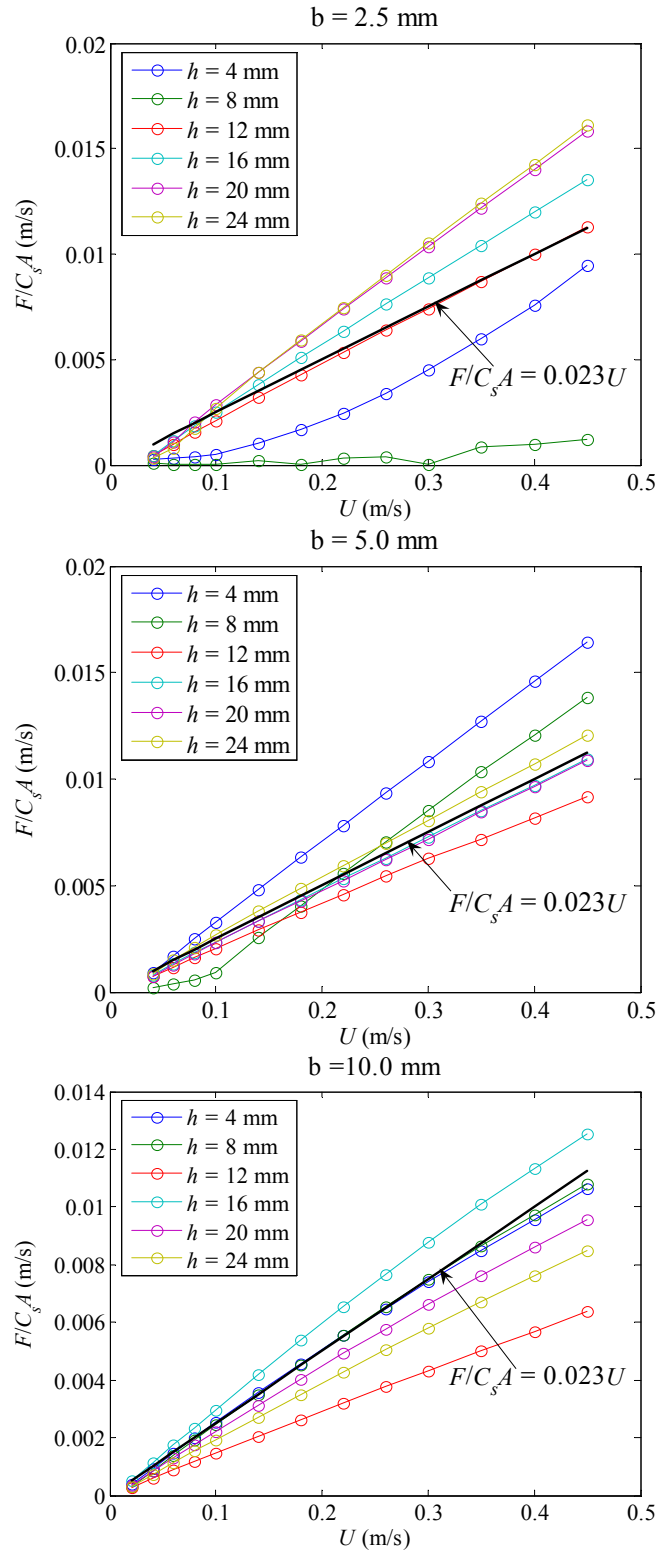


Figure 42. Release rate vs. current speed for selected shell thickness, (h), and breach hole radii, (b).

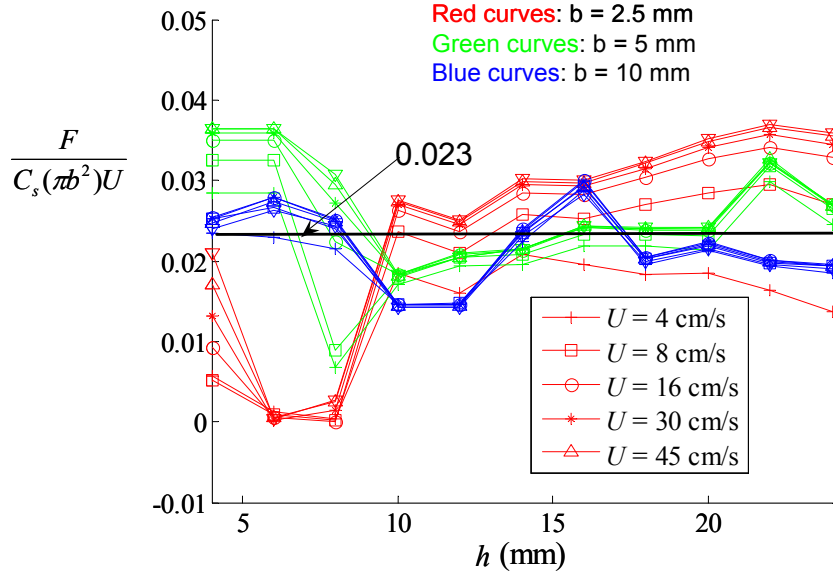


Figure 43. Effects of shell thickness on the normalized release rate.

Table 16. Saturation concentrations (C_s), dissolution rates, and dissolution speed (μ) for TNT, RDX, and HMX in freshwater.

MCs	Saturation Concentration (C_s) (mg/L)	Dissolution Rate ($\mu\text{g}/\text{cm}^2/\text{s}$)	Dissolution Speed (μ) (cm/s) (Dissolution Rate/Saturation Concentration)
TNT	88.5 (a)	0.20(d)	0.00226
RDX	38.4 (b)	0.05(d)	0.00130
HMX	6.6 (c)	0.15(d)	0.02272

(a) Ro *et al.* (1996)

(b) Spangord *et al.* (1983)

(c) McLellan, Hartley, and Brower (1988)

(d) Lynch, Brannon, and Delfino, 2002a and 2002b.

Therefore, the dissolution rates for freshwater (Table 16) are used as a conservative measure for the analysis of release rate of MCs from breached shells in the following sections.

For analysis of the following scenario, we use a typical round with the following shell dimensions: length = 24 inches, diameter = 8 inches, and MC weight = 8 kg. Shell thickness is not included for problem simplification purposes.

For different realistic combinations of the five variables in Eq. (10a), release time can vary by several orders of magnitude. For example, under an ambient current of 45 cm/s (fast flow), release time ranges from 300 years for a hole with radius of 0.05 cm to 1 year for a hole with radius of 0.95 cm, illustrating the importance of hole size. The sensitivity to ambient current is also apparent in Figure 45, where the release time varies by one order of magnitude between slow flow (5 cm/s) and fast flow (45 cm/s). For example, for a hole with a radius of 0.5 cm, it takes about 28 years to deplete the MC inside the shell under ambient current of 5 cm/s. The release time is much shorter, less than 8 years, if the ambient current increases to 45 cm/s.

Figure 46 compares the release time for TNT, RDX, and HMX under the same conditions. TNT release time is fast, followed by RDX, and HMX. Although HMX has the highest dissolution speed, its low saturation concentration (Table 16) and interactions with other parameters, including current speed, hole size, and cavity size, make the mass release from the shell the slowest of the three MCs for this scenario. For the scenario in Figure 46, saturation concentrations dictate the release time (and rate) for the three MCs.

In Figure 47, time for complete release of MC from a hypothetical shell depends on the five parameters, as discussed previously with Eq. (10a). Overall, the release function is controlled by the dissolution rate for the regime, $\mu R^2 \ll \alpha U b^2$. In this region, the release rate (and the time for complete release) depends primarily on the dissolution rate (speed), but is insensitive to the current, which is assumed to be large enough to disperse released solution faster than the dissolution rate. For the other extreme, the current controlled flow regime, $\mu R^2 \gg \alpha U b^2$, the release function (and the time for complete release) is less dependent on the dissolution rate, and depends primarily on the current speed. The dissolution speeds are 0.0016 cm/s for TNT, 0.0008 cm/s for RDX, and 0.019 cm/s for HMX, respectively, which the three up-point arrows indicate as release processes for the three MCs are between the two limiting cases.

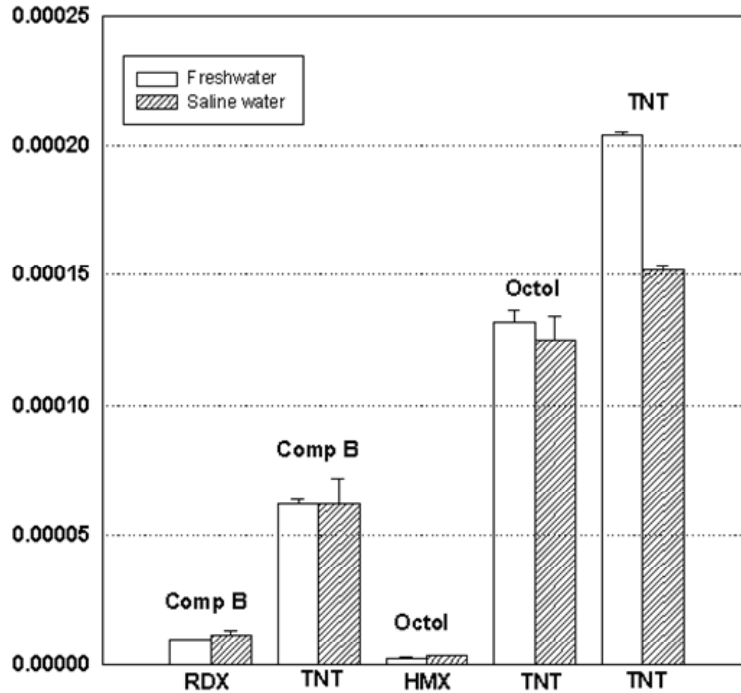


Figure 44. Measured dissolution rate constants for TNT, RDX, and HMX in freshwater and saline water (Brannon *et al.*, 2005).

In a natural coastal setting, tidal cycles dictate the flow behavior. Release rates during tidal cycles with tidal current speed ranging from 5 to 45 cm/s are shown in Figure 48 and Figure 49. For small hole size ($b = 0.1$ cm, Figure 48), release rates for TNT, RDX, and HMX vary with tidal currents over the entire current speed range. For this scenario, the current-based Reynolds Number ($U b / D$) is much smaller than the dissolution-based Reynolds Number ($\mu R / D$) and release rates are limited by current speed. For larger holes (*i.e.*, $b = 2.5$ cm, Figure 49), release rate of TNT is limited primarily by current speed when the current is low (< 15 cm/s). When the current becomes strong (speed ~ 15 to 45 cm/s), release rate of TNT is only weakly dependent on current speed; it is limited primarily by

dissolution rate. For RDX, Figure 48 and Figure 49 show that release rate is primarily limited by current speed for small hole size (*i.e.*, $b = 0.1$ cm), but it is primarily limited by dissolution rate for larger hole size (*i.e.*, $b = 2.5$ cm) over the entire range of current speed. The release rate for HMX is limited by current speed for both small and large hole sizes over the entire range of current speed.

From these analyses, it has been shown that release rates for TNT, RDX, and HMX are governed by five variables, including current speed, hole size, cavity volume, dissolution rates, and hydrodynamic diffusivity coefficient. Release rates of MC in a dynamic estuarine environment are limited by two overall conditions: current-controlled release and dissolution-controlled release. Ultimately, the release rate function can be linked with a hydrodynamic and fate/transport model to simulate the dynamic release and subsequent fate/transport of MCs in the estuarine receiving water.

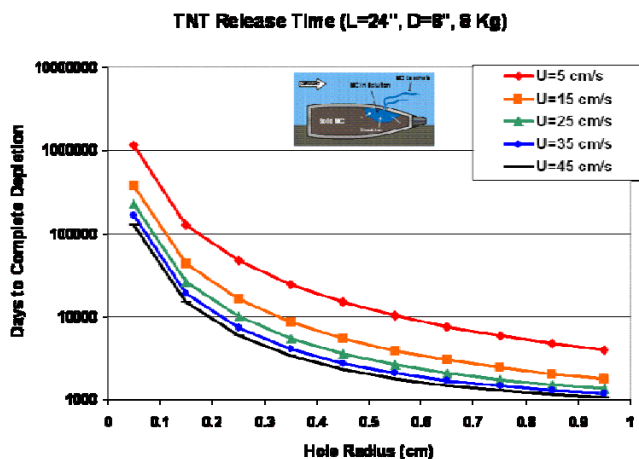


Figure 45. Days to complete release of TNT inside the shell with dimension of $L = 24$ inches, $D = 8$ inches, and MC mass = 8 kg. Release time are plotted as functions of ambient velocity (U), and hole radius (b).

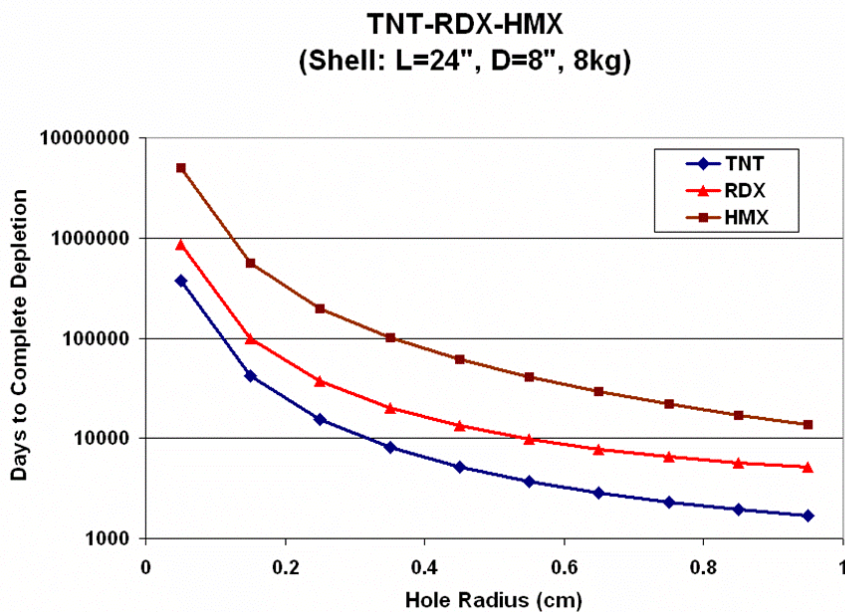


Figure 46. Release time for TNT, RDX, and HMX under the same conditions ($U = 15$ cm/s).

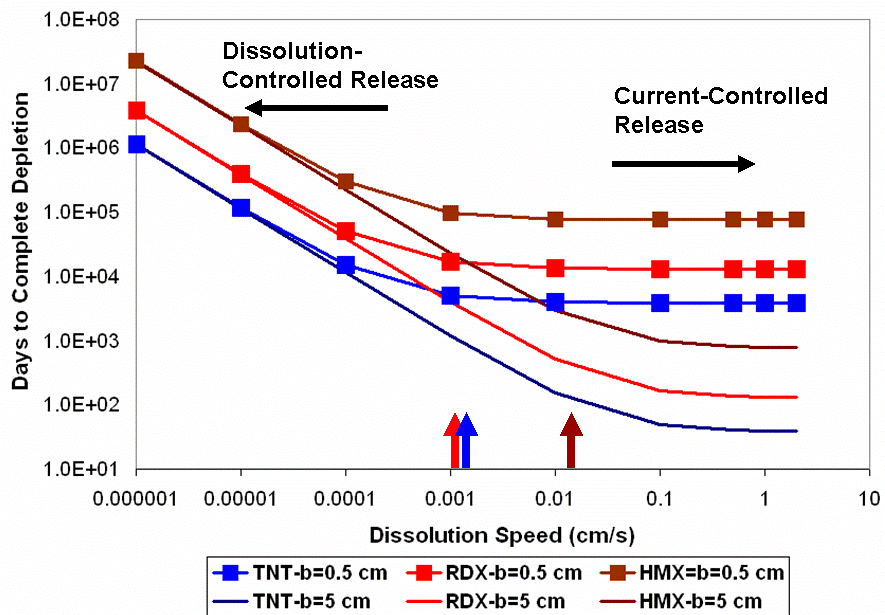


Figure 47. Days for complete release (based on Eq. (10a)) for TNT, RDX, and HMX for a release case: $U = 10$ cm/s, $R = 10$ cm. The three up-pointing arrows represent the dissolution speeds for the three compounds.

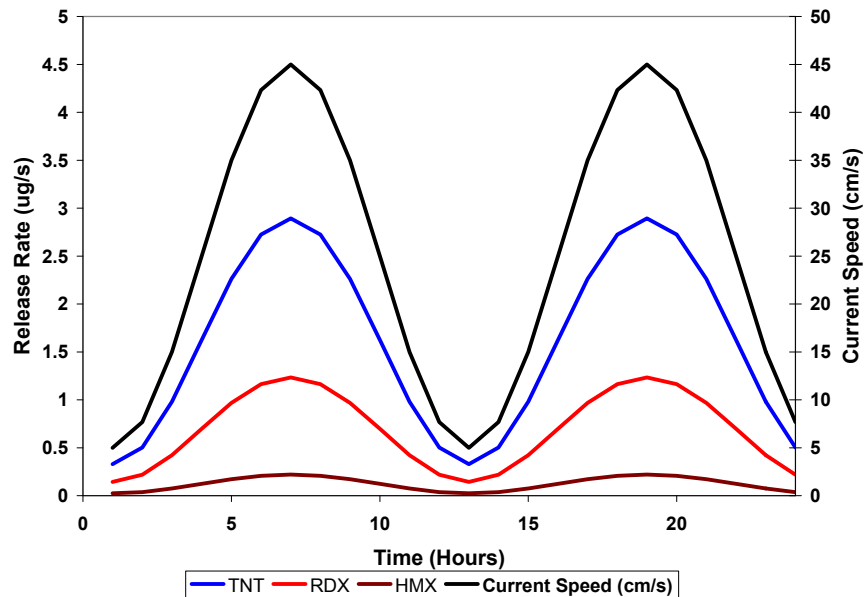


Figure 48. Release rates and current speeds over two tidal cycles (~24 hours) for TNT, RDX, and HMX ($b = 0.1$ cm, $R = 10$ cm).

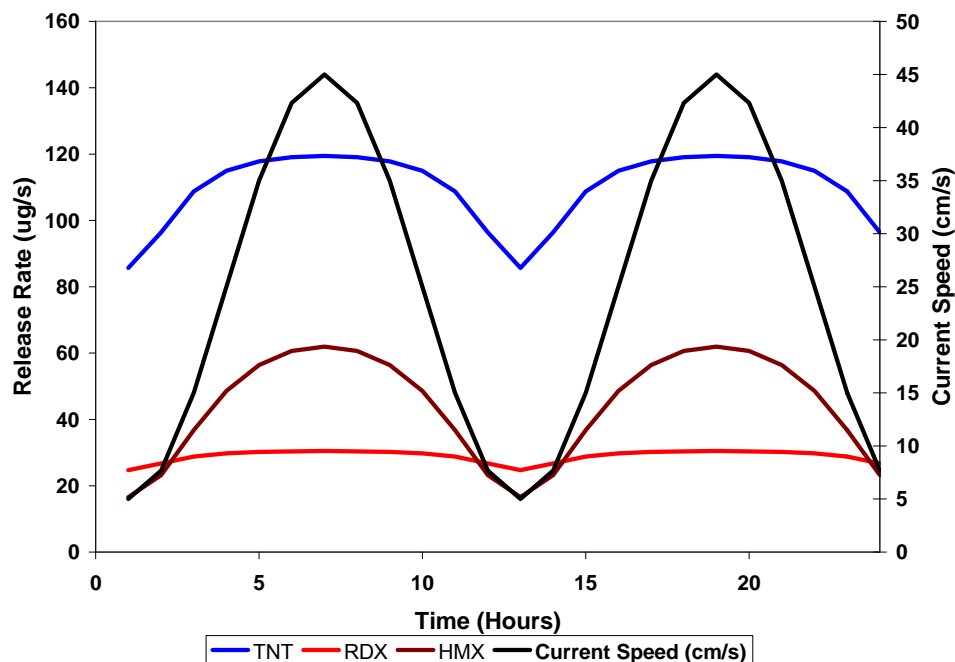


Figure 49. Release rates and current speeds over two tidal cycles (~24 hours) for TNT, RDX, and HMX (b = 2.5 cm, R = 10 cm).

4.4 MODELING FATE AND TRANSPORT OF TNT, RDX, AND HMX

4.4.1 TRIM2D Model Results

Source release rates are a function of current speed as determined by tidal fluctuations, as illustrated in Figure 50. Current speeds in the inner (San Diego) bay area are on the order of 8 cm/s and the corresponding release rates are about 300 $\mu\text{g/s}$. Generally, the release rate is controlled by current speed, below current speeds of 12 cm/s. When current speeds exceed 12 cm/s, the release rate is limited by the dissolution rate and becomes insensitive to a high current speed. Release rates under these extreme conditions (high current speed and ignoring degradation processes) were previously analyzed analytically, and they are now demonstrated here under field-based conditions.

Scenario A: Steady-state TNT concentrations in water from a single shell source release simulated under various tidal stages without any degradation are shown in Figure 51 and Figure 52. Generally, steady-state concentrations decrease from the source to the mouth of the bay, resulting from hydrodynamic transport and diffusivity. Under steady-state conditions, transport of TNT released from the breached shell gradually achieves equilibrium with the hydrodynamic flushing of the bay water, which is driven by ocean tides mixed with diurnal and semi-diurnal tidal cycles. The simulated steady-state TNT concentrations range from ~30 to 50 ng/L in the inner bay to 10 to 30 ng/L in the mid-bay areas and to about 1 to 2 ng/L near the bay mouth.

Results shown in Figure 52 and Figure 53 are independent of dissolution processes and illustrate only the transport behavior of TNT; it is assumed that already dissolved TNT (i.e., to simulate situation where dissolution rate is not limiting) is released into the water column. No net loss of TNT from the water column is allowed to exist from any other process, except the hydrodynamic dispersion and tidal flushing through the mouth of the bay. Hydrodynamic dispersion redistributes TNT concentrations and tidal flushing through the mouth of the bay provides a net mass loss of TNT out of the model domain. When a steady-state condition is reached, mass loss rate of TNT by

flushing through the mouth of the bay should be balanced by the net release rate of TNT from the breached shell. Therefore, results shown in Figure 52 and Figure 53 can be considered conservative estimates of TNT exposure from single-shell source releases.

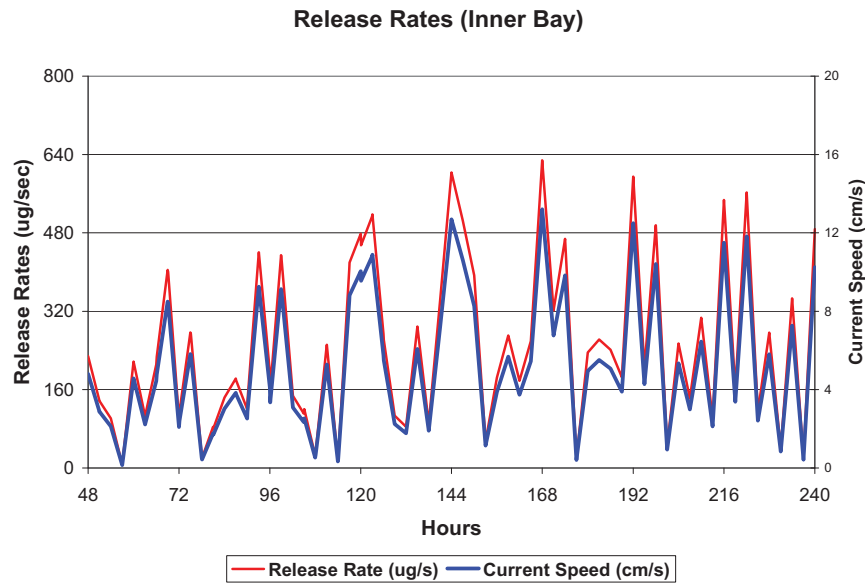


Figure 50. Current speed and estimated release rate at the inner San Diego Bay location.

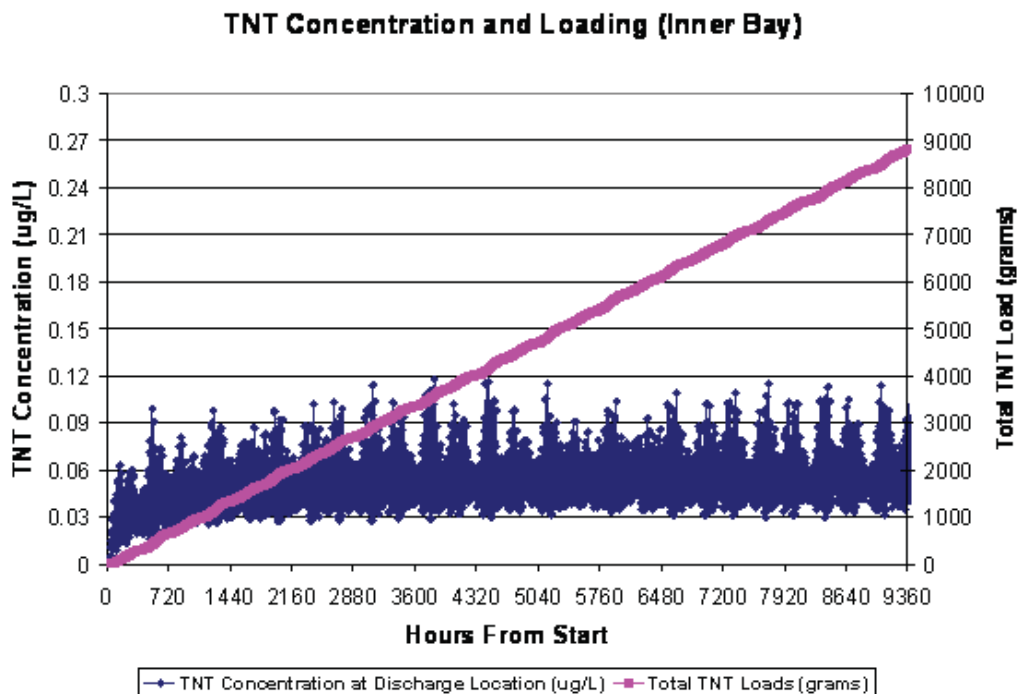


Figure 51. Simulated TNT concentration at the source location (inner San Diego Bay) and total TNT load during 1-year period.

TNT_base 01

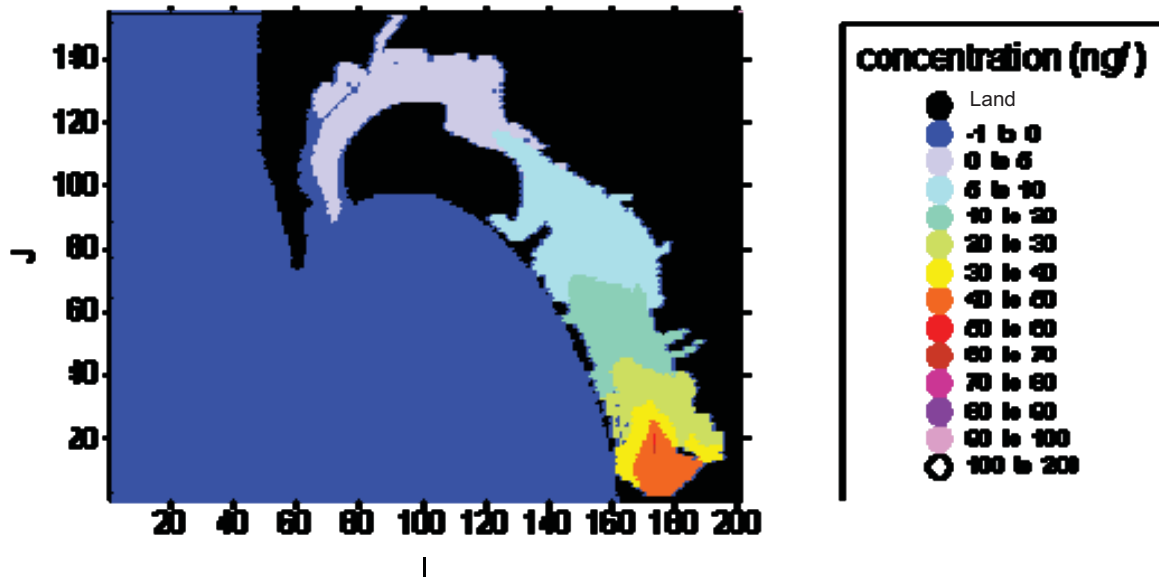


Figure 52. Steady-state TNT concentration during ebb tide (simulated release from inner San Diego Bay) (x-y coordinates are distances with I, J indices multiplied by 100 meters, the same convention hereafter).

In a separate study, the mineralization of TNT, RDX, and HMX in marine water and sediments was reported in Montgomery *et al.*, 2008.

These mineralization rates represent neither a zero or first-order process. For modeling purposes, we used these reported mineralization measurements to estimate and incorporate pseudo-first-order TNT degradation kinetics into the models. As shown in Table 17, 1.5% of the TNT is mineralized in marine sediment and seawater by the end of the first day. This daily mineralization rate is equivalent to a first-order mineralization rate of 0.0151 day^{-1} . Simulations with TRIM2D using this mineralization rate were conducted and the resulting simulated steady-state concentrations are shown in Figure 54 and can be compared to the results without mineralization as shown in Figure 52.

Scenario B. For this scenario, current speeds near the Naval Station San Diego are on the order of 4 cm/s and the corresponding release rates are approximately 150 ug/s. Release rate during the entire 1-year period is current-controlled, due to the relative low current speed and tidal fluctuations, as shown in Figure 55.

Simulated steady-state TNT concentrations are shown in Figure 56 through Figure 58. Generally, as observed previously in Scenario #1, steady-state concentrations decrease from the source, resulting from hydrodynamic transport and dispersion within the bay. Simulated steady-state TNT concentration ranges were $\sim 8 \text{ ng/L}$ in the inner bay, $\sim 4 \text{ ng/L}$ in the mid-bay areas, and $\sim 1 \text{ ng/L}$ near the bay mouth. The highest TNT concentrations ($\sim 15 \text{ ng/L}$) occur near the source region, at Naval Station San Diego. Due to the weaker current speed at this location in the bay, annual release of TNT from the breached shell at Naval Station San Diego is only about 5 kg/year, in comparison with the larger release rate of about 8.4 kg/year in the southern inner bay (Scenario #1) (Figure 51). Simulated steady-state concentrations taking into account the previously described first-order mineralization rate are shown in Figure 59.

In a separate study, the mineralization of TNT, RDX, and HMX in marine water and sediments was reported in Montgomery *et al.*, 2008.

These mineralization rates represent neither a zero or first-order process. For modeling purposes, we used these reported mineralization measurements to estimate and incorporate pseudo-first-order TNT degradation kinetics into the models. As shown in Table 17, 1.5% of the TNT is mineralized in marine sediment and seawater by the end of the first day. This daily mineralization rate is equivalent to a first-order mineralization rate of 0.0151 day^{-1} . Simulations with TRIM2D using this mineralization rate were conducted and the resulting simulated steady-state concentrations are shown in Figure 54 and can be compared to the results without mineralization as shown in Figure 52.

Scenario B. For this scenario, current speeds near the Naval Station San Diego are on the order of 4 cm/s and the corresponding release rates are approximately 150 ug/s. Release rate during the entire 1-year period is current-controlled, due to the relative low current speed and tidal fluctuations, as shown in Figure 55.

Simulated steady-state TNT concentrations are shown in Figure 56 through Figure 58. Generally, as observed previously in Scenario #1, steady-state concentrations decrease from the source, resulting from hydrodynamic transport and dispersion within the bay. Simulated steady-state TNT concentration ranges were $\sim 8 \text{ ng/L}$ in the inner bay, $\sim 4 \text{ ng/L}$ in the mid-bay areas, and $\sim 1 \text{ ng/L}$ near the bay mouth. The highest TNT concentrations ($\sim 15 \text{ ng/L}$) occur near the source region, at Naval Station San Diego. Due to the weaker current speed at this location in the bay, annual release of TNT from the breached shell at Naval Station San Diego is only about 5 kg/year, in comparison with the larger release rate of about 8.4 kg/year in the southern inner bay (Scenario #1) (Figure 51). Simulated steady-state concentrations taking into account the previously described first-order mineralization rate are shown in Figure 59.

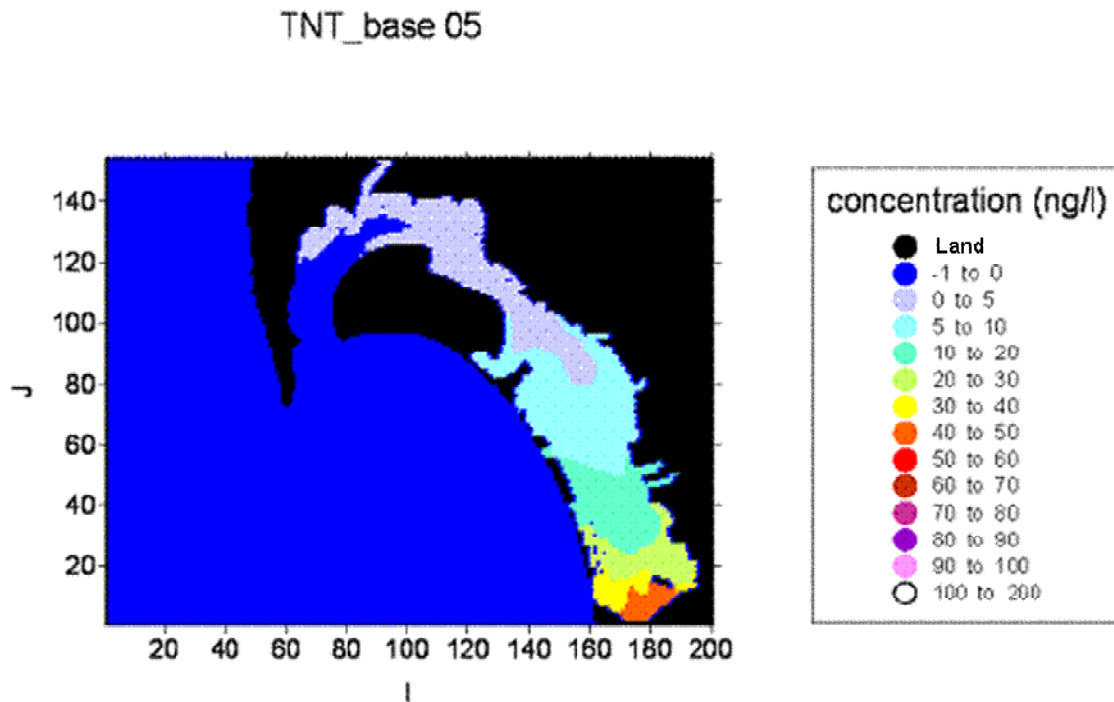


Figure 53. Steady-state TNT concentration during flooding tide (simulated release from inner San Diego Bay).

TNT_base 1 (12/12/06)

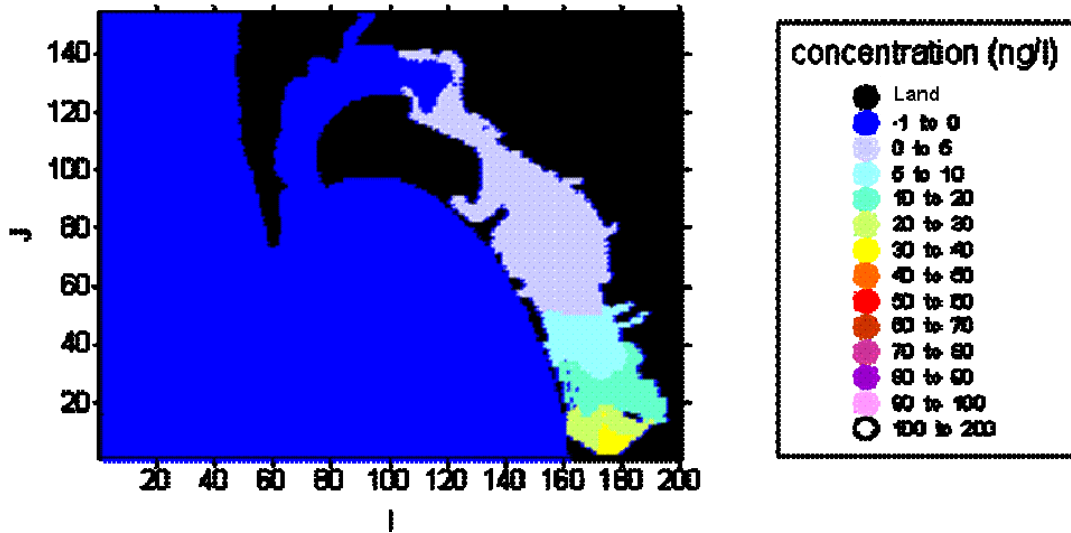


Figure 54. Steady-state TNT concentrations with first-order mineralization during ebb tide (simulated release from inner San Diego Bay).

Table 17. Mineralization rates for TNT (data provided by Dr. Mike Montgomery, NRL).

Microbial Assemblage Type	TNT Mineralization		
	Rate ($\mu\text{g/L}$ (or Kg)/day)	% of added TNT	%/day
Marine sediment	3 to 17	3	1.5
Seawater	3 to 5	3	1.5

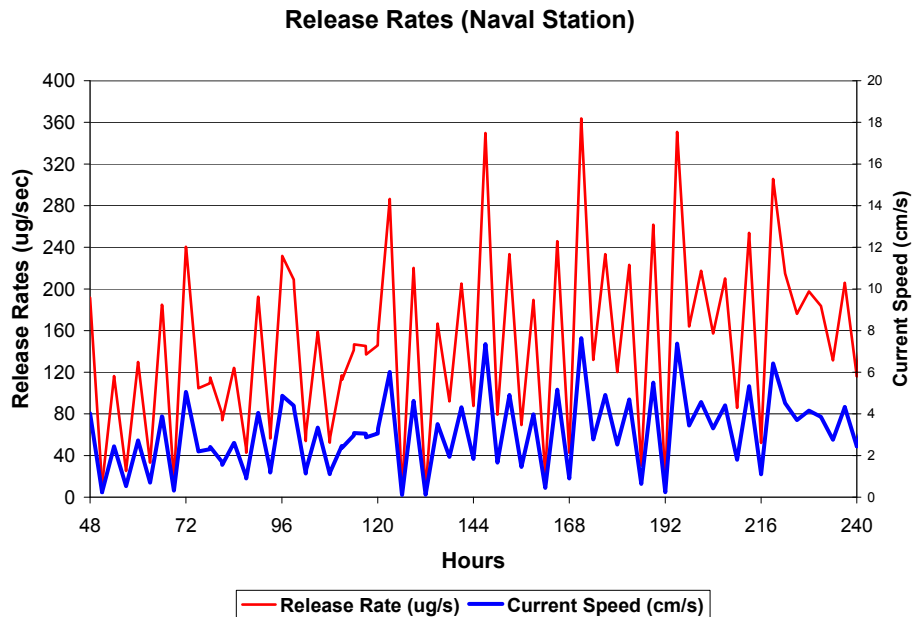


Figure 55. Current speed and estimated release rate at Naval Station San Diego.

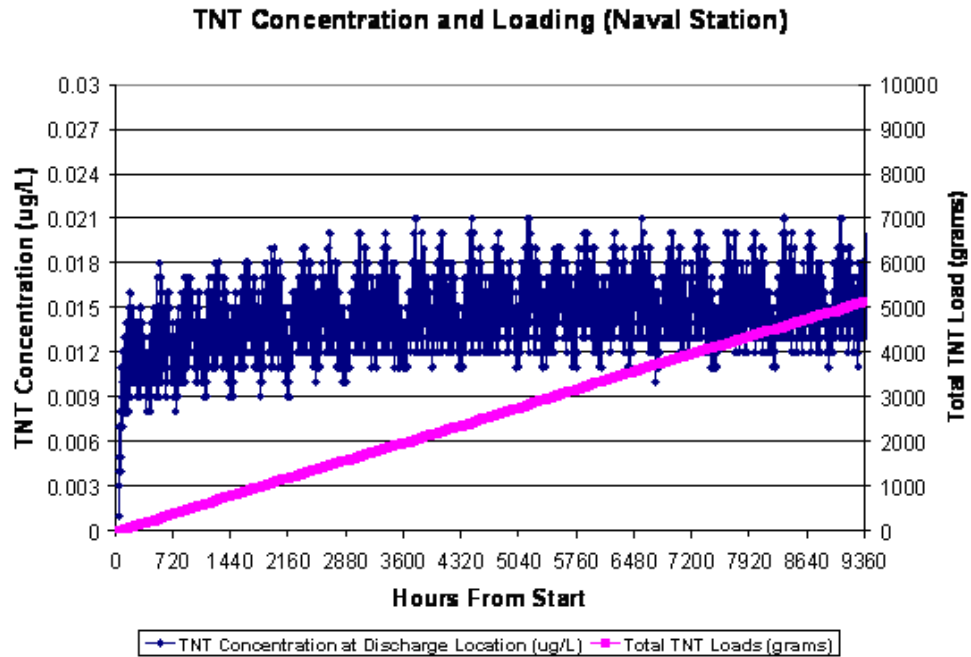


Figure 56. Simulated TNT concentration at the source location (Naval Station San Diego) and total TNT load during 1-year period.

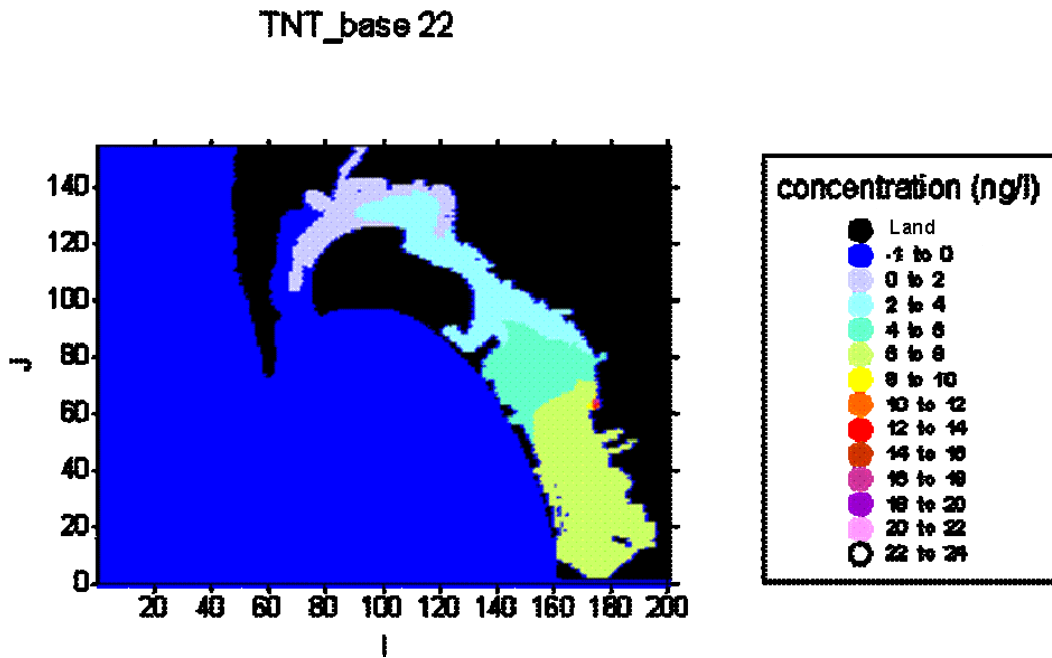


Figure 57. Steady-state TNT concentrations during ebb tide (simulated release from Naval Station San Diego).

TNT_base 25

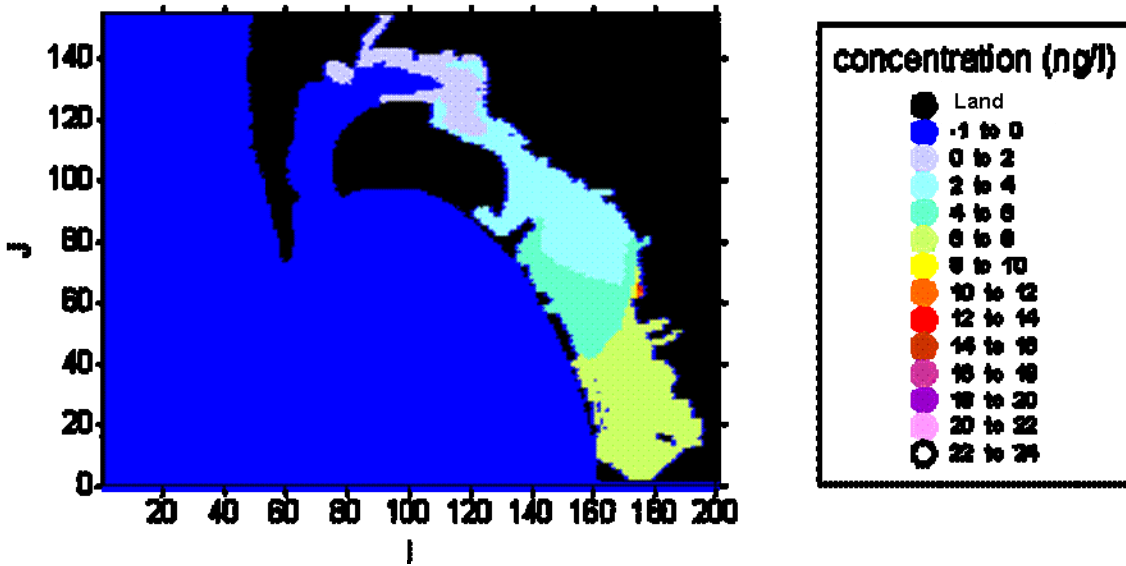


Figure 58. Steady-state TNT concentrations during flooding tide (simulated release from Naval Station San Diego).

TNT_base 2 (12/12/06)

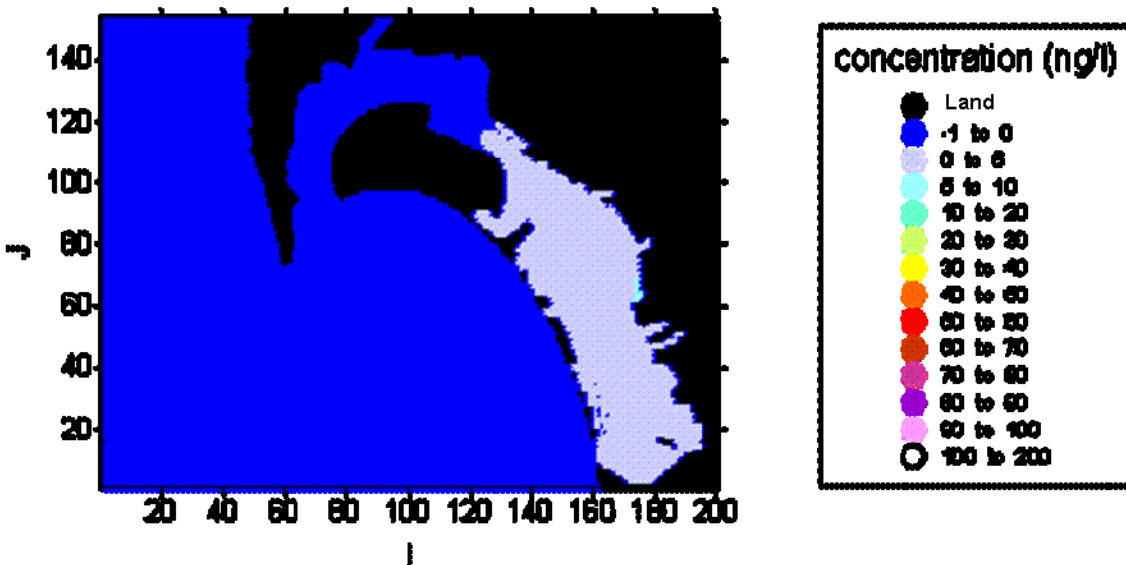


Figure 59. Steady-state TNT concentrations with mineralization of TNT during flooding tide (simulated release from Naval Station San Diego).

For these simulations with TRIM2D, as with Scenario #1, it is assumed that all TNT released from the breached shells is in the form of dissolved species (aqueous TNT concentrations). The only TNT mass loss term included is a result of flushing dissolved TNT out of the bay by currents and hydrodynamic dispersion. No loss to the sediment is assumed. Therefore, this approach focuses on a maximum dissolved TNT concentration, and fine-resolution model results from TRIM2D can be considered upper-bound estimates for steady-state TNT concentrations in the water column. Thus, the predicted steady-state TNT concentrations using TRIM2D throughout the bay can be considered conservative estimates.

4.4.2 WASP7 Model Results

For verification for the San Diego Bay model, WASP7-simulated results are compared with those previously simulated by TRIM2D. To compare with results from the TRIM2D model, which are considered conservative predictions for water column concentration, a steady-state TNT loading rate of 8.4 kg/year (Case #1 for TRIM2D modeling scenario) was also used for loading into WASP7 Box #1 (refer to Figure 30). Model simulations were run until model results reached steady-state. Figure 60 shows the simulated steady-state TNT concentrations for the eight boxes of the water column of the San Diego Bay for Cases 1a and 1b. For Case 1a, hydrodynamic dispersion is the only driving force for the TNT transport. Simulated TNT concentrations in the water column range from ~45 ng/L in the inner bay (Box #1), where the TNT source is released, to ~5 ng/L in the middle bay and < 1 ng/L near the mouth. TRIM2D results are volume-averaged for each of the eight boxes and compared with WASP results. As shown in Figure 60, the WASP-simulated TNT concentrations are very close to the TRIM-simulated TNT concentrations, even though these two models use different solution schemes and grid resolutions. The results for Case 1b also compare well with the results from TRIM2D results (Figure 60) for the corresponding scenarios.

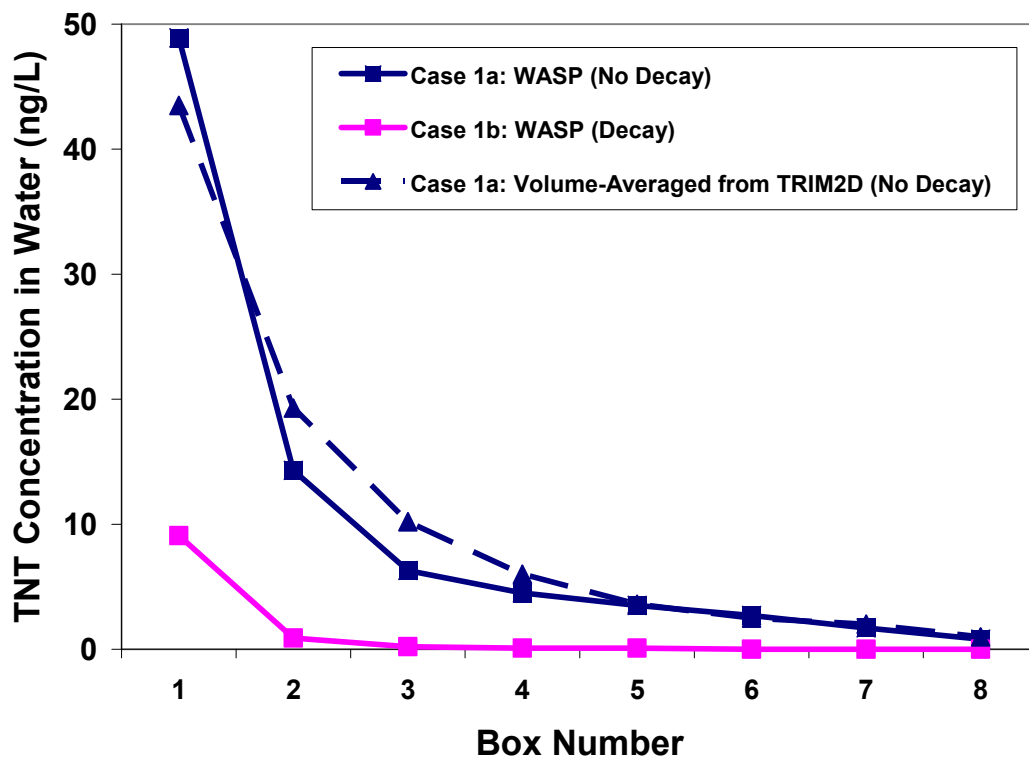


Figure 60. Wasp7-simulated TNT concentrations in water column for Cases 1a and 1b.

Unlike TRIM2D, WASP7 can simulate exchange of solids and particulate contaminants across the water/sediment interface by partitioning and settling/resuspension. Two partitioning coefficients, 0.9 and 5.0 L/Kg, represent the lower and upper bounds from the literature values (Case 2a). As discussed in the literature, partitioning coefficients for TNT (in soil) are low and hence, we would expect that only a small portion of TNT mass would be trapped in sediment. As shown in Figure 61, with the 5.5 L/Kg partitioning coefficient, TNT concentrations in sediment range from 0.1 ng/L for Box #1 to 0.0001 ng/L for Box #8. With a smaller partitioning coefficient, simulated TNT concentrations in sediment are even lower, ranging from 0.02 ng/L for Box #1 to 0.00001 ng/L for Box #8. While these concentrations are low, note that these are simulated concentrations from TNT release from a single breached shell. When multiple shells exist and are taken into account, their accumulated concentration needs further study.

Model simulations with two partitioning coefficients, i.e., 5.54 and 0.88 L/kg, with/without a first-order mineralization rate constant (0.0151 day^{-1}) were then conducted, Steady-state TNT concentrations are shown in Figure 61. Generally, TNT concentrations in San Diego Bay, which is similar to most estuaries, are primarily governed by hydrodynamic transport, including bay flushing and hydrodynamic dispersion. For San Diego Bay, hydrodynamic transport governs the primary distributions of TNT released from a single breached shell. Steady-state concentrations result from an equilibrium achieved between the TNT source and the hydrodynamic dispersion. Generally, TNT concentrations in sediment are proportional to a partitioning coefficient, as shown in Figure 61. With the first-order mineralization, steady-state concentrations in sediment decrease by 20% or less.

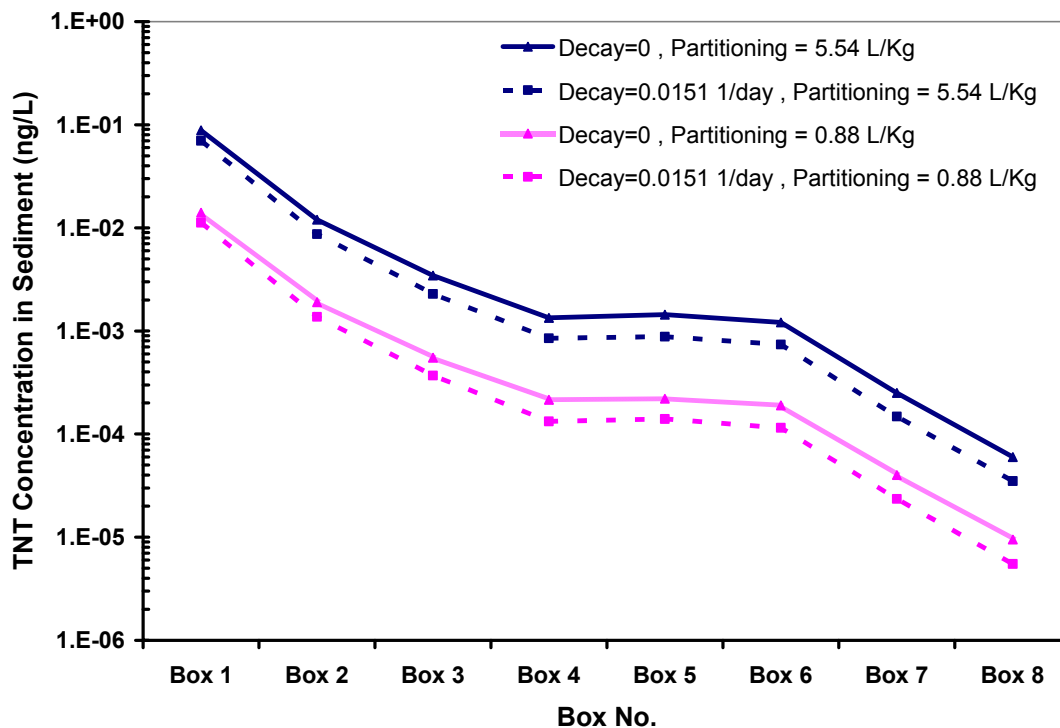


Figure 61. WASP7-simulated TNT concentrations in sediment for Case 2a (water column transport and exchange with sediment) and 2b (with mineralization) for different partitioning coefficients for San Diego Bay.

For the Elizabeth River model (Figure 29), we release the 8 kg/year TNT at three different boxes, #2, #6, and #12 which are located upstream, middle portion, and downstream of the main river stretch. Unlike San Diego Bay, riverine freshwater in Elizabeth River flows from upstream all the way to the downstream mouth regions. Therefore, freshwater flushing exists throughout the river. Figure 62 shows that release in Box #2 generates a maximum steady-state concentration of ~42 ng/L. Release in Box #6 produces a maximum concentration of ~25 ng/L at Box #6, which is almost equal to the concentration resulting at Box #6 upon release in Box #2. The same phenomenon is observed for release in Box #12. Release in Box #12 produces a maximum concentration of ~5 ng/L at Box #12, which is close to the concentration resulting at Box #12 upon release in Box #2. These phenomena are consistent with processes occurring in a conservative system. Since in this case, there is no mineralization and the transport equation satisfies conservation of mass law, the patterns of the predicted concentrations are reasonable.

With the mineralization rate, simulated TNT concentrations in the water column show reduced concentrations in the water column as shown in Figure 63. On average, a decrease of ~15% in simulated concentrations is observed.

Simulated TNT concentrations in sediment for two different partitioning coefficients, 0.88 and 5.54 L/Kg, both with and without mineralization are shown in Figure 64 (TNT release in Box #2) and Figure 65 (TNT release in Box #6). Simulated TNT concentrations in sediment are approximately proportional to the partitioning coefficient, *i.e.*, the higher partitioning coefficients are associated with higher concentrations in sediment, similar to the results for San Diego Bay.

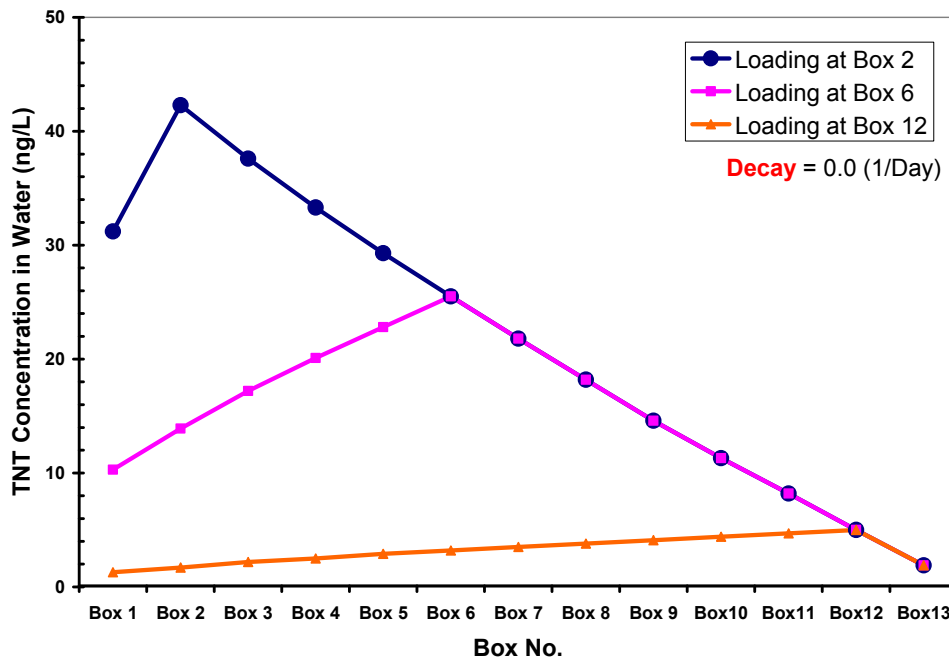


Figure 62. Simulated TNT concentrations in water column for Case 3a, with TNT release occurring in Box #2, #6, and #12, respectively.

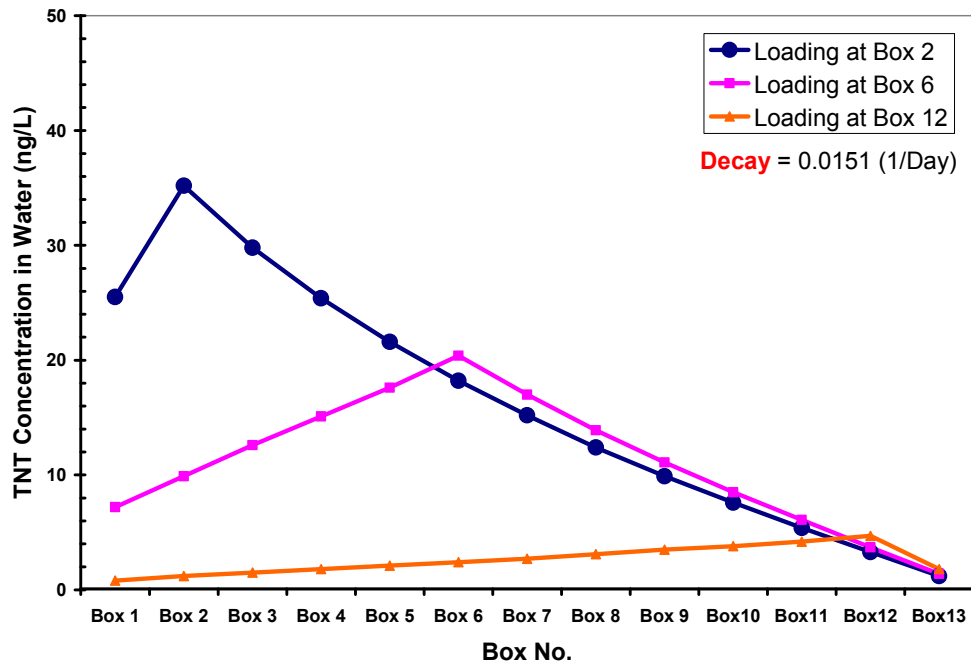


Figure 63. Simulated TNT concentrations in water column for Case 3b, with TNT release occurring in Box #2, #6, and #12, respectively.

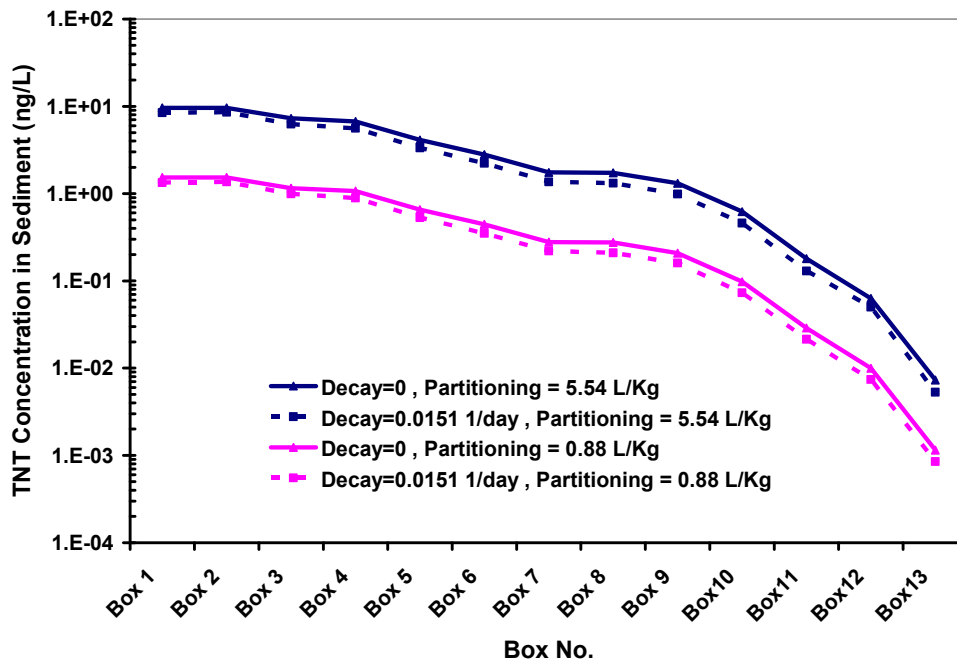


Figure 64. Simulated TNT concentrations in sediment for Case 4a (with partitioning coefficients without mineralization) and Case 4b (with mineralization), with TNT release occurring in Box #2.

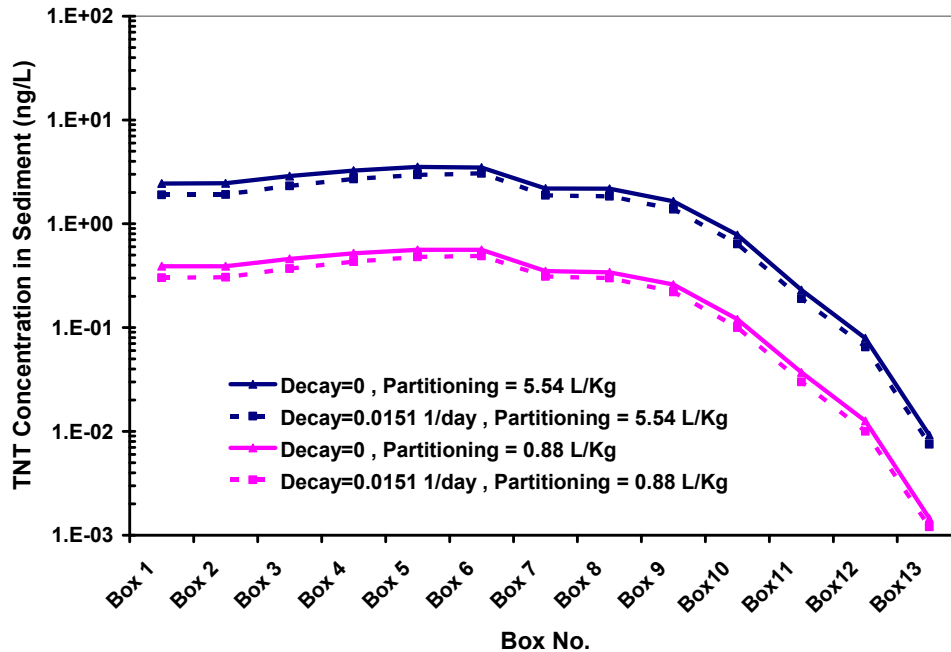


Figure 65. Simulated TNT concentrations in sediment for Case 4a (with partitioning coefficients and without mineralization) and Case 4b (with mineralization), with TNT release occurring in Box #6.

4.5 RESULTS OF TASKS 4.3.1A, 4.3.1B, 4.3.2, AND 4.3.6

Study results of the four Phase III tasks (Figure 3) are discussed. These results include both the numerical modeling study and empirical study. These are explained as follows.

4.5.1 Effect of Shapes of Opening

The numerical model, FLUENT, was set up to simulate release of MC from holes of four different shapes, including a circle, a triangle, and two rectangles with the aspect ratios of 4:1 and 10:1, respectively. Areas for these four different opening shapes were the same, which is equal to $\pi/16$ (cm^2), e.g., the radius of the circle = 0.25 cm. Simulated release rates were plotted and compared, as shown in Figure 66.

As shown in Figure 66, the mass release rates are linearly proportional to the current speed (range of ~ 0.05 -50 cm/s (0.0005-0.5 m/s)), with two relatively constant slopes in two regions. For the region, $U < 15$ cm/s, the mass release rates remain almost the same for the four opening shapes (Figure 67). The slope is about 0.0079 for all the four shapes within the entire current speed range (except for circle at 0.15 m/s). This indicates that for weak flows, shapes of the hole openings do not have a major effect on the MC release rate. For the medium-high flow regimes, namely, $U > 0.15$ m/s, the mass release rates are linearly dependent on the current speed, but with different slopes for the different shapes (Figure 68).

Model results show that when ambient currents are weak (less than 0.15 m/s), hydrodynamic mixing of MC through the opening is also weak and the mass release rates can not differentiate the different shapes of the openings and differences of the mass release rates are small.

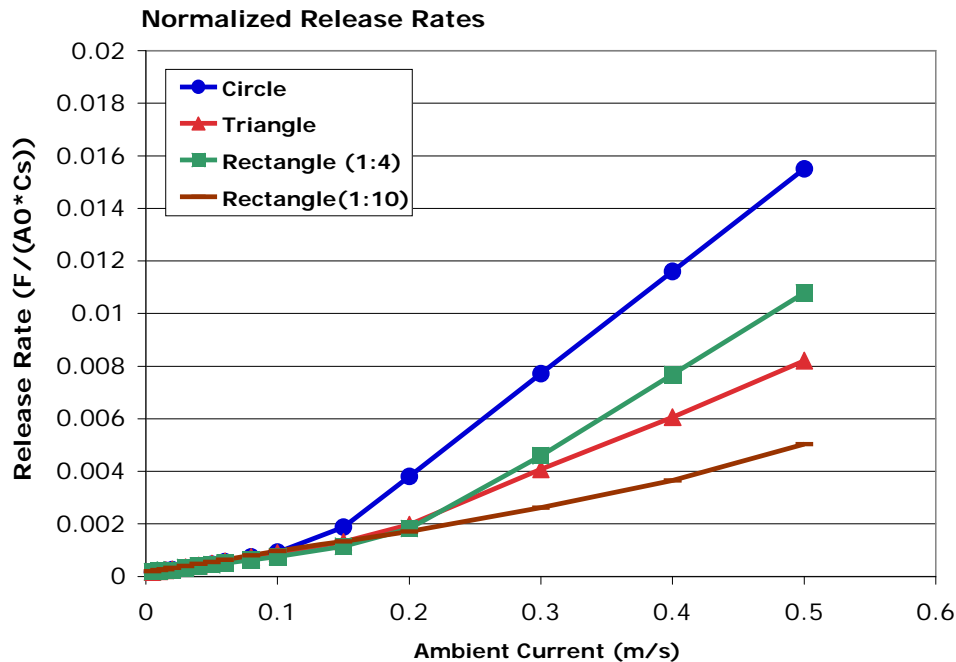
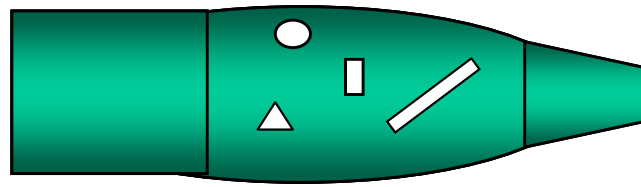
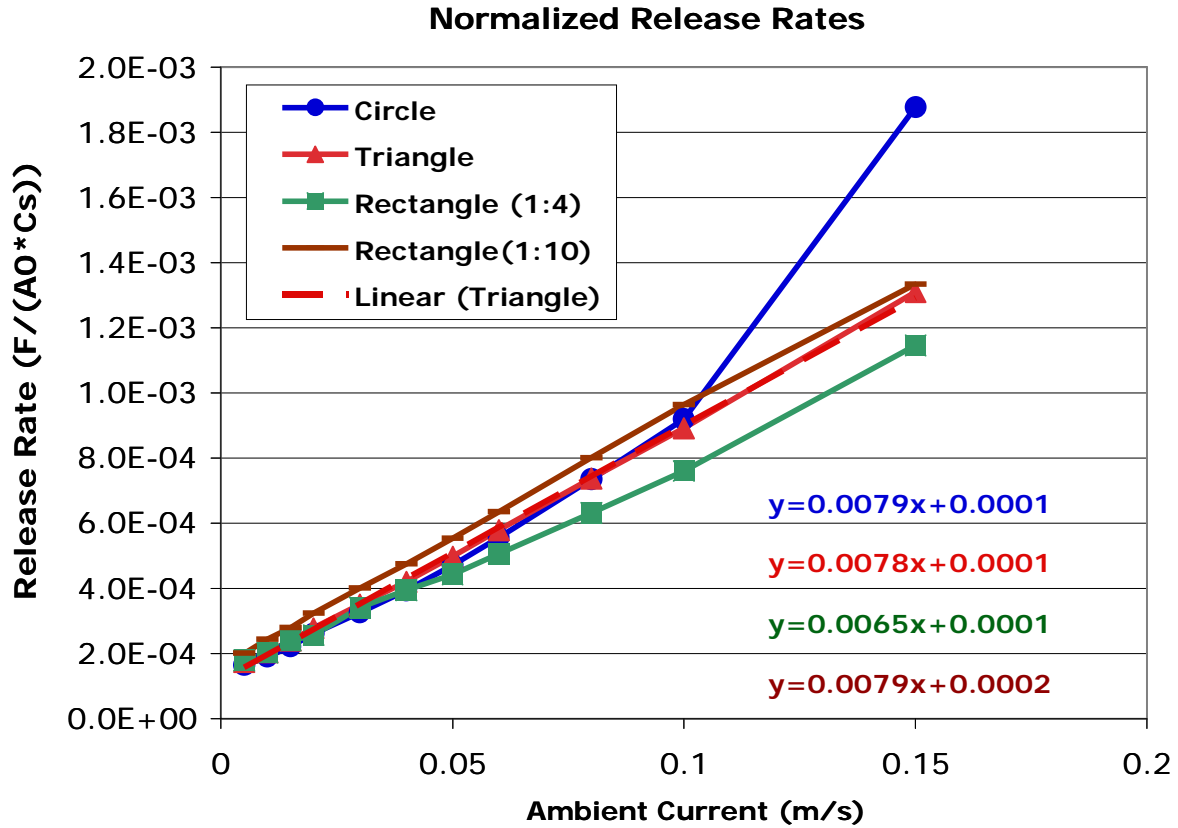


Figure 66. Four different shapes of opening (above) and normalized mass release rates at different current speed (lower).

When ambient currents become stronger ($U > 0.15$ m/s), hydrodynamic mixing of MC through the opening becomes stronger and the release rates are influenced by the shapes of the openings. Of the four different shapes, the circle produces the largest release rate (with a slope of 0.039), followed by the rectangle of 4:1 aspect ratio (0.028), and then by the triangle (0.02) and the rectangle of 10:1 aspect ratio produces the smallest mass release rate (with a slope of 0.011) (Figure 68).

4.5.2 Effect of Orientation of Opening (rectangle of 4:1 aspect ratio)

Breached holes are formed not only in different shapes, but also at different orientation angles relative to the current direction. For example, breached cracks may form that are in line or crossing with the ambient current. Effect due to orientation on the release rate was studied by simulating release rates for the rectangle (4:1) with the orientation angles ranging from 0° (current crosses with the long axis), to 45° and 90° (current in line with the long axis). Figure 69 shows that a 45° -angle produces the maximum release rate ($F = 0.041U - 0.0033$), and a 0° -angle produces the minimum release rate ($F = 0.028U - 0.004$). Such behavior of different orientation angles on the release rate may not be obvious intuitively. It may imply that local dispersion near the hole at different orientation angles might be more complex than originally thought. The model results show that differences on the release rates from different orientation angles are in the range of $\pm 25\%$, compared to the difference of twofold on the release rates from different shapes of openings.



Hydrodynamic Diffusivities are linearly dependent on ambient current:

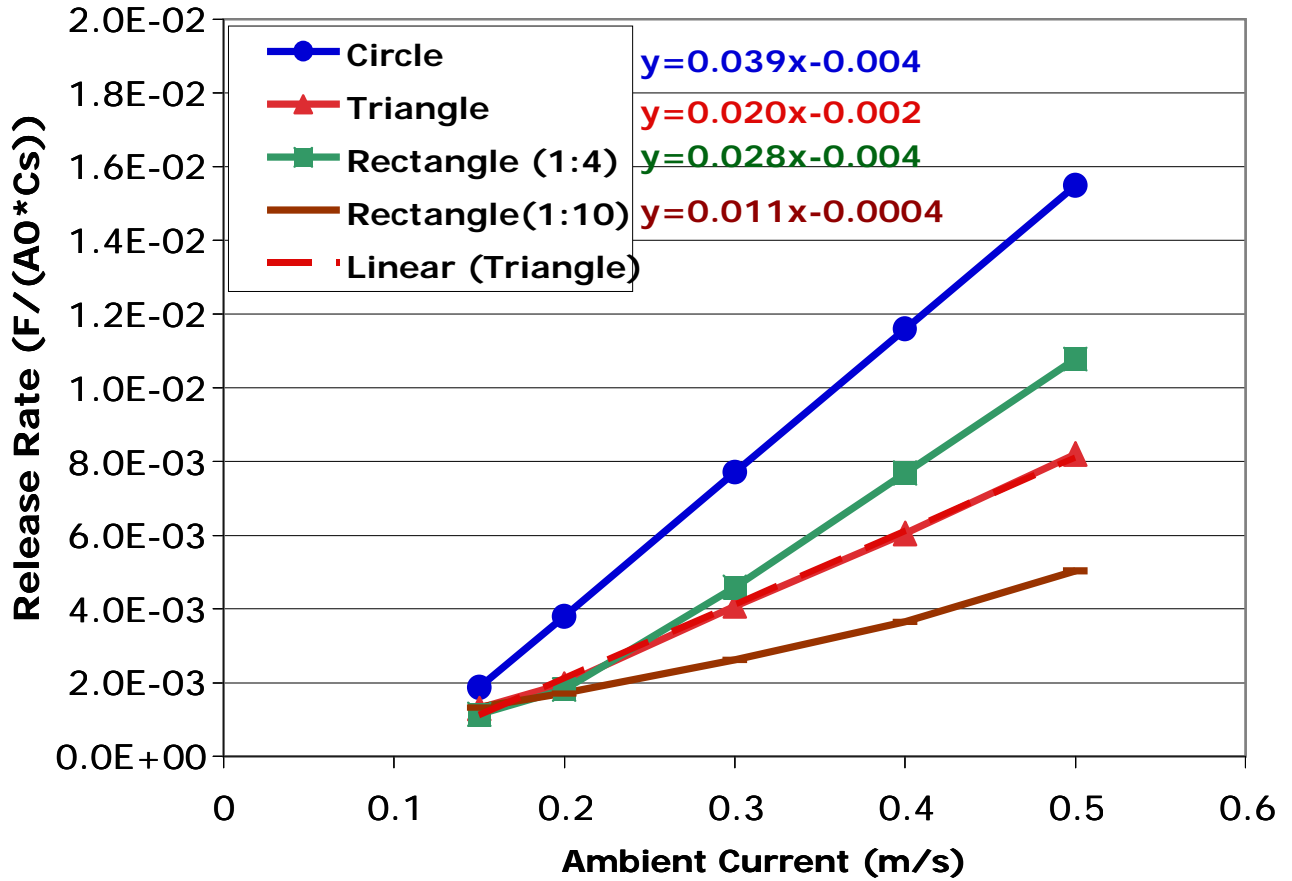
$$F_N = AU+B \sim 0.0079U$$

Regime I: $U < 15 \text{ cm/s}$

	●	▲	—	—
A	0.0079	0.0078	0.0065	0.0079
B	0.0001	0.0001	0.0001	0.0002

Figure 67. Normalized release rates vs. ambient current speed in the range of $0 < U < 0.15 \text{ m/s}$ (above), and the slopes for the four different shapes of openings.

Normalized Release Rates



Regime I: $U > 15 \text{ cm/s}$

				
A	0.039	0.020	0.028	0.011
B	-0.004	-0.002	-0.004	-0.0004

Figure 68. Normalized release rates vs. ambient current speed in the range of $0.15 \text{ m/s} < U$ (above), and the slopes for the four different shapes of openings.

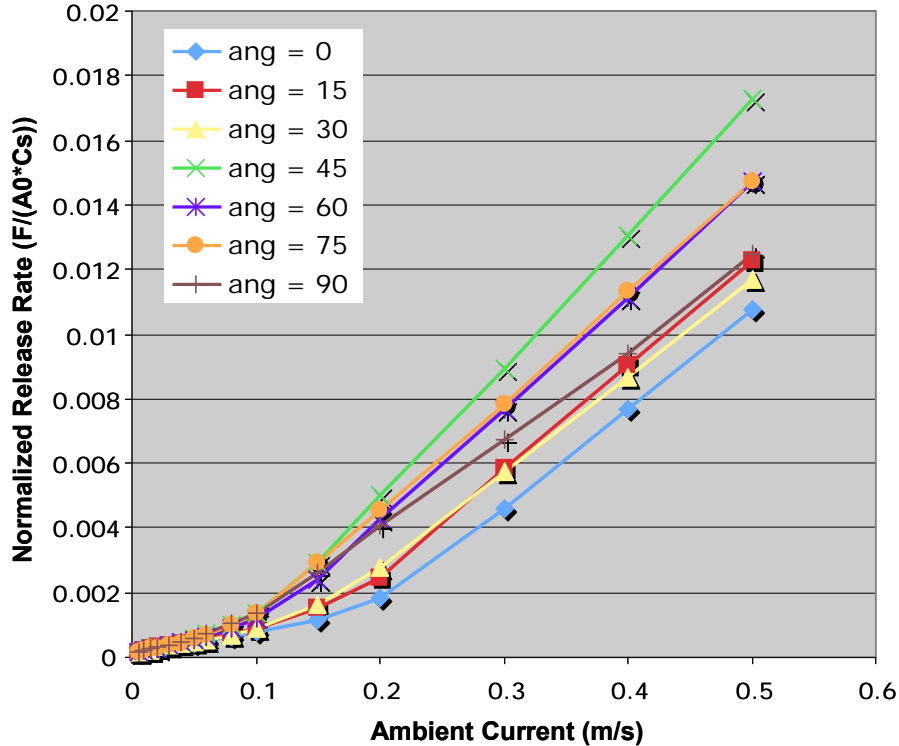


Figure 69. Normalized release rates vs. ambient current speed for rectangle (4:1 aspect ratio) at different orientation angles.

4.5.3 Internal Circulation

A FLUENT simulation was conducted to obtain the internal circulation pattern inside the half dome. The radius of the cavity, radius of the breach hole, and the mean current speed are $R = 35$ mm, $b = 2.5$ mm, and $U = 0.18$ m/s, respectively. The steady-state in-cavity circulation patterns are characterized by two jet streams, one pointing upward to the breach hole, and the other which seems to be emitted from the hole and shooting downward (Figure 70). There also appears to be two counter-rotating vortices on the two sides of the jets. Similar circulation patterns were measured by the PIV instrument as part of the experimental release rate study (Figure 13), except the downward jet is not appreciable. The location and shape of the upward jet and the two counter-rotating vortices are somewhat different from those seen in the experiment. Despite these differences, excellent agreement is found between the simulation and the experiment in terms of the magnitude of the circulation velocities. The variance of the distributed flow speed is 0.012 mm/s for simulation and 0.014 mm/s for the experiment. This is a more important fact as we argue that the overall magnitude of circulation speed determines the in-cavity mixing and thus the chemical release rate. It has verified that the in-cavity circulation is laminar as the overall circulation Reynolds Number $Re_c = u_c R / \nu = 12$ for the case we measured (where u_c is the average internal circulation speed, R is the radius of the cavity, and ν is the kinematic viscosity). Thus, the FLUENT simulation based on the laminar model is considered valid for inner circulation. We can also argue that although the outer flow is turbulent, its effect on the release of MC is confined to the near-breach area. Given that the size of the breach is small, the internal near-breach part is still laminar, i.e., in the viscous sublayer of the boundary layer. This is partially verified by the fact that the measured in-cavity circulation is almost steady. These two figures show that the flow speeds between model and measurement are of the same order of magnitude, with similar degree of variances. Based on both results, the Reynolds Number (Ub/ν) ~ 12 , where U is internal circulation speed (~ 5 mm/s), $b = 2.5$ mm, and ν is dynamic viscosity.

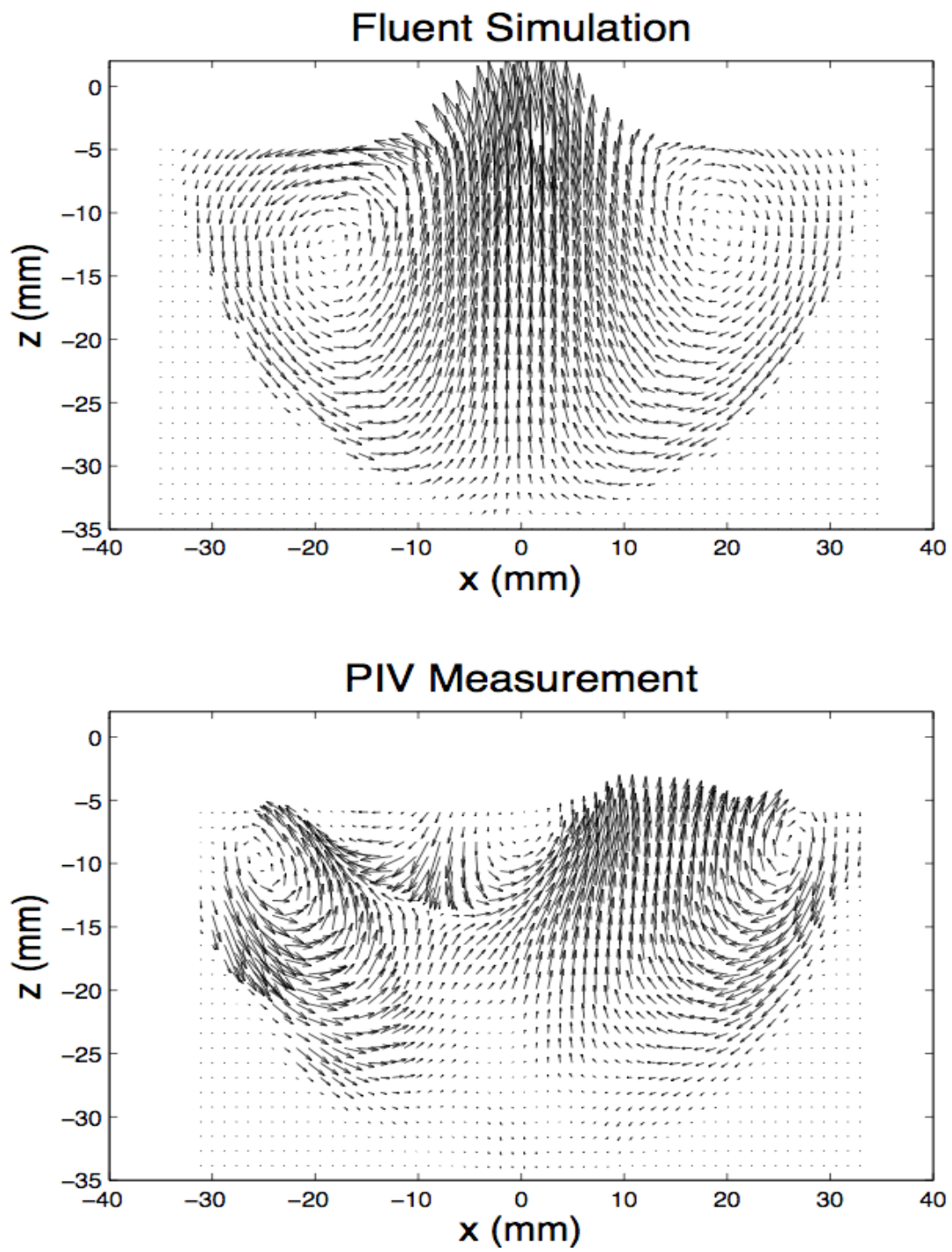


Figure 70. Model-simulated (above) and measured (below) internal circulation.

4.5.4 Probabilistic Modeling

The five variables governing the mass release rate function (F) for a single shell, as shown in Eq. (10a) can be prescribed either deterministically or probabilistically or as a combination of both:

$$F = \frac{2\pi DC_s}{\frac{2D}{\alpha Ub^2} + \frac{D}{\mu R^2} + \frac{1}{b} - \frac{1}{R}} \quad (43)$$

For example, the sizes of the holes (with b as the radius) on a single shell will vary or change in time. The hole sizes may involve a range or distribution function, which represents variability associated with the variable b . Ambient current U will also fluctuate due to the dynamic nature such as tidal forcing, wind, and freshwater effects of the marine environment in which these shells reside. Therefore, a range or distribution function is often used to prescribe a range of expected currents in the marine environment. Another source of probabilistic nature is the uncertainty or lack of data associated with certain variables. Hole sizes not only involve variability, they often are associated with uncertainty due to lack of sufficient data. To make meaningful predictions, uncertainty associated with certain variables can be prescribed by a probability function. Predictions should also be interpreted in a probabilistic fashion using an output distribution.

When the mass release rate function, developed for a single shell, is implemented for multiple shells, the number of shells for each shell type needs to be prescribed, deterministically or probabilistically. If it is prescribed probabilistically, it can also be processed in ways similar to those for the other variables. When multiple variables are prescribed probabilistically, each with its own distribution function, predictions would require a large number of calculations so that the variables with a probability distribution can be adequately sampled. To do this, we used the Monte Carlo method to perform the scenario simulations (results described below). For all of the Monte Carlo simulations, 10,000 calculations were conducted for each scenario. Simulation results from the 10,000 calculations showed no noticeable difference from the results of 1,000 calculations.

4.5.5 Monte Carlo Simulation Results

The first example scenario is for a single 24 inches \times 8 inches round with 8 kg of MC. Two variables use probabilistic input: the hole size and ambient current speed. The hole radius is assumed to be associated with a normal distribution with a mean and standard deviation of 2 and 0.75 cm, respectively. Ambient current speed is associated with a normal distribution with a mean and standard deviation of 15 and 5 cm/s, respectively. Saturation concentrations and dissolution speed for TNT were used and hydrodynamic dispersion coefficient was obtained from the FLUENT model. The resulting simulated release rates are also associated with a probabilistic range (0.01 to 0.033 mg/s) and an estimated time for the complete depletion of MC ranges from 8 to 12 years (Figure 71)

For the second example, the hole size is reduced from a 2-cm mean radius normal distribution to a 0.4-cm mean radius log-normal distribution. The predicted depletion time increases from 10 to 120 years (Figure 72).

The last scenario is similar to the second scenario, except that the number of shells has a normal distribution with a mean and standard deviation of 100 and 30, respectively. Figure 73[a] shows the simulated release rate distribution for a single shell. When these two numbers were multiplied in the Monte Carlo manner, total release rates were simulated and results are shown in Figure 73 [c]. Figure 73[d] shows the probability for each release time or bin time it takes to completely release 8 kg of MC from each of 100 shells for the scenarios. And the total cumulative probability for complete release of all shells can be obtained by integrating all the bins in the curve (\sim 120 years).

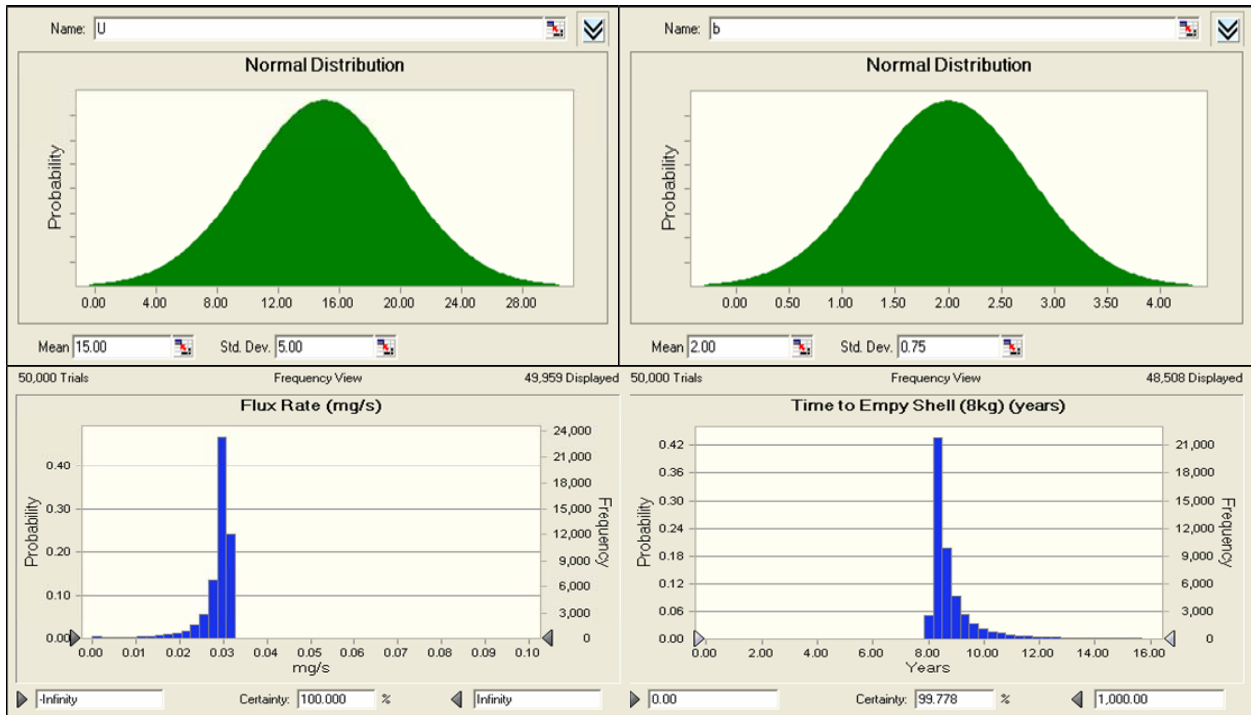


Figure 71. Monte Carlo simulation for release rate and time for complete depletion of MC; b has a normal distribution.

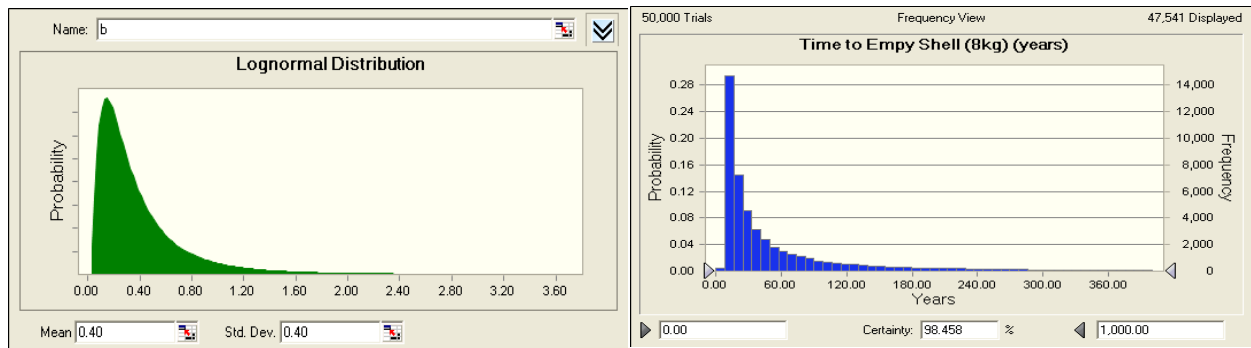


Figure 72. Monte Carlo simulations for release rate and time for complete depletion of MC; b has a log-normal distribution.

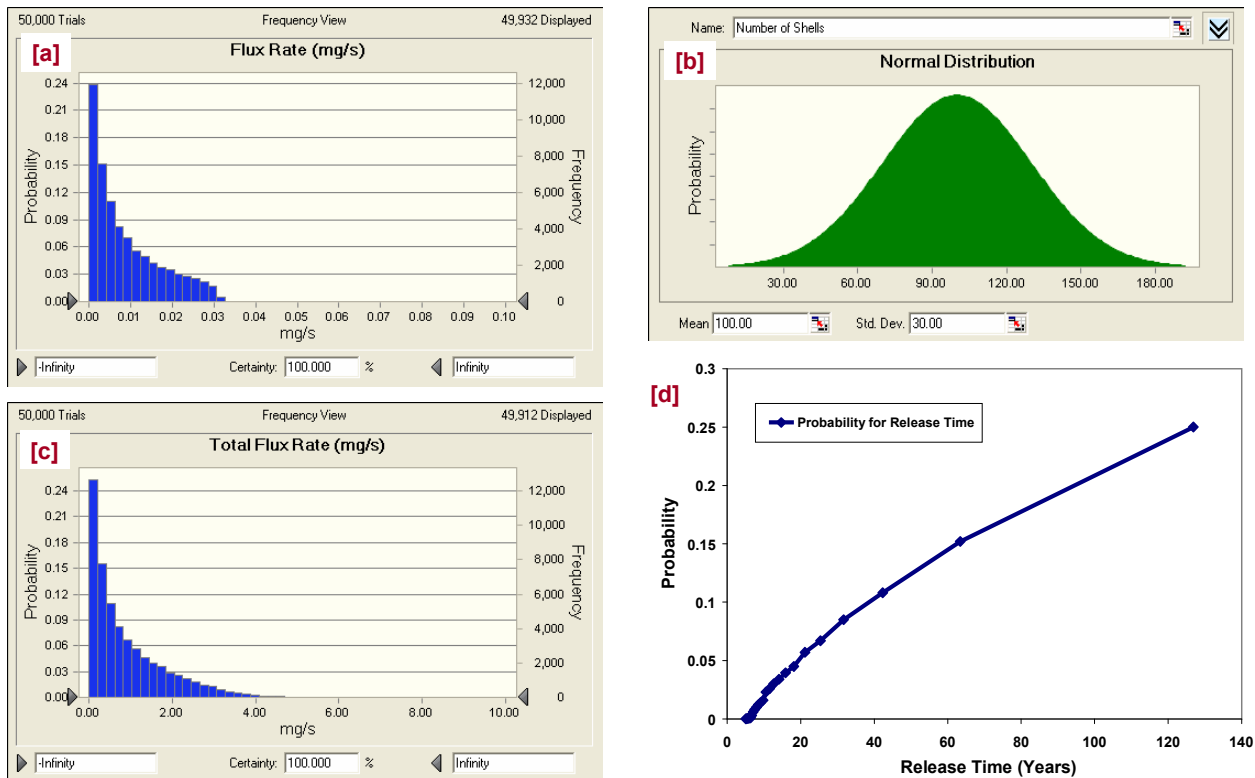


Figure 73. Simulated release rate for group of shells, [a], prescribed probability distribution for shell number with a mean of 100 and standard deviation of 30, [b], and simulated total release rate, [c], and probability of release time, [d].

The probabilistic model is based on the analytical release rate function. The multiple variables can be treated both deterministically and/or probabilistically, or a combination of both. When the mass release rate function is implemented in the field, the number of shells can be added into the function as a multiplicative term. For real scenarios, the three variables that are most likely associated with probabilistic estimation, would include number/type of shells, hole size, and ambient current. Study results in this section demonstrate that the Monte Carlo simulation is effective in quantifying the effect on mass release rate when multiple variables are associated with probability distributions.

4.6 EMPIRICAL STUDY RESULTS – BURIED SHELL

Results from 18 test runs described in Section 3.4 are presented in Figure 74 through Figure 91. Time histories of the exit dye concentration C_{out} and log-transformed C_{out} values are shown in the following figures. A log-linear profile would indicate that the model Eqs. (28) and (29) proposed in the above section is valid, and that the mass release velocity u_f can be estimated from linear regression (note: sporadic excursions or “spikes” can be found in some datasets, which are considered to be due to sensor errors).

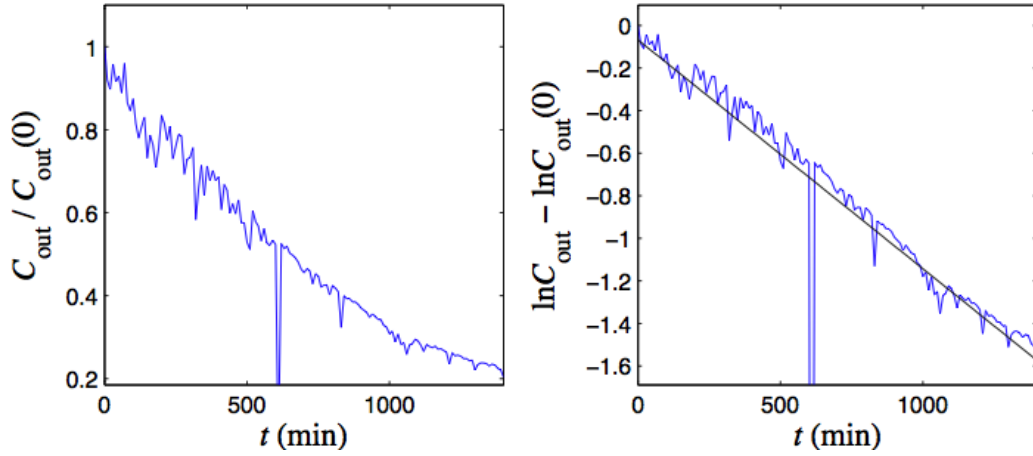


Figure 74. Fine sand, low seepage flow ($\Delta h = 1''$), crack hole diameter ($d_b = 0.21$ cm).

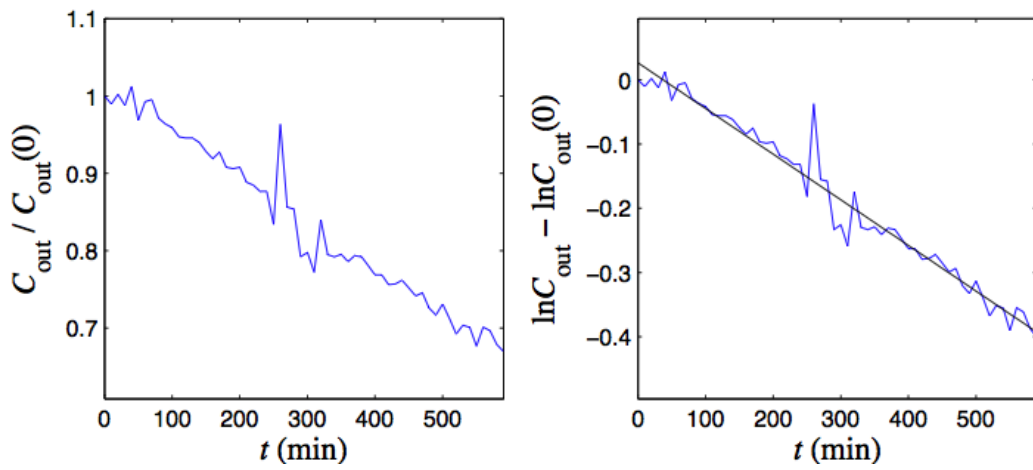


Figure 75. Fine sand, medium seepage flow ($\Delta h = 2''$), crack hole diameter ($d_b = 0.21$ cm).

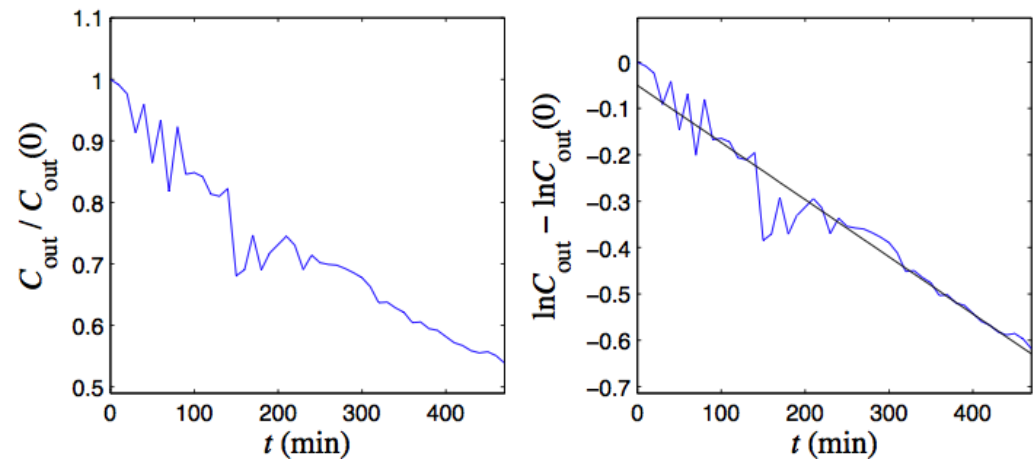


Figure 76. Fine sand, high seepage flow ($\Delta h = 3''$), crack hole diameter ($d_b = 0.21$ cm).

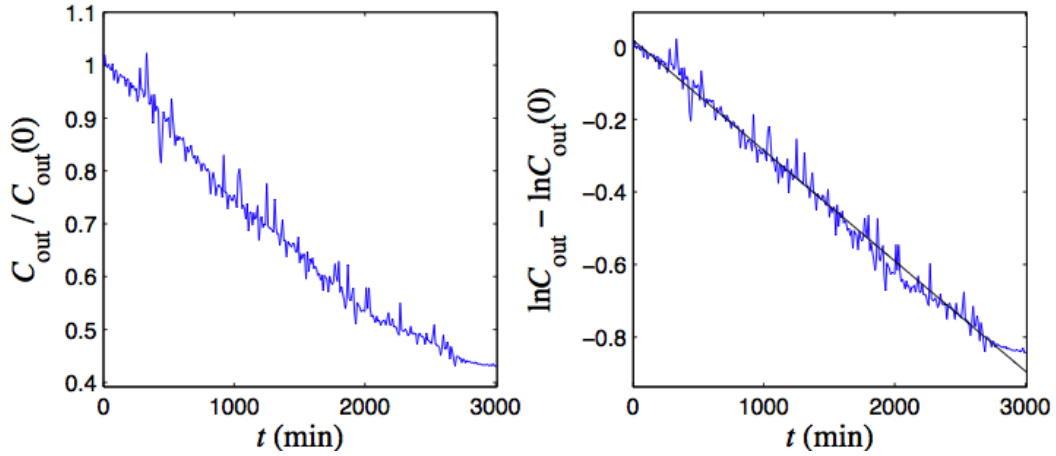


Figure 77. Fine sand, low seepage flow ($\Delta h = 1''$), crack hole diameter ($d_b = 0.40$ cm).

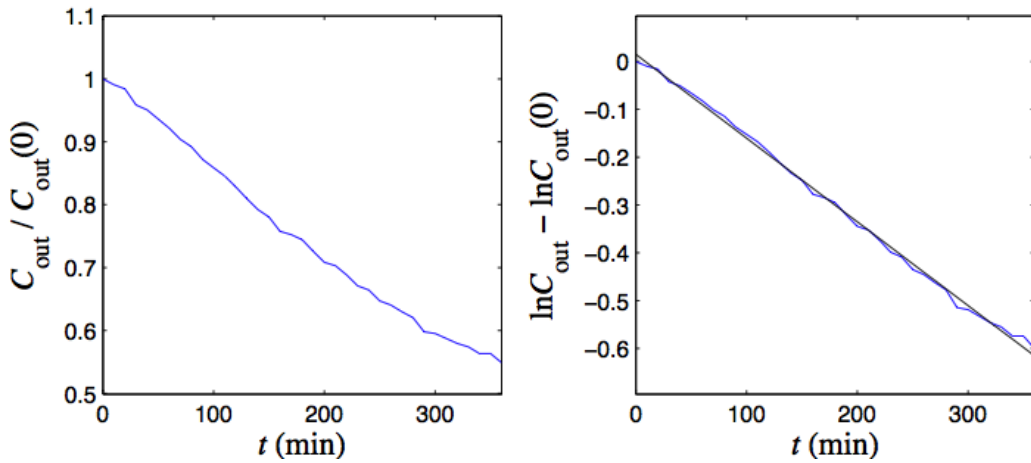


Figure 78. Fine sand, medium seepage flow ($\Delta h = 2''$), crack hole diameter ($d_b = 0.40$ cm).

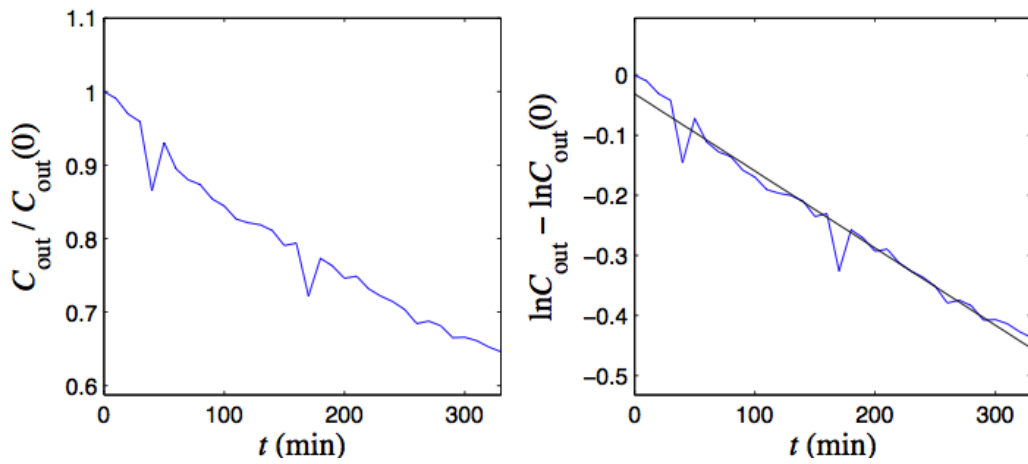


Figure 79. Fine sand, high seepage flow ($\Delta h = 3''$), crack hole diameter ($d_b = 0.40$ cm).

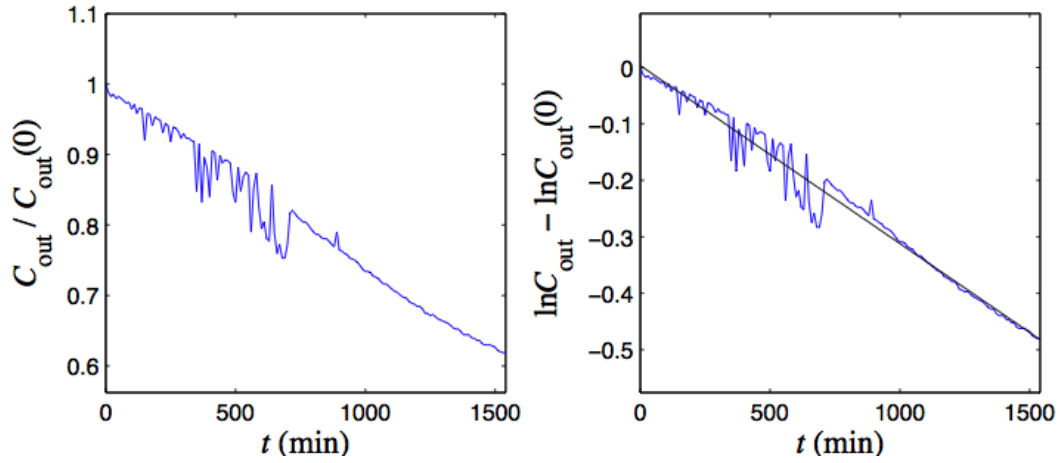


Figure 80. Fine sand, low seepage flow ($\Delta h = 1''$), crack hole diameter ($d_b = 0.56$ cm).

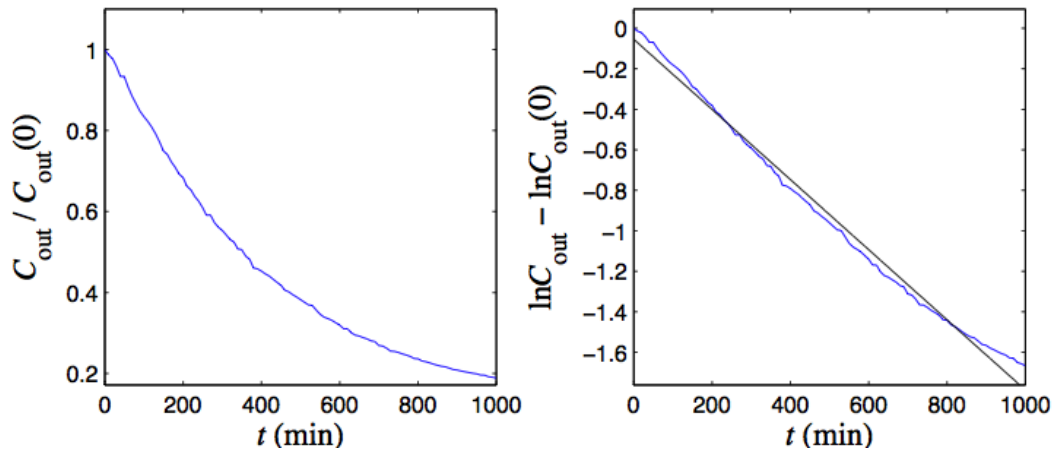


Figure 81. Fine sand, medium seepage flow ($\Delta h = 2''$), crack hole diameter ($d_b = 0.56$ cm).

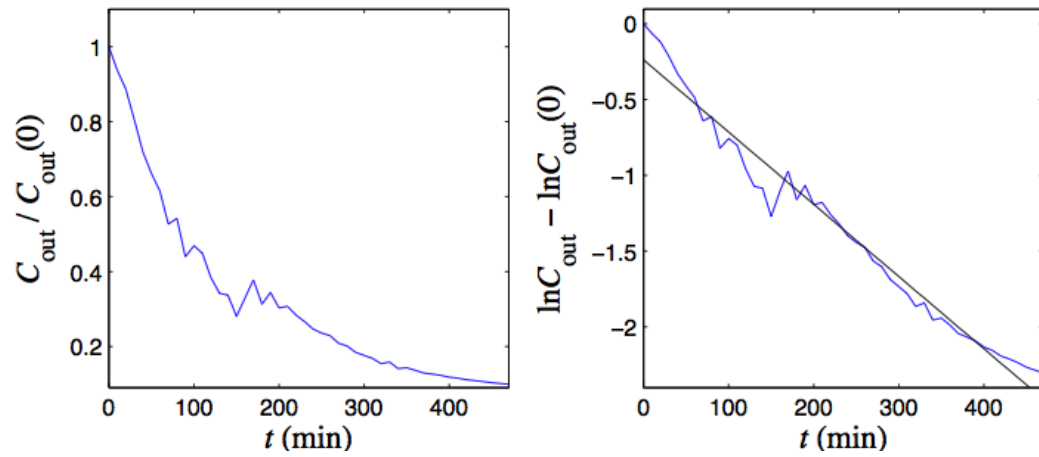


Figure 82. Fine sand, high seepage flow ($\Delta h = 3''$), crack hole diameter ($d_b = 0.56$ cm).

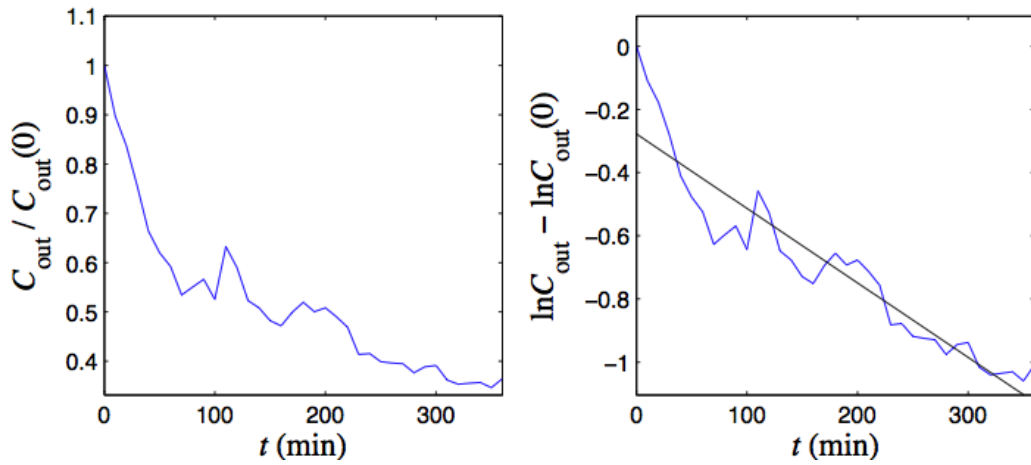


Figure 83. Coarse sand, low seepage flow ($\Delta h = 1''$), crack hole (diameter $d_b = 0.21$ cm).

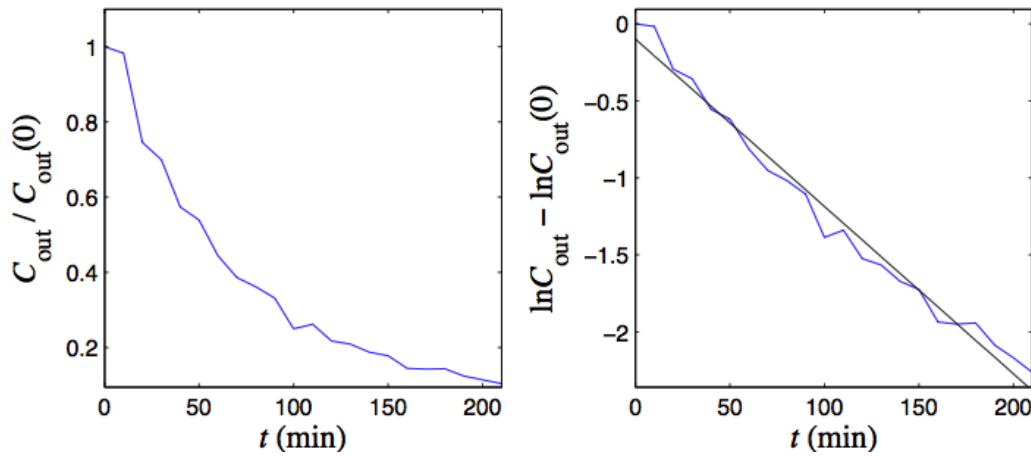


Figure 84. Coarse sand, medium seepage flow ($\Delta h = 2''$), crack hole diameter $d_b = 0.21$ cm.

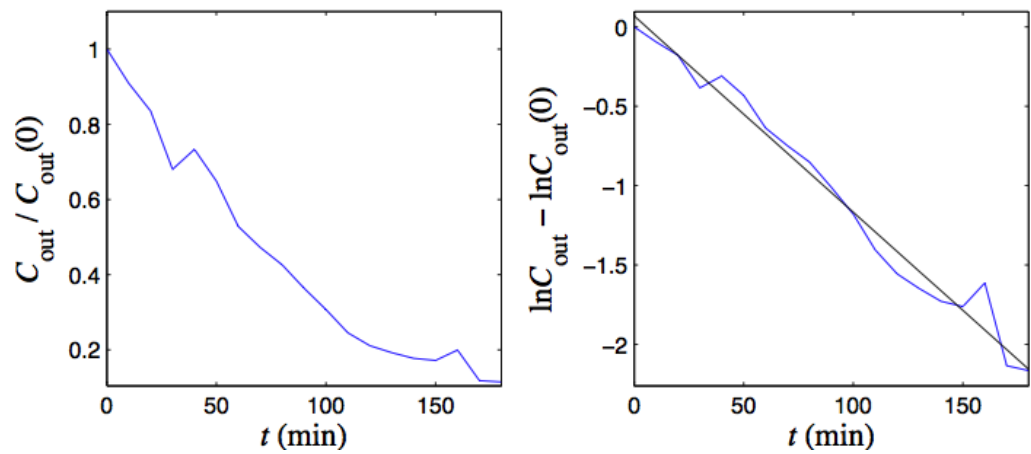


Figure 85. Coarse sand, high seepage flow ($\Delta h = 3''$), crack hole diameter $d_b = 0.21$ cm.

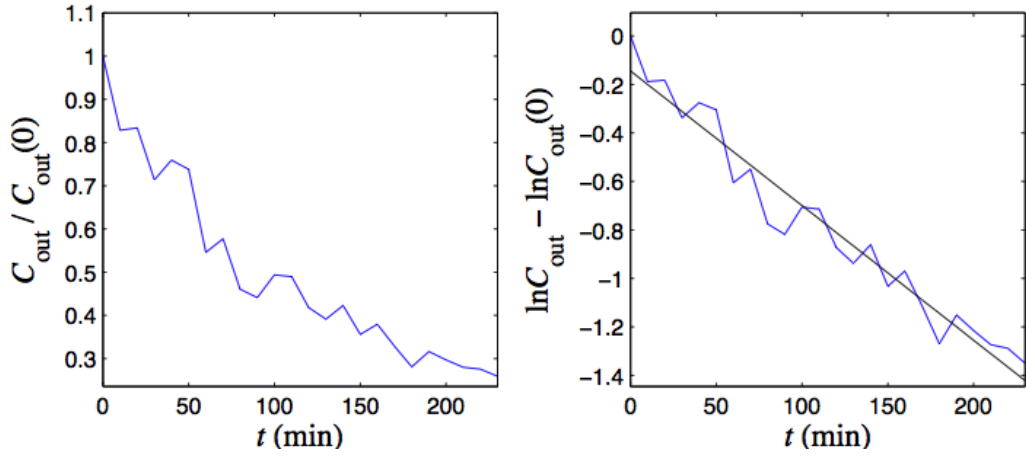


Figure 86. Coarse sand, low seepage flow ($\Delta h = 1''$), crack hole diameter $d_b = 0.40$ cm.

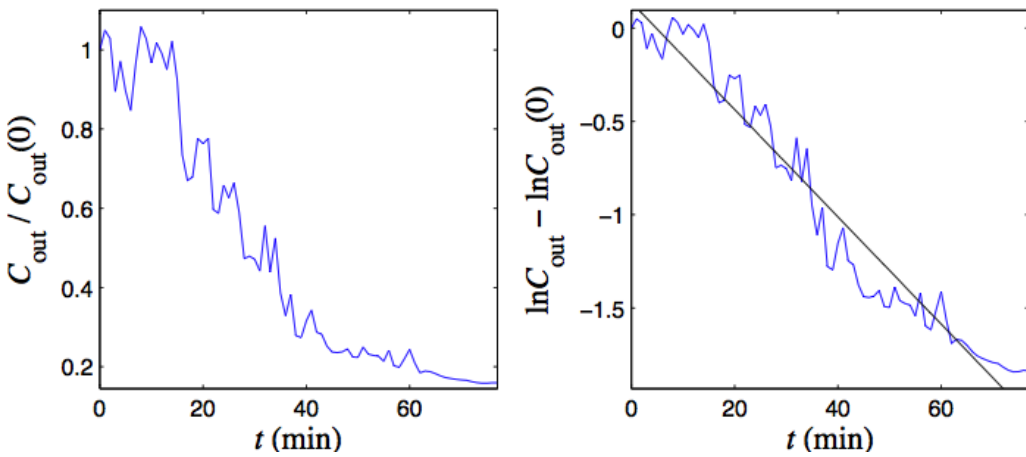


Figure 87. Coarse sand, medium seepage flow ($\Delta h = 2''$), crack hole diameter $d_b = 0.40$ cm.

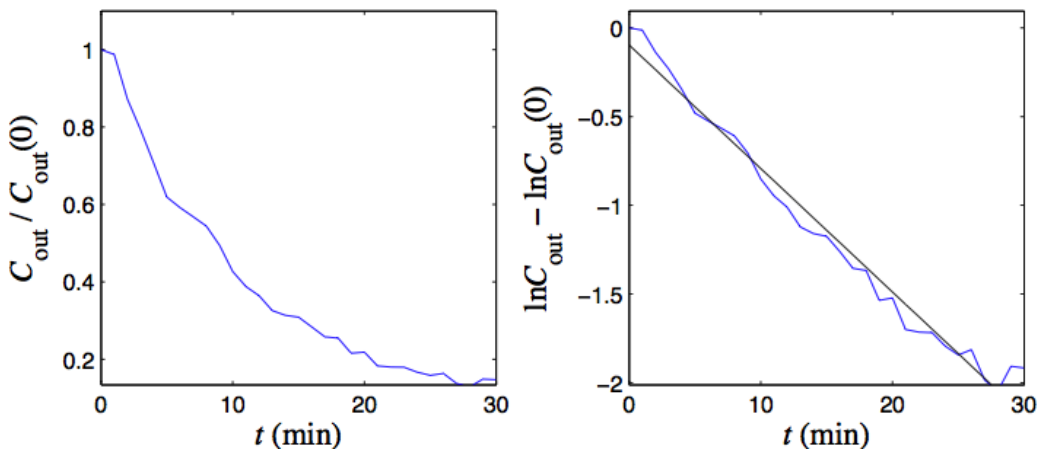


Figure 88. Coarse sand, high seepage flow ($\Delta h = 3''$), crack hole diameter $d_b = 0.40$ cm.

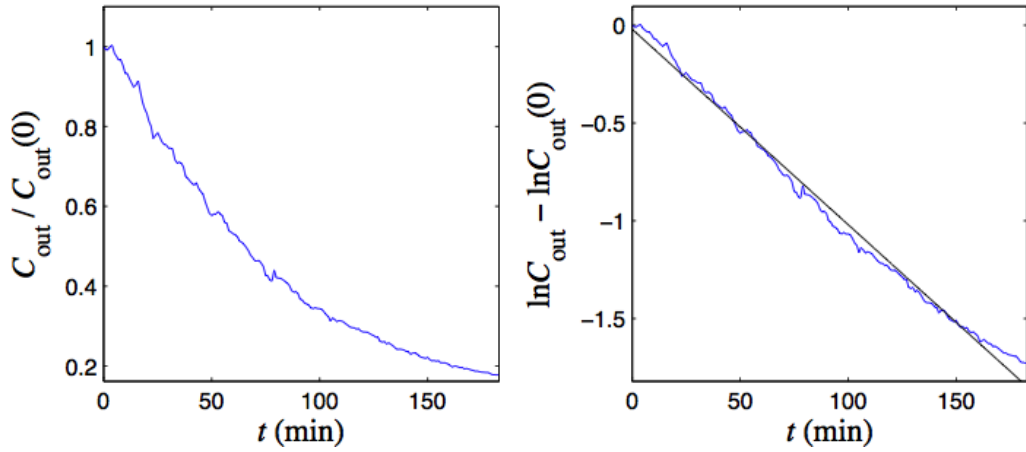


Figure 89. Coarse sand, low seepage flow ($\Delta h = 1''$), crack hole diameter $d_b = 0.56$ cm.

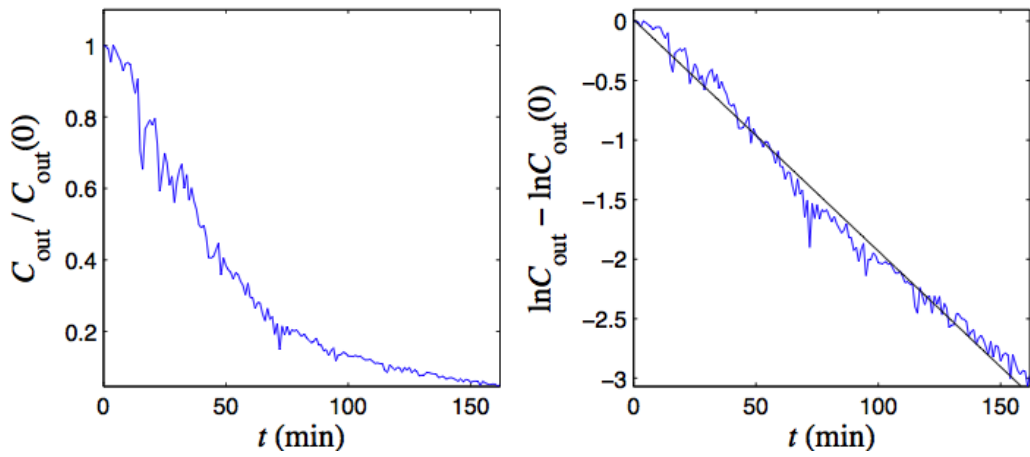


Figure 90. Coarse sand, medium seepage flow ($\Delta h = 2''$), crack hole diameter $d_b = 0.56$ cm.

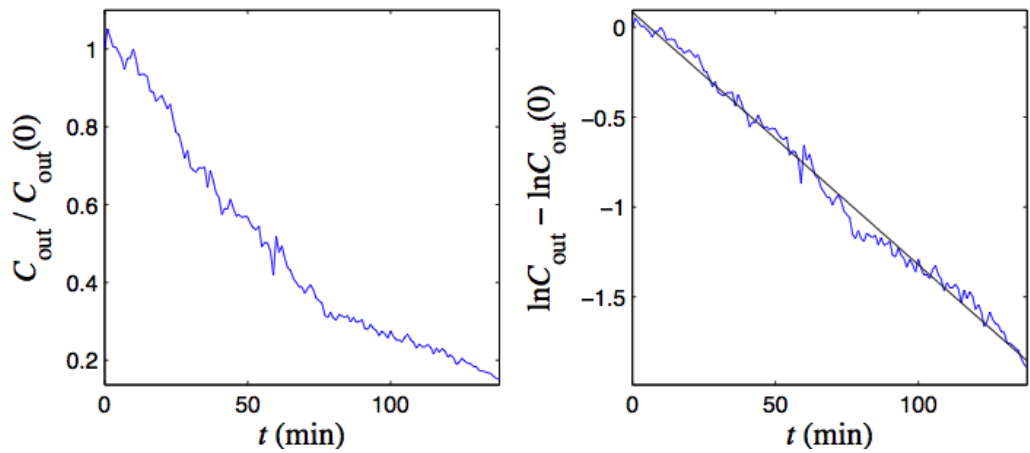


Figure 91. Coarse sand, high seepage flow ($\Delta h = 3''$), crack hole diameter $d_b = 0.56$ cm.

The estimated mass release velocity u_f is plotted against the local seepage velocity u_s in Figure 92 for all measurements shown in Figure 74 through Figure 91, above. A linear relationship exists between u_f (experimental mass release velocity) and u_s (seepage flow velocity) and the release velocity has no obvious dependency on either the crack hole diameter or on the type of sand, meaning it is not restricted by these variables. Linear regression (with intercept forced to zero) on all of the data indicates that $u_f = 1.53 u_s$ with the coefficient of determination $R^2 = 0.96$.

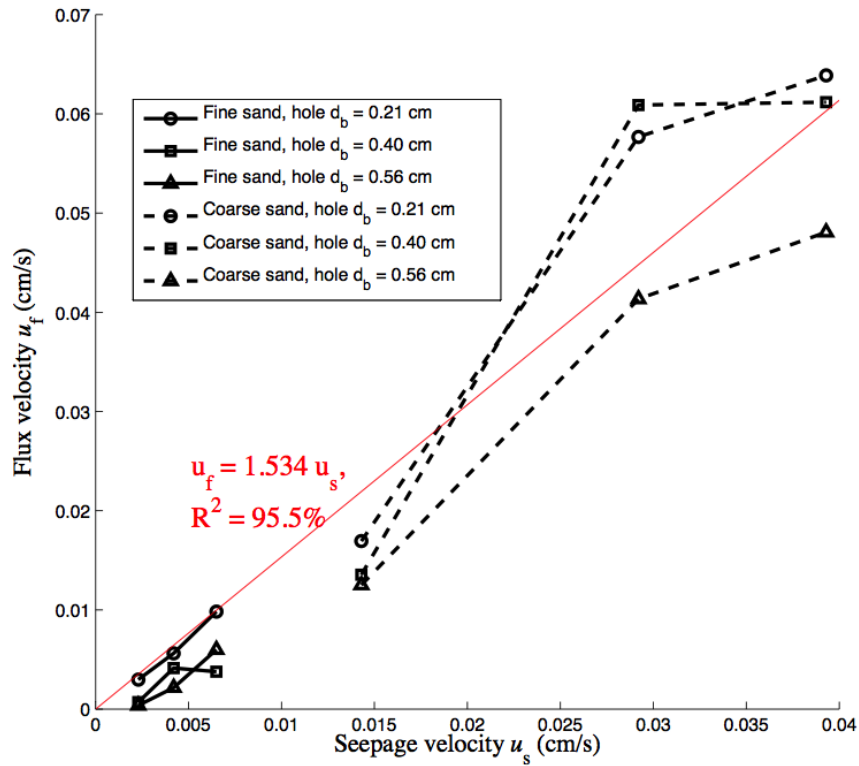


Figure 92. Relationship between the estimated mass release velocity (u_f) and the seepage flow velocity (u_s).

4.6.1 Flux with Zero Seepage Velocity

The limiting experiment for the case of zero seepage velocity was also conducted with the same container and a breach hole diameter $d_b = 0.56$ cm. A bucket (diameter = 40 cm) was filled with sand and then water to a depth of 20 cm above the sand. The breached container with Rhodamine WT (concentration $C_0 = 680$ ppm) was buried in sand at a depth of ~ 5 cm. The water above sand was continuously and gently stirred (without causing seepage flow in the water) such that once the dye diffused from the porous sand into the overlying water, it would be adequately mixed. Concentration of dye in water was measured at set time intervals (~ 50 hr) for ~ 400 hours (16 days). Figure 93 shows the time series of measured dye concentrations in water.

The remarkably linear variation of concentration with time indicates a quasi-constant release rate of dye from the container over the 2-week period. For the release rate model, $F = C_0 A u_f$, the estimated mass release velocity in this case is $u_f = 0.00005$ (cm/s), ~ 2 orders of magnitude smaller than the case with seepage flow exhibiting the lowest mass release velocity of all cases tested ($u_s = 0.023$ mm/s).

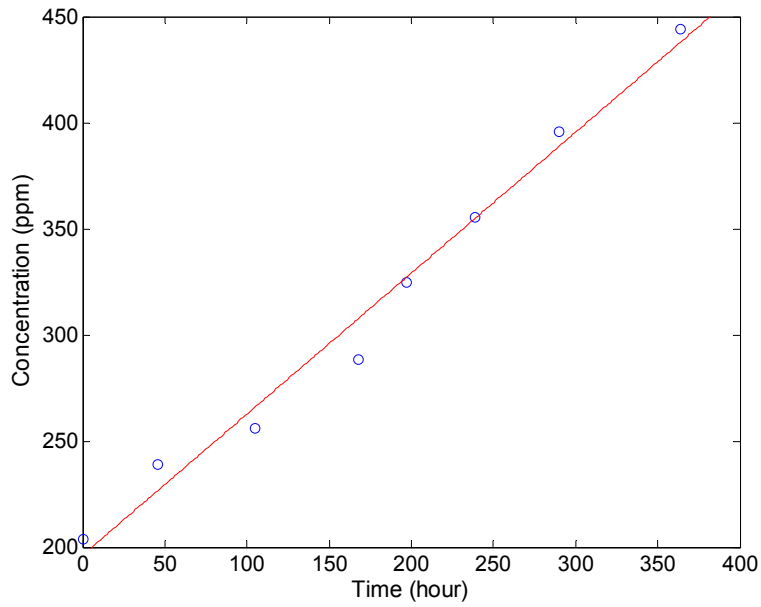


Figure 93. Change of concentration in water above the sand.

4.7 MODELING STUDY RESULTS – BURIED SHELL

Figure 94 compares the Darcy velocity calculated by the model to the measured velocity for the fine and coarse sand under the three different head gradient scenarios. Model-simulated pore-water velocities mimicked measured values for all of these scenarios.

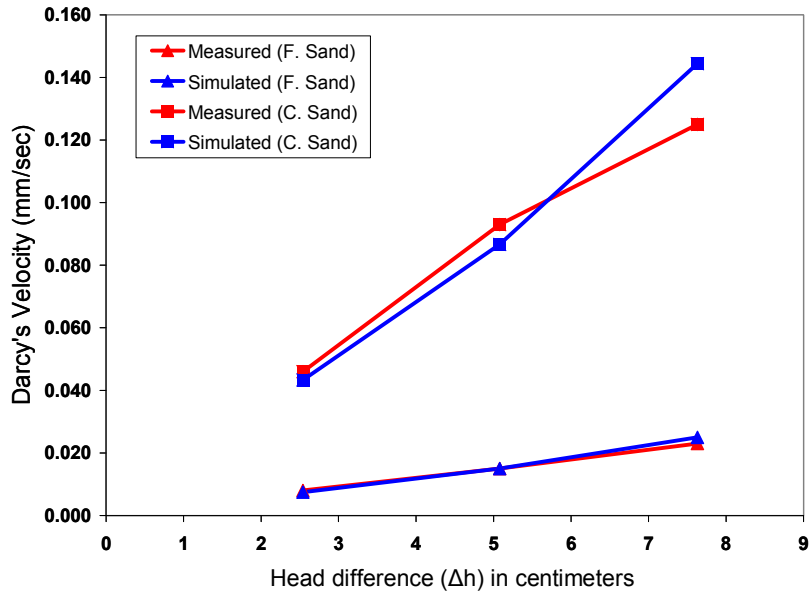


Figure 94. Comparison of simulated and measured Darcy velocities at three head pressure differences for fine and coarse sands.

4.7.1 Transport of TNT in Sediment

As discussed previously, the release rate of MC from a single breached shell (e.g., Eq. (10a) or Eq. (43)) depend on five parameters, which includes ambient current (U), hole size (b), cavity volume (R), dissolution rate constant (μ), and mixing coefficient (D). These can be grouped into two Reynolds numbers, namely Ub/D and $\mu R/D$. We have demonstrated that the MC release rate is limited by the combination of these two Reynolds numbers:

(i) Current-Controlled Release ($\mu R / D \gg Ub/D$)

When the dissolution speed (μ) is much larger than the ambient current (U) or the cavity (R) is much larger than the hole (b), MC solutions inside the cavity are near saturation and the release rate of MC is controlled by the ambient current speed U and the hole size.

(ii) Dissolution Rate-Controlled Release ($\mu R / D \ll Ub/D$)

For this case, release of MC is controlled by the dissolution rate (μ) since ambient current and/or the hole is so large that MC solution dissolved from the solid phase is dispersed out of the breached shell immediately.

For both cases, the mixing coefficient, D , plays a significant role in the release rate. We previously demonstrated that for the water column, current speed is in general larger than 0.1 cm/sec, which according to the mixing coefficient, developed empirically can be estimated as

$$\frac{D}{\beta} = 0.012Ub ,$$

where β is an empirical constant.

Generally, ambient current and its induced mixing coefficient is the primary driving force for the release rate. For release in sediment, MC is subject to mixing by low advective flow and molecular diffusivity. As the advection of the pore-water decreases, the current-induced mixing would be reduced accordingly to a level comparable to molecular diffusivity, as shown in Figure 95. As an extreme condition, when advection of pore water becomes zero (stagnant flow), fate and transport of MC in sediment is controlled by molecular diffusivity alone.

For example, in the case of TNT, molecular diffusivity becomes important when ambient current speed is reduced below $\sim 10^{-3}$ cm/s (Figure 95). This low current speed can be considered to be stagnant or below detection limits for surface water. However, for marine sediment, this low pore water flow is within the range for pore water advection. For sediment, molecular diffusivity needs to be corrected for porosity (or tortuosity) of the sediment medium:

$$D_{\text{Eff}} = D_{\text{Mol}} \varepsilon \alpha, \quad (44)$$

where ε is the porosity and α is an empirical constant (~ 1.2 to 1.8) validated by the empirical study, and D_{Mol} is the molecular diffusivity of TNT (6.54×10^{-6} cm²/s) (Lynch, Brannon, and Delfino, 2002a). Using the diffusivity and pore-water flow with speed of 0.00001, 0.0001, and 0.001 cm/s, respectively, the release rate and TNT plume are modeled under three scenarios with different relative magnitudes between the advection and diffusivity (molecular) extremes.

Advection-Diffusivity Transport of MC in Sediment and Water

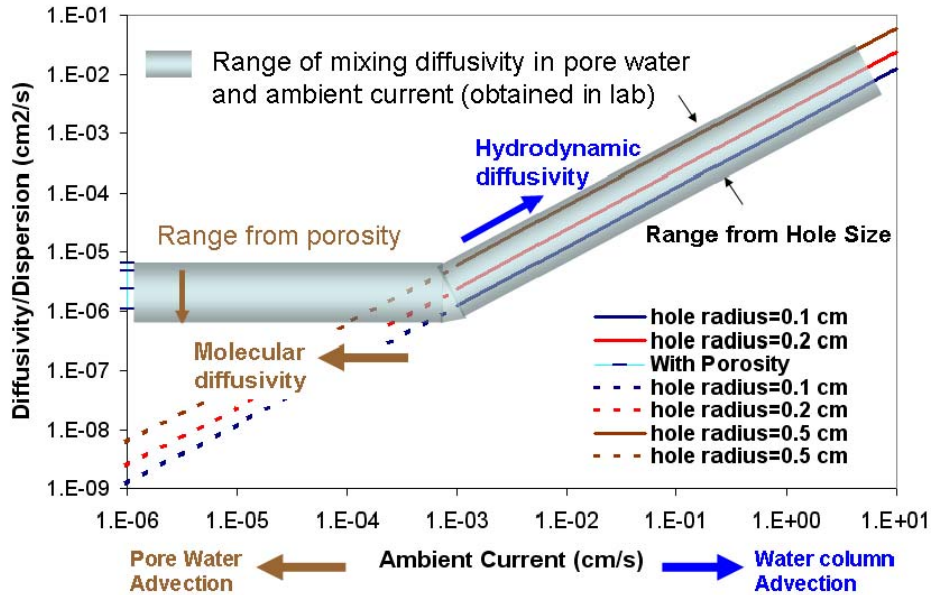


Figure 95. Range of advection and diffusivity (e.g., molecular) in water and sediment (pore water).

4.7.2 Advection-Diffusivity Transport of MC in Sediment

Transport of MC in sediment is governed by the advection-dispersion transport equation, which is the same fundamental equation as used for transport in the water column. In the latter case, advection by ambient currents dominate the mixing and transport of MC. As discussed above, for transport in sediment, both advection and diffusivity (molecular) need to be considered, in particular, for low or stagnant-water flows.

Figure 96 through Figure 98 show simulated dispersive behaviors of a substance (e.g., MC), located at (0,0) with concentration of 500 units initially ($t > 0$) at time = 23 hours, 7th day and 30th day, respectively. A horizontal diffusivity $D_x = D_y = 1.18 \times 10^{-6} \text{ cm}^2/\text{s}$ for the x-y plane and a vertical diffusivity $= 0.5 D_x(y)$ for the z-direction are used. Concentrations in the three vertical planes, $z = -5, 0$ and 5 cm , respectively, are shown. The figure shows that on the $z = 0$ plane, diffusion of concentration at the 10% of the boundary condition (500 units at (0,0)) expand to a radius of $\sim 5 \text{ cm}$ and $\sim 7 \text{ cm}$ at the end of 7th day and 30th day, respectively. At both $z = -5 \text{ cm}$ and 5 cm planes, no appreciable concentrations are reached at $t = 23$ hours. These different concentrations are within the same order of magnitude as those measured in the laboratory, discussed previously.

Figure 99 shows the advection-diffusion transport for different relative magnitudes of advection and diffusivity. The three pore-water seepage velocities are $0.001, 0.0001, \text{ and } 0.00001 \text{ cm/s}$, and the molecular diffusivities in the x-y and z planes are the same as described above (Figure 96 through Figure 98). It is hypothesized that the three seepage velocities are selected to cover a flow regime for advection dominated flow ($U = 0.001 \text{ cm/s}$) and a flow regime governed equally by advection and diffusivity ($U = 0.00001 \text{ cm/s}$). Flow advection dictates the length of the plume, whereas diffusivity dictates the expansion (width) of the plume. In Figure 99, the characteristics of advection and diffusivity effects on the transport can be visualized clearly in the model-predicted contours of the plumes.

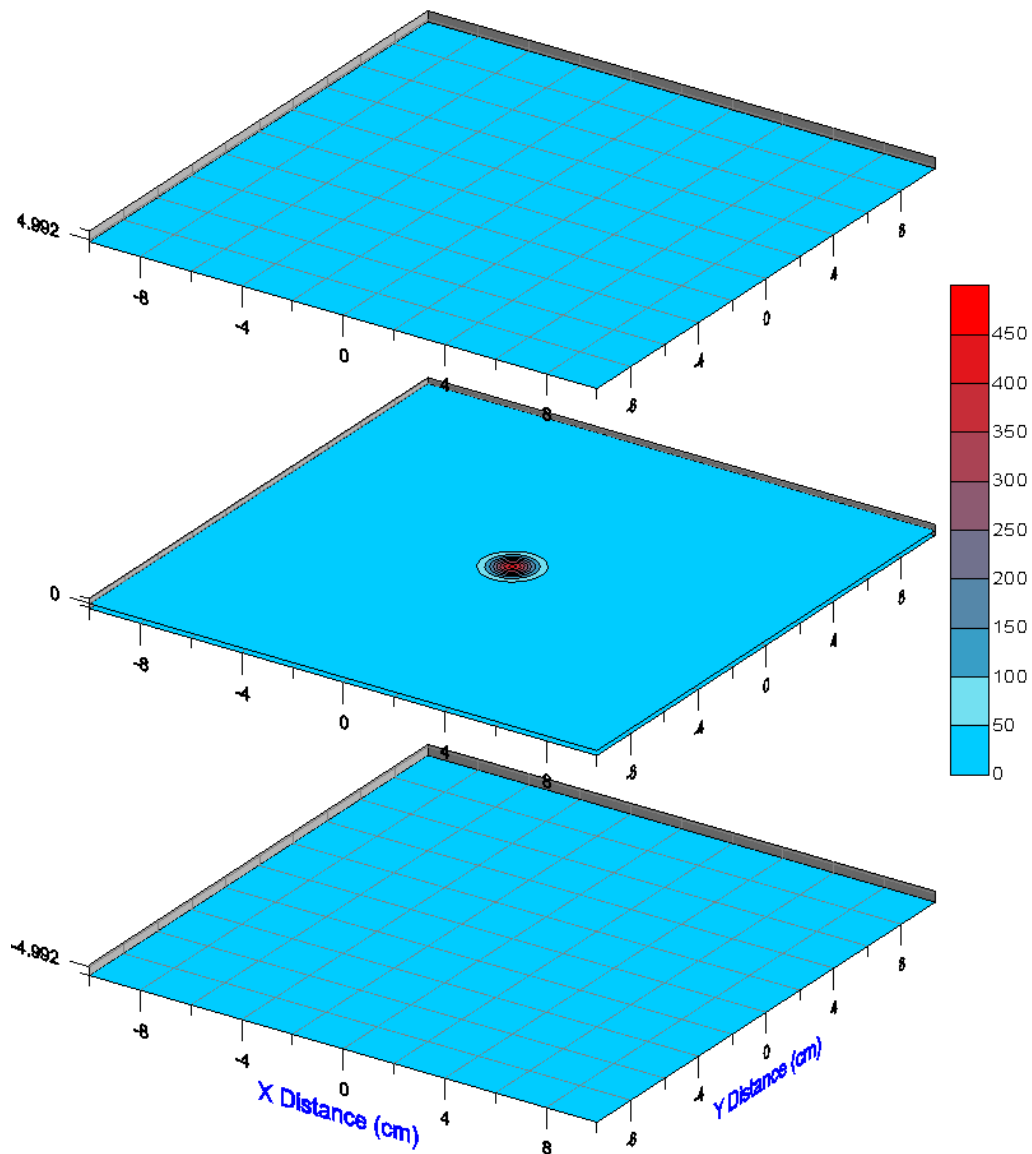


Figure 96. Dispersion of TNT in sediment by molecular diffusivity ($D_x = D_y = 1.18 \times 10^{-6} \text{ cm}^2/\text{sec}$, $D_z = 0.5 D_{x(y)}$) at time = 23 hours from initial condition (continuous source for $t > 0$, with concentration of 500 units at $(0,0)$).

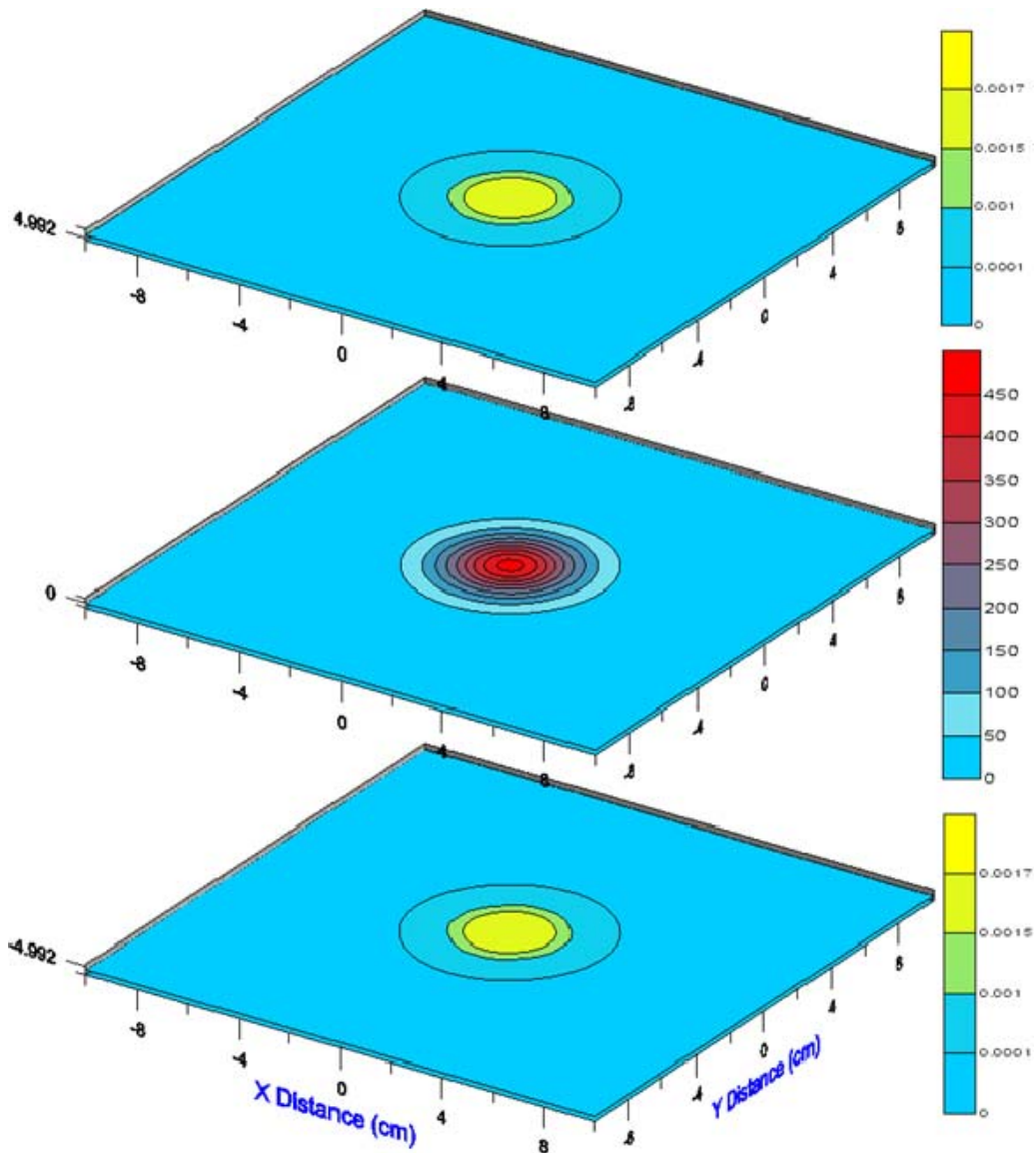


Figure 97. Dispersion of TNT in sediment by molecular diffusivity ($D_x = D_y = 1.18 \times 10^{-6} \text{ cm}^2/\text{sec}$, $D_z = 0.5 D_{x(y)}$) at time = 7th day from initial condition (continuous source for $t > 0$, with concentration of 500 units at (0,0)).

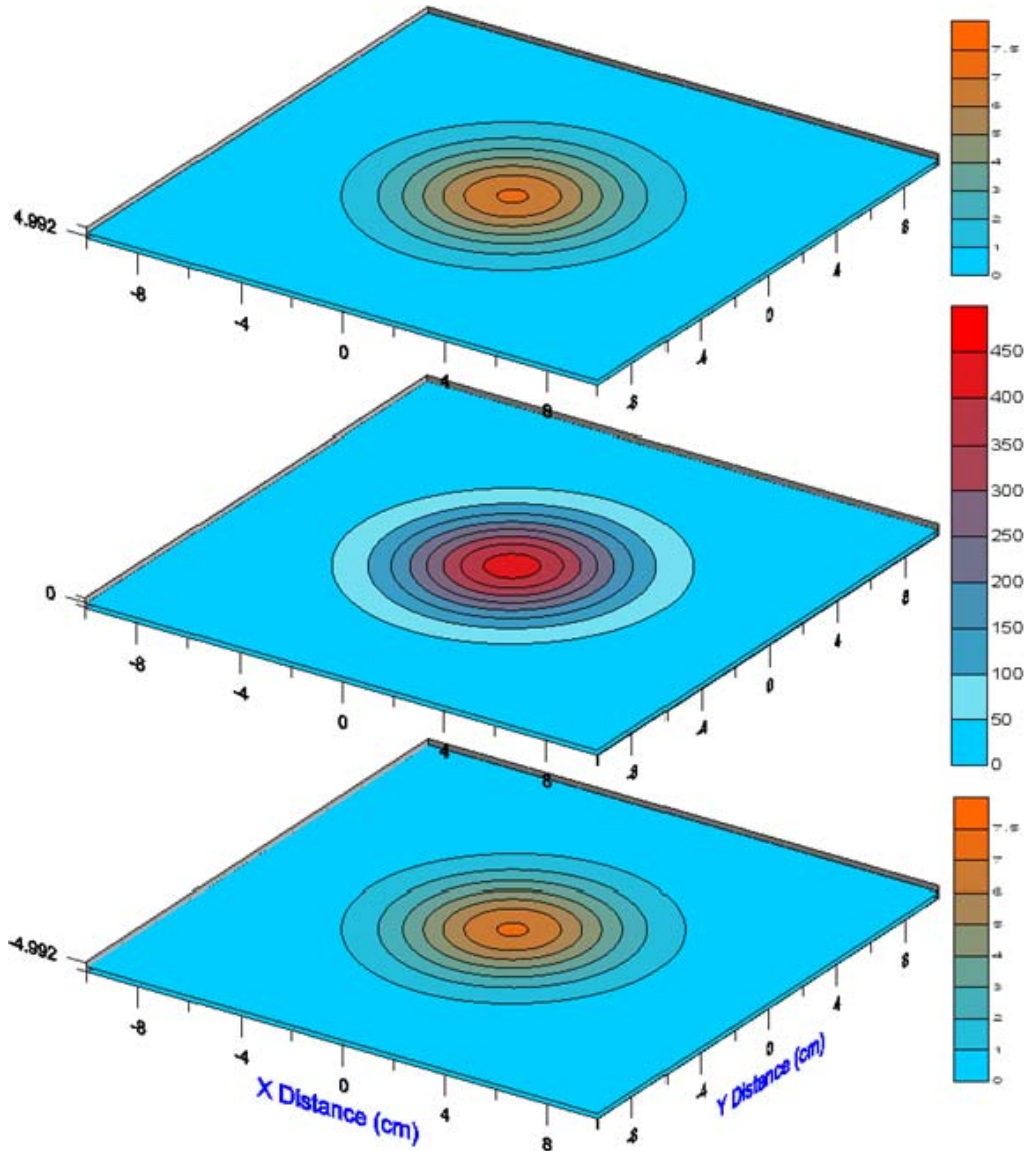


Figure 98. Dispersion of TNT in sediment by molecular diffusivity ($D_x = D_y = 1.18 \times 10^{-6} \text{ cm}^2/\text{sec}$, $D_z = 0.5 D_{x(y)}$) at time = 30th day from initial condition (continuous source for $t > 0$, with concentration of 500 units at $(0,0)$).

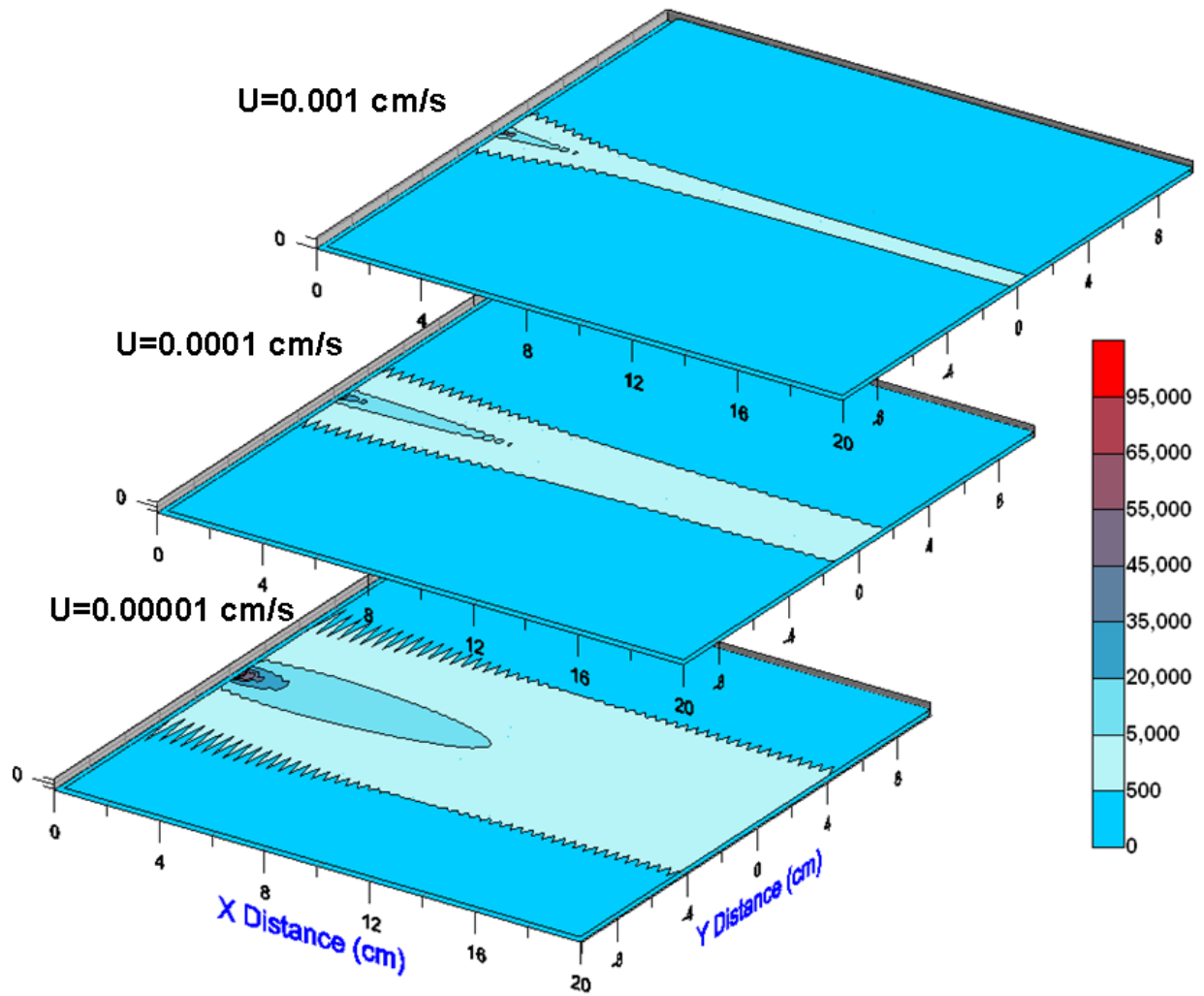


Figure 99. Transport of TNT in sediment by molecular diffusivity ($D = 1.18 \times 10^{-6}$ cm²/s) and advection ($U = 0.001, 0.0001$ and 0.00001 cm/s, for top, middle, and bottom figures, respectively) from initial condition (continuous source for $t > 0$, with concentration of 100,000 units at (0,0))

5. CONCLUSIONS AND IMPLICATIONS FOR FUTURE RESEARCH/IMPLEMENTATION

Theoretical and numerical studies were conducted for the release of munitions compounds from a single breached shell under various hydrodynamic and shell integrity conditions. Analytical solutions were derived for the release rate based on the assumptions that ambient currents are tangential over the shell surface, and that the hole is small in size compared to the cavity inside the shell. These theoretical analyses and numerical simulations have demonstrated that the flux of MC solution can be expressed explicitly as a function of five primary variables: current speed U , hole area A , saturated concentration C_S , dissolution speed (μ), and hydrodynamic dispersion coefficient D (Eq. (10a)). The analytical release rate solutions were validated by the model results using FLUENT.

5.1 RELEASE RATE

The validated results show that, in a dynamic estuarine water body, release rates can experience processes that cover wide regimes including two extreme limiting conditions. For the first condition, $ub^2 \ll \mu R^2$, the release rate is limited by the ambient current speed. MC dissolution in the shell cavity occurs at a faster rate than the ability of MC to escape through the hole as a function of the ambient current (hydrodynamic dispersion). As a result, the solution in the cavity is always near saturation. For the condition, $ub^2 \gg \mu R^2$, where the release rate is limited by dissolution speed, MC dissolution in the cavity is much slower than the transport of MC solution through the hole. For this scenario, the solution in the cavity is not near saturation and the retention time of the MC solution inside the breached shell (cavity) is small, resulting in more mass per unit time escaping from the shell.

When the thickness of the shell (h) is considered, the general release rate retains the same functional dependence on the five variables above. However, the shell thickness imposes an effect on the release rate, which can be expressed explicitly as

$$F = \kappa U (\pi b^2) C_S, \quad (45)$$

where κ is a coefficient which assimilates the effect of the geometry of the breach and shell thickness. If the breach has a circular shape, the value of κ is between 0.015 and 0.035 according to numerical simulations, in comparison with value of 0.023 when the thickness is ignored. This empirical model suggests that the MC release rate grows linearly with U , A , and C_S , while it is independent of the cavity size R . This model is only valid if the breach size is relatively small compared to the cavity inside the shell ($b \ll R$) and the shell thickness is large compared to the hole radius ($h > b$).

A series of scenarios were designed and conducted in Phase III to study the release rate of MC from breached shells in marine environment. Based on the semi-analytical release rate function developed in the Phase I study, extensive experiments and corresponding modeling studies were conducted to examine the mass release rate of a surrogate dye from a semi-spherical cavity through a circular hole. The experiments investigated the effects of breach hole sizes, shapes, and orientations on transport out of the breached shell into the external water. Of the five variables that define the release rate, the hole size and the ambient current speed appear to be the two most important parameters. As such, the internal circulation magnitudes were also measured, analyzed, and characterized. The mass release rate is considered to be proportional to the local shear velocity, the mass concentration in cavity and the area of the breach. Dimensional analysis indicates that the mass release rate can be defined by a characteristic speed u_f , which is defined as the mass release speed,

i.e., $F = u_f A C_0$, where A is the area of the crack, and C_0 is the concentration of mass within the cavity. The mass release speed would then depend on the shear velocity above the crack, u_* , the size of the crack and the hole, as well as the kinematic viscosity of water.

Experimental study in this report entailed the variables with values with the following ranges: $u_f = 0.4 \sim 2 u_*$ for $b = 0.5 \sim 25$ mm and $R = 1 \sim 5$ cm. It also shows that there is no clear evidence of a relationship between the ratio of u_f/u_* and the hole radius b , or the Reynolds Number $u_* b/\nu$. However, u_f/u_* is largely determined by the cavity size R , and, thus, the Reynolds Number $u_* R/\nu$. An extrapolation of the experimental results indicates that u_f/u_* is approximately 3 to 4 for $R = 10$ cm, which is the case for our previous FLUENT simulation. Numerical simulation had shown that u_f/u_* in that case was about 1.

A linear model between u_f/u_* and the cavity-based Reynolds number Re_R seems to be plausible according to this series of experiments. The strong dependency on the cavity size R was not explicitly considered in our simple theoretical model, that is,

$$F = UC(b)\pi b^2 = \frac{2\pi DC_s}{\frac{2D}{\alpha U b^2} + \frac{D}{\alpha R^2} + \frac{1}{b} - \frac{1}{R}} \quad (46)$$

However, as we assume infinite dissolving speed and large R/b ratio, the mass release rate can be described as

$$F = \frac{2\pi DC_s}{\frac{2D}{\alpha U b^2} + \frac{1}{b}} \quad (47)$$

Additionally, the dependency on R could be linked through the in-cavity mixing coefficient D .

TNT mineralization occurs by multiple pathways, including transformation, bio-degradation and mineralization. Mineralization rates of TNT as reported are based on laboratory studies, including those of Dr. Mike Montgomery of NRL (Montgomery *et al.*, 2008). The mineralization rates, conducted and measured in the laboratory experiments appear to be high and do not follow zero- or first-order criteria. With mineralization rates this high, simulated TNT concentrations should be very low. In this study, we only consider a reported mineralization process by mineralization. Thus, the reported 1.5% TNT mineralization rate over a 24-hour period assuming concentrations of TNT of 0 to 400 ng/L (water) or ng/Kg (sediment). Assuming a first-order mineralization (an unverified assumption and extrapolation from laboratory data), this translates into in a half-life of 0.0151/day.

5.2 MC TRANSPORT

Transport processes for TNT were simulated using both a fine-scaled hydrodynamic and transport model, TRIM2D, and a box-scaled model, WASP7. Both of these models provide meaningful results that are mutually consistent and complementary, demonstrating their utility for developing an understanding of munitions constituent transport in marine environment.

For the conservative scenario, where TNT release loads enter the inner San Diego Bay (Box #1 for WASP) water column with no mineralization or exchange of mass with the sediment, results from both models compare well, demonstrating the consistency of both models. Results for this scenario provide conservative estimates of TNT in San Diego Bay.

With the use of reported soil partitioning coefficients for TNT, which are low, only a small fraction of TNT mass is distributed into the particulate/sediment phase. WASP-simulated TNT concentrations in sediment (< 0.1 ng/L for San Diego Bay and < 1 ng/L for Elizabeth River) are much lower in this scenario than the simulated TNT concentrations in the water column (< 45 ng/L). Therefore, the particulate phase-associated TNT in both water column and sediment should be low. These model results are based on the assumption of equilibrium partitioning between particulate and aqueous phase of TNT, which is considered a reversible process. However, as discussed by Brannon, it was observed that TNT is lost from the water column at relatively fast rates and sediment is a sink for TNT in the water column. This can be attributed to continuing removal of the compound from the water by degradation, transformation, or covalent bonding to sediment components such as organic carbon (Brannon *et al.*, 2005). Mostly likely, these processes are not reversible, contrary to a partitioning process, which is considered reversible.

5.3 SETTLING AND RESUSPENSION

When the exchange of TNT mass between water column and sediment is considered, WASP7 is used to account for these mass-exchange processes, including partitioning, settling, and resuspension, in addition to the hydrodynamic transport. Partitioning of TNT onto TOC with TSS as the transport vehicle describes the particulate phase-associated behavior of TNT. Mass exchange of TNT across the water/sediment interface takes place through settling and resuspension of TSS. By settling, the particulate phase of TNT moves into the sediment bed, which is assumed to be homogenous over the top mixing-layer thickness. Sediments, and the particulate phase of TNT, are considered mobile and are transported back into the water column through the resuspension processes. However, the empirical study conducted by Pennington indicated that sorption of TNT to TOC in water could not reach a steady-state condition, implying that sorption of TNT may not follow a reversible process, which is the underlying assumption for use of partitioning coefficient. Accordingly, for this study, partitioning coefficients reported for soils were used to simulate TNT in both the water column and sediment.

Generally, literature reports describing gross settling and resuspension rates (velocities) in rivers and harbors are not adequate. However, field data, such as net erosion or deposition over extended time, can be used to deduce the order of magnitude for each individual process. In this study, we used Stokes Law to estimate settling velocity and the resuspension velocity is calculated based on the assumption that there is no net erosion or deposition throughout San Diego Bay. This baseline assumption/approach is taken for simplification purposes in the modeling study. As more field data become available, estimates with higher certainty can be made for the settling and resuspension velocities.

For the release rate of 8 kg/year from a single-shell, it is estimated that TNT concentrations in the water column are ~ 40 ng/L for both estuaries. Simulated TNT concentrations in sediment for San Diego Bay are ~ 0.1 ng/L, and ~ 1 ng/L for the Elizabeth River, a one order of magnitude difference. This is because the two systems have significantly different TSS characteristics and behaviors (Table 19).

For example, TSS concentrations in San Diego Bay and Elizabeth River are 2 mg/L and 15 mg/L, respectively, a factor of 7X. Settling velocities are 12 m/day for San Diego Bay and 50 m/day for Elizabeth River, a difference of a factor of 4X. Resuspension velocity for San Diego Bay is 2.6×10^{-7} m/day, compared to Elizabeth River at 3.0×10^{-4} m/day, a difference of three orders of magnitude. Therefore, the exchange of TSS and associated TNT between the water column and sediment, via settling, resuspension, and partitioning, is much more active in Elizabeth River than in San Diego Bay, resulting in higher predicted TNT concentrations in sediment.

Table 18. Comparison of TSS, settling velocity, and resuspension velocity for San Diego Bay and Elizabeth River.

	San Diego Bay	Elizabeth River
Settling Velocity (meters/day)	12	50
Resuspension Velocity (meters/day)	2.6×10^{-7}	3.0×10^{-4}
Total Suspended Solid (mg/L)	2	15

Transport and flushing of munition compounds in estuaries is primarily governed by hydrodynamics, including tides and freshwater inflows. We have examined the transport and flushing characteristics for TNT in two estuarine scenarios: San Diego Bay, which has only tidal flushing, and Elizabeth River, which has both tidal and riverine flushing. These examples, chosen for their respectively unique estuarine characteristics, should represent most transport and flushing behaviors encountered in DoD harbors.

5.4 SCALING AND INTERPRETATION

An energy balance analysis was undertaken based on the sketch shown in Figure 100. The overall magnitude of in-cavity circulation velocity is denoted as u_m . The characteristic velocity near the breach can be considered as the shear velocity u_* . Taking the cavity as the control volume, the energy influx into the cavity should be in balance with energy dissipation in the volume under an equilibrium state. The energy influx should scale with $u_*^3 b^2$ and the dissipation should scale with $(u_m^3/R)R^2 = u_m^3 R^2$. If this scaling is right, the mixing coefficient can be scaled as

$$D \sim u_m R \sim u_* R^{1/3} b^{2/3}; \quad (48)$$

thus D becomes relevant in Equations (47) and (47).

Experimental investigation on the scaling between u_m and u_* is underway, which may explain the observed dependency of u_f on the cavity size R .

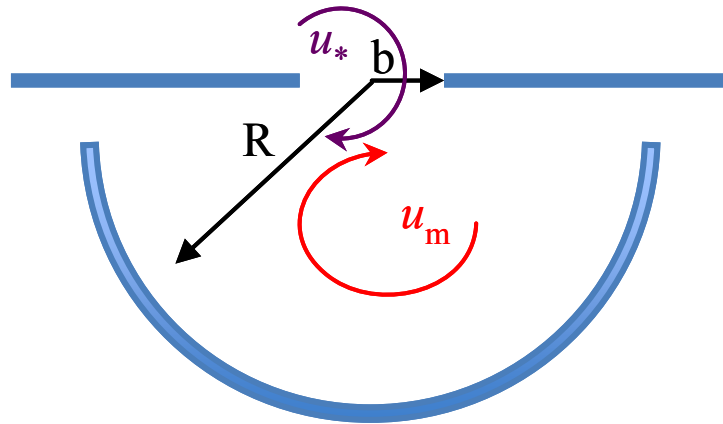


Figure 100. A sketch of an energy balance model to scale the in-cavity circulation to external shear velocity.

Overall, assuming equal opening areas, different shapes of the breach hole will generate different mass release rates, which are, however, small to moderate (Figure 66, Figure 67, and Figure 68). The size of the hole (area) has more effect on the mass release rate than the shape of the hole. The same conclusion is made for the orientation of cracks, which are simulated as two rectangles with the

aspect ratios of 1:4 and 1:10, respectively (Figure 69). These findings indicate that hydrodynamic mixing (i.e., release velocity) is governed more by the magnitude of the ambient current than by the direction of the current relative to the breach holes. In reality, formation of the breach holes, and cracks by corrosion can be a random process in terms of their shapes and orientations, which is not as important for the mass release rates as is the total area of the breach hole.

While the mass release rate for a single shell with a breach hole has been studied, there are inherent uncertainties for estimation for release from more than one shell. The semi-empirical release function, which has been validated by both the empirical and modeling studies, can be used to estimate the release rates of MC (surrogate dye in the study) from a breached shell under various cases of shell integrity and ambient hydrodynamic conditions. Uncertainty for the release rate includes two sources. The first sources of uncertainty are variabilities associated with the five variables in the release rate function. For example, a group of breached shells may have breach holes with a variety of various sizes. The ambient hydrodynamic current speed may also fluctuate with different tidal and flow conditions under which the breach shells reside. As such, probabilistic modeling simulations were conducted (Section 0). In these simulations, the size of the breach hole and the ambient current are allowed to possess probability distributions due to variabilities associated with them. The Monte Carlo method was used to quantify the effects of these two variables on the mass release rate in a probabilistic manner (Figure 71, Figure 72, and Figure 73). The same probabilistic modeling method can be used to study the uncertainties associated with lack or inadequacy of the knowledge or data associated with the variables for the mass release rate.

5.5 SIMULATING BREACHED SHELL SCENARIOS

Initially, MC release into the water column from breached shells in marine environments was studied using three complimentary approaches: analytical, empirical, and numerical study components. The study was based on the conceptual model shown in Figure 1 with MC release from a breached shell. Two initial nominal scenarios were studied and results validated, including a breached shell sitting on top of the sediment with hydrodynamic actions imposed by ambient current, and a low order detonation (MC fully exposed to ambient current). We have also addressed a third nominal case, a breached shell buried in sediment, for which a study of MC release from breached shells buried in sand has been conducted and results reported herein. In a manner similar to the water column release studies, fluorescent dye experiments were conducted in a laboratory sediment channel contained within a constructed sand flume box. Two types of sand were used as the porous medium to simulate the sediment bed of a coastal ocean. The mean grain diameter of the two sands were $d_s = 150 \mu\text{m}$ and $500 \mu\text{m}$. A small bottle of fluorescent dye solution with a breach hole in the cap (hole diameter $d_b = 0.21, 0.40, \text{ and } 0.56 \text{ cm}$) was buried in the sediment channel and the dye was transported by seepage flow under a maintained pressure gradient. Eighteen experiments were conducted to simulate shells buried in sediment, which included two sand sizes (fine and coarse sand), three pore-water flow regimes (low, medium, and high), and three hole sizes (0.2, 0.4, and 0.56 cm).

Measured pore-water flow rate (speed) compared well with the model-simulated values for all of these cases, confirming that results from the empirical and numerical models are consistent, and should thus be accurate. Release rates were determined by measuring the release dye concentrations at the outlet of the flume box over time. The measured time series of the dye concentration compared well with the analytical solution for all 18 cases and follows a first-order decay rate. The good comparison of the pore-water advection over the low-, medium-, and high-flow regimes, coupled with the dye release rate provides evidence that processes controlling MC release from breached shells buried in sand have been successfully parameterized, simulated, and validated. A first-order depletion model can be used to explain the observed time history of the exit dye concentration. This

model is then applied to validate the mass release rate model,

$$F = C_0 A u_f,$$

where C_0 is the mass concentration near the breach, A is the area of the breach, and u_f is a mass release velocity. Experimental results indicate that u_f is linearly proportional to the seepage velocity near the breach hole and 1.53 times the seepage velocity (u_s). The study of mass release rate from breach holes subject to water flow shows that $u_f = 0.4 \sim 2 u_*$, where u_* is the shear velocity of the mean flow. In both water column flow and sediment porous seepage flow, mass release velocity, u_f , is linearly proportional to the index velocity, which is the friction velocity, u_* , and the seepage flow velocity, u_s , for water column flow and sediment seepage flow, respectively. It is important to observe that the proportionality constants of 1.53 (Figure 92) for sediment seepage flow and 0.4 to 2.0 for water flow (Wang *et al.*, 2007) are comparable in magnitude.

5.6 FUTURE RESEARCH/IMPLEMENTATION

Much understanding has been obtained about the fate and transport of MC leached from breached shells in both the water column and sediment. When the shell is buried in sediment, fate and transport of MC released from the shell would be slowed, occurring on a time scale much longer than the modeled transport in the water column. This slow, long-term process needs to be considered in conjunction with the possibility of accumulated effects from multiple buried shells. A quantitative, model-based treatment of these factors will be required to understand the significance of fate and transport for these scenarios, which may be reflective of a more realistic or real-world scenario. Future experimental and monitoring studies are needed to further understand the behavior of TNT in marine waters, in particular the ability to evaluate dynamic exchange and transformations of TNT and degradation products specific to known decay pathways appear to be limited. This type of effort should include a systematic sensitivity/uncertainty evaluation and selective experimental and monitoring validation of the developed critical model components.

Finally, MC transport modeling through sediment surrounding a buried, breached shell may include the presence of naturally occurring organic matter (NOM). Such organic matter may impact both MC transport and related degradation. While the study of NOM as a factor in attenuating MC fate and transfer was not included in this effort, this issue can be considered by the shell model in two different ways: (a) as dissolved NOM associated chemically with MCs (as MC-NOM), and (b) as MC partitioning onto particulates of NOM. The shell model can treat MC-NOM in a similar fashion as that for MC in case (a), and it is readily implementable to simulate dissolved MC-NOM in a way similar to that for MC in case (b). However, MC-NOM transport and MC transport are similar enough that explicit treatment may not be needed. The MC partitioning (b) can also be treated as part of sedimentation and resuspension, a capability which is included in the model.

6. REFERENCES

- Adams, J., *et al.* 1999a. "Ocean Currents." *Microsoft Encarta*. 2 vols. CD-ROM. Microsoft, Redmond, WA, 191.
- Adams, J., *et al.* 1999b. "Ocean Currents." Speed of Ocean Current, <http://hypertextbook.com/facts/2002/EugeneStatnikov.shtml>.
- Ambrose, R.B., T.A. Wool, J.L. Martin, J.P. Connolly, and R.W. Schanz. 1992. WASP4, a Hydrodynamic and Water Quality Model - Model Theory, User's Manual, and Programmer's Guide, U.S. Environmental Protection Agency, Athens, GA.
- Bear, J. 1979. *Hydraulics of Groundwater*. McGraw-Hill Publishing Company. New York, NY.
- Brannon, J.M., and J.C. Pennington. 2002. Environmental Data and Transport Process Descriptors for Explosives. Technical Report TR-02-10. U.S. Army Engineer Research and Development Center, Vicksburg, MS
- Brannon, J.M., C.B. Price, S.L. Yost, C. Hayes, and B. Porter. 2005. Comparison of environmental fate and transport process descriptors of explosives in saline and freshwater systems. *Marine Pollution Bulletin* 50:247–252.
- Chadwick D.B., J. Leather, K. Richter, S. Apitz, D. Lapota, D. Duckworth, C. Katz, V. Kirtay, B. Davidson, A. Patterson, P. Wang, S. Curtis. 1999. "Sediment Quality Characterization Naval Station San Diego: Final Summary Report." Technical Report 1777. SSC San Diego, San Diego, CA.
- Cheng, R.T., V. Casulli, and J.W. Gartner, 1993. "Tidal, Residual, Intertidal Mudflat (TRIM) Model and Its Applications to San Francisco Bay, California," *Estuarine, Coastal and Shelf Sciences* 36:235–280.
- Coble, C.R., E.G. Murray, and D.R. Rice. 1987. *Earth Science*. 3rd ed. Prentice Hall, Englewood Cliffs, NJ.
- Freeze, R.A., and J.A. Cherry. 1979. *Groundwater*. Prentice Hall, Englewood Cliffs, NJ.
- Fried, E. and I.E. Idelchik. 1989. *Flow Resistance: A Design Guide for Engineers*. Hemisphere Publishing Corporation, New York, NY.
- Gaskell, T.F. 1973. *The Gulf Stream*. John Day Company, New York, NY.
- Gerald, J.A., and M.S. Dortch. Predicting range UXO source quantity and its impact on future training (unpublished manuscript)
- Gross, M.G. 1982. *Oceanography: A View of the Earth*. 3rd ed. Prentice Hall, New York, NY.
- Gross, M.G. 1990. *Oceanography*. 6th ed. Merrill Publishing Company, Columbus, OH.
- Huang, G. -L., H. Xiao, J. Chi, J., W. -Y. Shiu, D. Mackay. 2000. "Effects of pH on the aqueous solubility of selected chlorinated phenols," *J. Chem. Eng. Data* 45, 411–414.
- Huettel, M. and G. Gust. 1992. "Impact of Bioroughness on Interfacial Solute Exchange in Permeable Sediments," *Marine Ecology-Progress Series* 89:253–267.

- Huettel, M., S. Forster, S. Kloser, and H. Fossing. 1996. "Vertical Migration in the Sediment-Dwelling Sulfur Bacteria *Thioploca* spp in Overcoming Diffusion Limitations," *Applied and Environmental Microbiology* 62:1863–1872.
- Lynch, J.C., J.M. Brannon, and J.J. Delfino. 2002a. "Dissolution Rates of Three High Explosive Compounds: TNT, RDX, and HMX," *Chemosphere* 47:725–734.
- Lynch, J.C., J.M. Brannon, and J.J. Delfino. 2002b. "Effects of Component Interactions on the Aqueous Solubilities and Dissolution Rates of the Explosive Formulations Octol, Composition B, and LX-14," *Journal of Chemical and Engineering Data* 47(3):542–549.
- Lynch, J.C., J.M. Brannon, K. Hatfield, and J.J. Delfino. 2003. "An Exploratory Approach to Modeling Explosive Compound Persistence and Flux using Dissolution Kinetics," *Journal of Contaminant Hydrology* 66:147–159.
- Lynch, J.C., K.F. Myers, J.M. Brannon, and J.J. Delfino. 2001. "Effects of pH and Temperature on the Aqueous Solubility and Dissolution Rate of 2,4,6-trinitrotoluene (TNT), Hexahydro-1,3,5-trinitro-1,3,5-triazine (RDX), and Octahydro-1,3,5,7-tetranitro-1,3,5,7-tetrazocine (HMX)," *Journal of Chemical and Engineering Data* 46(6):1549–1555.
- McLellan, W.L., W.R. Hartley, and M.E. Brower. 1988. Health Advisory for Octahydro-1,3,5,6-tetranitro-1,3,5,6-tetrazocine (HMX). Criteria and Standards Division, Office of Drinking Water, U.S. Environmental Protection Agency, Washington, DC.
- Montgomery, M.T., S.W. Walker, T.J. Boyd, L.J. Hamdan, and C.L. Osburn. 2008. Biotic and Abiotic Attenuation of Nitrogenous Energetic Compounds (NEC) in Coastal Waters and Sediments – Final Report. SERDP Project ER-1431, NRL/MR/6110--08-9139.
- Pennington, J. C. and Brannon, J. M. 2002. "Environmental Fate of Explosives," *Thermochimica Acta* 384:163–172.
- Polly, D. 2012. Underwater UXO Corrosion Model - Users Guide (in Prep.)
- Precht, E., and M. Huettel. 2003. "Advective Pore-water Exchange Driven by Surface Gravity Waves and its Ecological Implications," *Limnology and Oceanography* 48:1674–1684.
- Precht, E., and M. Huettel. 2004. "Rapid Wave-driven Advective Pore Water Exchange in a Permeable Coastal Sediment," *Journal of Sea Research* 51:93–107.
- Reimers, C.E., H.A. Stecher, G.L. Taghon, C.M. Fuller, M. Huettel, A. Rusch, N. Ryckelynck, and C. Wild. 2004. "In situ Measurements of Advective Solute Transport in Permeable Shelf Sands," *Continental Shelf Research* 24:183–201.
- Ro, K.S., A. Venugopal, D.D. Adrian, D. Constant, K. Qaisi, K.T. Valsaraj, L.J. Thibodeaux, and D. Roy. 1996. "Solubility of 2,4,6-trinitrotoluene (TNT) in Water," *Journal of Chemical Engineering Data* 41:758–761
- Spanggord, R.J., R.W. Mabey, T. Mill, T.W. Chou, J.H. Smith, S. Lee, and D. Roberts, D. 1983. "Environmental Fate Studies on Certain Munitions Wastewater Constituents: Phase IV – Lagoon Model Studies," AD-A133987, SRI International, Menlo Park, CA, for U.S. Army Medical Research and Development Command, Ft. Detrick, MD.
- Thomann, R. V., and J. A. Mueller, 1987. Principles of Surface Water Quality Modeling and Control. Harper and Row, Inc., New York, NY.

- Wang P.F., R.T. Cheng, K. Richter; E.S. Gross; D. Sutton; and J.W. Gartner. 1998a. "Modeling Tidal Hydrodynamics of San Diego Bay, California," *Journal of the American Water Research Association* 34(5):1123–1140.
- Wang, P.F., and B. Chadwick. 1998b. Dilution and Transport of Convention Center Effluent of Copper, Zinc and Silver in San Diego Bay. SPAWAR Systems Center San Diego draft report for the Port of San Diego.
- Wang, P.F., D. Sutton, K. Richter, and B. Chadwick. 2000. "Modeling Migration of Sediment and Sorbed Contaminants Resuspended by Ship Docking in San Diego Bay," *Proceedings of the 4th International Conference on Hydrosience & Engineering*. 26–29 September. Seoul, Korea.
- Wang, P.F., D.B. Chadwick, C. Johnson, and J. Grovhoug, 2006. "Modeling Copper and Biocide Concentrations from Hull Paint Leachate in San Diego Bay." Technical Report 1935, SSC San Diego, CA.
- Wang, P.F., J. Martin, T. Wool, and G. Morrison. 1999. "Water Quality and Eutrophication in Tampa Bay, Florida," *Estuarine and Shelf Science* 49:1–20.
- Wang, P.F., Q. Liao, R. George, and B. Wild. 2011. "Release Rate and Transport of Munitions Constituents from Breached Shells in Marine Environment." In *Environmental Chemistry of Explosives and Propellant Compounds in Soils and Marine Systems: Distributed Source Characterization and Remedial Technologies*. Chapter 16, pp. 317-340, ACS Symposium Series 1069, American Chemical Society, Washington DC.
- Wang, P.F., R. George, B. Wild, and Q. Liao. 2007. Defining Munition Constituent (MC) Source Terms in Aquatic Environments on DoD Ranges (Phase I) (ER-1453). Draft Technical Interim Progress Report submitted to SERDP.
- Wang, P.F., T. Mill, J. Martin, and T. Wool. 1997. "Fate and Transport of Metam Spill in the Sacramento River," *Journal of Environmental Engineering* 123: 704-712.
- Wang, P.F., W.H. Choi, J. Leather, and V. Kirtay, 2007. Modeling Long-Term PAH Attenuation in Estuarine Sediment, Case Study: Elizabeth River, VA, Draft Technical Report, SSC Pacific.
- Wool, T.A., R.B. Ambrose, J.L., Martin, and E.A. Comer. 2001. "Water Quality Analysis Simulation Program (WASP) version 6.0 DRAFT: User's Manual, U.S. Environmental Protection Agency-Region 4 Atlanta. GA.

REPORT DOCUMENTATION PAGE

*Form Approved
OMB No. 0704-01-0188*

The public reporting burden for this collection of information is estimated to average 1 hour per response, including the time for reviewing instructions, searching existing data sources, gathering and maintaining the data needed, and completing and reviewing the collection of information. Send comments regarding this burden estimate or any other aspect of this collection of information, including suggestions for reducing the burden to Department of Defense, Washington Headquarters Services Directorate for Information Operations and Reports (0704-0188), 1215 Jefferson Davis Highway, Suite 1204, Arlington VA 22202-4302. Respondents should be aware that notwithstanding any other provision of law, no person shall be subject to any penalty for failing to comply with a collection of information if it does not display a currently valid OMB control number.

PLEASE DO NOT RETURN YOUR FORM TO THE ABOVE ADDRESS.

1. REPORT DATE (DD-MM-YYYY) January 2013		2. REPORT TYPE Final		3. DATES COVERED (From - To)	
4. TITLE AND SUBTITLE Defining Munition Constituent (MC) Source Terms in Aquatic Environments on DoD Ranges (ER-1453) Final Report				5a. CONTRACT NUMBER	
				5b. GRANT NUMBER	
				5c. PROGRAM ELEMENT NUMBER	
6. AUTHORS P. F. Wang Q. Liao R. D. George; W. Wild				5d. PROJECT NUMBER	
				5e. TASK NUMBER	
				5f. WORK UNIT NUMBER	
7. PERFORMING ORGANIZATION NAME(S) AND ADDRESS(ES) SSC Pacific 5622 Hull Street San Diego, CA 92152-5001				8. PERFORMING ORGANIZATION REPORT NUMBER Department of Civil Engineering and Mechanics University of Wisconsin-Milwaukee Milwaukee, WI 53201 TR 1999	
9. SPONSORING/MONITORING AGENCY NAME(S) AND ADDRESS(ES) Environmental Restoration Program Manager SERDP/ESTCP 901 N Stuart Street, Suite 303 Arlington VA 22203				10. SPONSOR/MONITOR'S ACRONYM(S)	
				11. SPONSOR/MONITOR'S REPORT NUMBER(S)	
12. DISTRIBUTION/AVAILABILITY STATEMENT Approved for public release.					
13. SUPPLEMENTARY NOTES This is work of the United States Government and therefore is not copyrighted. This work may be copied and disseminated without restriction.					
14. ABSTRACT The objectives of this study were to develop a basic understanding of the release rate and subsequent fate and transport of munition constituent (MC) in water and in sediment. The ability to characterize, assess, and predict potential MC source loading and distribution has significant implications for Department of Defense (DoD) and Department of Navy (DoN) range sustainability initiatives. DoD will gain critical information for making scientifically defensible risk management decisions about underwater ordnance leave-in-place (LIP) mitigation and blow-in-place (BIP) vs. removal options. In addition to explosive blast (safety) considerations, future regulatory emphasis will likely require an assessment of potential underwater ordnance contamination and mitigation efforts that could include water and sediment quality issues. A basic understanding of processes and governing factors for the release rate and fate/transport of MC in marine environment was developed. Predictive modeling capabilities were also developed for these processes, which will help DoD scientifically address the MC issues mentioned above. With the data developed from this study, DoD will be better equipped to make technically defensible managerial decisions for sites with underwater ordnance.					
15. SUBJECT TERMS					
release rate		underwater ordnance contamination		RDX	
munition constituents		sediment seepage		HMX	
risk management		hydrodynamics TNT			
16. SECURITY CLASSIFICATION OF:			17. LIMITATION OF ABSTRACT	18. NUMBER OF PAGES	19a. NAME OF RESPONSIBLE PERSON
a. REPORT	b. ABSTRACT	c. THIS PAGE			P. F. Wang
U	U	U	U	128	19b. TELEPHONE NUMBER (Include area code) (619) 553-9192

INITIAL DISTRIBUTION

84300	Library	(2)
85300	Archive/Stock	(1)
85300	S. Baxley	(1)
71750	P. F. Wang	(2)
71750	R. D. George	(1)
71760	W. J. Wild	(1)

Qian Liao
Associate Professor
Department of Civil Engineering and
Mechanics
University of Wisconsin-Milwaukee
P.O. Box 784
Milwaukee, WI 53201 (1)

Defense Technical Information Center
Fort Belvoir, VA 22060-6218 (1)

SSC San Diego Liaison Office
C/O PEO-SCS
Arlington, VA 22202-4804 (1)

Center for Naval Analyses
Alexandria, VA 22311-1850 (1)

Andrea Leeson (1)
Environmental Restoration
Program Manager
SERDP/ESTCP
901 N Stuart Street, Suite 303
Arlington, CA 22203

Approved for public release.



SSC Pacific
San Diego, CA 92152-5001